

OPTICAL COHERENCE TOMOGRAPHY FOR RETINAL IMAGING

The work presented in this thesis was performed at the Wellman Center for Photomedicine and Harvard Medical School, Massachusetts General Hospital, Boston, Massachusetts, United States of America.

The author gratefully acknowledges grants from the National Eye Institute (R01 EY014975 and 1R24 EY 12877), Whitaker foundation (26083), Department of Defense (F4 9620-021-1-0014), CIMIT and a generous gift from Mr. and Mrs. Chen to the Optical Diagnostics Group of the Wellman Center for Photomedicine.

ISBN 90-365-2183-1

© Barry Cense 2005
All rights reserved

OPTICAL COHERENCE TOMOGRAPHY FOR RETINAL IMAGING

DISSERTATION

to obtain
the doctor's degree at the University of Twente,
on the authority of the rector magnificus,
prof.dr. W.H.M. Zijm,
on account of the decision of the graduation committee,
to be publicly defended
on Wednesday, April 20th at 13.15

by

Barry Cense

born on September 16th 1973

in Eindhoven, The Netherlands

Dit proefschrift was goedgekeurd door

De promotor: Prof. Dr. T.G. van Leeuwen

De copromotor: Prof. Dr. J.F. de Boer

Table of Contents

1.	General introduction.....	1
1.1	Introduction	2
1.2	The mechanism of glaucoma	2
1.3	Prevalence and detection of glaucoma.....	4
1.4	Aim of this thesis.....	7
2.	Slit lamp-based ophthalmic imaging with optical coherence tomography.....	11
2.1	Introduction	12
2.2	Principle of time-domain OCT.....	12
2.3	Slit lamp interface	16
2.4	Adaptive ranging for motion compensation.....	22
2.5	Summary.....	22
3.	Polarization-Sensitive Optical Coherence Tomography.....	25
3.1	Introduction	26
3.2	Polarization-sensitive OCT theory.....	27
3.3	Measurement method	29
3.4	Results	33
3.5	Discussion.....	47
3.6	Conclusion.....	48
4.	Spectral-domain optical coherence tomography.....	51
4.1	Introduction	52
4.2	Principle and sensitivity gain of SD-OCT.....	52
4.3	High-speed spectral-domain optical coherence tomography	59
4.4	Ultrahigh-resolution SD-OCT.....	69
4.5	Conclusion.....	82
5.	Polarization-sensitive spectral-domain optical coherence tomography.....	85
5.1	Introduction	86
5.2	Measurement Method.....	86
5.3	Results and discussion.....	92
5.4	Conclusion.....	102
6.	Discussion, conclusion and outlook.....	105
6.1	Discussion.....	105
6.2	Conclusion.....	106
6.3	Outlook.....	107
7.	Summary	111
8.	Samenvatting voor leken.....	113
	De opbouw van het oog.....	113
8.2	Glaucoom	114
8.3	Nieuwe detectiemethoden	116
9.	Apendix.....	119
	Acknowledgements.....	124

1. General introduction

*Abstract**

Glaucoma is the world's second leading cause of blindness. The disease causes irreversible damage to the retinal ganglion cells, resulting in thinning of the retinal nerve fiber layer (RNFL). When glaucoma is detected at an early stage, further loss of vision can be prevented by treatment. Current measurement techniques are not sensitive enough to detect glaucoma at an early stage, which is essential for successful glaucoma treatment and management. The visual field test, the gold standard for glaucoma detection, can only detect glaucoma when up to 40% of the RNFL is irreversibly lost. In this thesis, two new imaging modalities are proposed for the early detection of glaucoma. Both modalities are based on optical coherence tomography, a technology that uses low-coherence light to create two-dimensional images of the retina. Depth scans are made as reflections are detected as a function of path length difference by rapidly changing the reference arm length of an interferometer. The sensitive coherence window that is created rejects light returning from other depths.

* This chapter was partly published in the following peer-reviewed article:
B. Cense, T.C. Chen, B.H. Park, M.C. Pierce and J.F. de Boer, "Thickness and birefringence of healthy retinal nerve fiber layer tissue measured with polarization-sensitive optical coherence tomography," *Investigative Ophthalmology & Visual Science*, 45, 2606-2612 (2004).

1.1 Introduction

Glaucoma is the world's second leading cause of blindness. When glaucoma is detected at an early stage, further loss of vision can be prevented by treatment. The visual field test is currently the current standard method of detecting loss of peripheral vision in glaucoma. However, measurements show that up to 40% of nerves are irreversibly damaged before loss of peripheral vision can be clinically detected.¹

The sensitivity and specificity of currently applied measurement techniques are not high enough to detect glaucoma successfully,² which is essential for effective glaucoma treatment and management. In this thesis, two new technologies – polarization-sensitive optical coherence tomography and spectral-domain optical coherence tomography - will be introduced that may be used for the early detection of glaucoma.

First, potential mechanisms of glaucoma will be discussed, followed by its prevalence and methods used for glaucoma detection. This chapter finishes with the aim and structure of this thesis.

1.2 The mechanism of glaucoma

Light enters the eye through the cornea, pupil and lens, and is focused on the photoreceptors in the retina (see Figure 1). The light signal is converted to electrical signals which are conducted through the axons of the ganglion cells in the retinal nerve fiber layer (RNFL). These axons concentrate in the optic nerve where they are accompanied by numerous large blood vessels that spread out to supply blood to cells in the retina.³

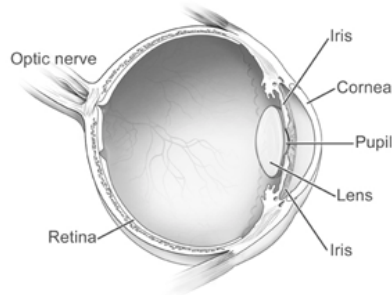


Figure 1: Schematic cross-section of a healthy human eye (courtesy of the National Eye Institute, National Institute of Health).

Transparent optical elements in the anterior segment of the eye such as the cornea and lens could not function properly if a dense network of nourishing but light absorbing blood vessels crossed it. Instead, the eye's ciliary body, located near the lens, creates a translucent fluid that nourishes these transparent elements. In a healthy eye, the influx of this fluid (the aqueous humor) is in balance with the outflow through the trabecular meshwork and Schlemm's canal. The latter is located at the periphery of the iris, beneath the sclera (see Figure 2). The sclera is the white opaque outer tissue of the eye.

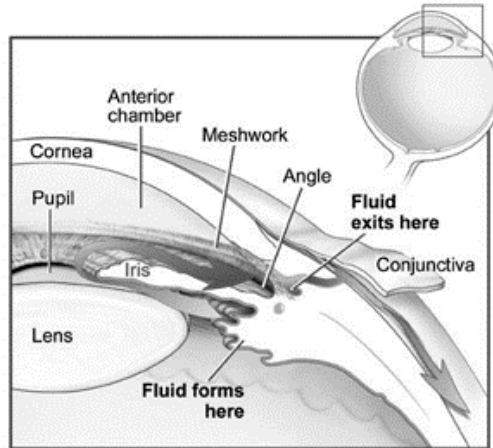


Figure 2: The eye's ciliary body ("Fluid forms here"), located near the lens, creates a translucent fluid that provides nutrients to transparent elements such as the lens and cornea. In a healthy eye, the influx of these fluids (the aqueous humor) is in balance with the outflow through the trabecular meshwork ("Meshwork") and Schlemm's canal ("Fluid exits here"). The latter is located at the periphery of the iris, beneath the sclera (image is courtesy of the National Eye Institute and National Institute of Health). A color image can be found on page 119.

Glaucoma is a name for a collection of diseases that finally result in fatal damage of the ganglion cells, probably by apoptosis (also known as cell death).⁴ The disease is related to a poor drainage of the aqueous humor. For various reasons, the trabecular meshwork or Schlemm's canal may become blocked, resulting in an increased intra-ocular pressure. The relationship between elevated intra-ocular pressure and glaucoma is poorly understood. The elevated intra-ocular pressure may reduce the blood flow to the optic nerve,³ or may deform the lamina cribrosa (located around the optic nerve outside the eye ball). Due to this deformation pressure may be exerted on the axons of the ganglion cells in the optic nerve, resulting in interruption of axoplasmic flow, which eventually kills the axon.⁵ Elevated intra-ocular pressure is a risk factor for glaucoma, but the fact that glaucoma occurs in patients without elevated intra-ocular

pressure emphasizes that other factors than elevated intra-ocular pressure also play a role.

Both in patients with elevated and normal intra-ocular pressure, the disease leads to irreversible damage of the ganglion cells. The axons of the ganglion cells, which are located in the retinal nerve fiber layer, disappear with progression of the disease. Damaged ganglion cells are not naturally replaced, and currently no medicine or treatment exists to add new ganglion cells. However, when the disease is detected in an early stage, it can be stabilized successfully with medication or surgery, usually by lowering the intra-ocular pressure.

Nerve fiber layer tissue loss may be preceded by changes in birefringence. Birefringence, an optical property, induces a phase retardation between two orthogonal polarization states that increases with thickness and with birefringence. It is a property that can be measured as a function of depth with polarization-sensitive optical coherence tomography. As ganglion cells become necrotic and axons in the retinal nerve fiber layer are replaced by a less organized and amorphous tissue composed of glial cells,¹ birefringence changes are expected to occur.

1.3 Prevalence and detection of glaucoma

Glaucoma is the world's second leading cause of blindness.^{6,7} More than 130,000 people in the United States are legally blind as a result of glaucoma.⁷ A person is considered legally blind when his best corrected visual acuity is 20/200, or the person's visual field is 20 degrees or less. If a patient has a visual acuity of 20/200, the smallest letter he sees at 20 feet can be seen by a normal eye at 200 feet. In the metric system, such a visual acuity equals 0.1. Open angle glaucoma, or primary open angle glaucoma, is the most common type of glaucoma, and its prevalence ranges from 1.5% (1997)⁷ to 3% (1978).⁸ Glaucoma is the leading cause of blindness in African Americans,⁹⁻¹³ and its prevalence in African Americans ranges from 1.2% in the 40-49 year old age group to 11.3% in the age group above 80 years.¹² Since up to half of the patients are under-diagnosed, even in developed countries, the above numbers are probably on the low side.¹⁴⁻¹⁸

As discussed before, elevated intra-ocular pressure is a risk factor for glaucoma. Other risk factors for glaucoma are old age (>70 years),^{10, 12, 15, 16, 18-22} African descent,^{10, 12, 15} and family history (a family member having glaucoma).^{18, 23, 24} In the U.S. alone, three to six million people (including 4-7% of the age group above 40 years) have elevated intra-ocular pressure without detectable glaucomatous damage in standard clinical tests.²⁵⁻²⁷

In order to prevent glaucoma from developing in these risk-groups, early detection is crucial. If glaucoma happens instantaneously, in case of so-called acute glaucoma, glaucoma can be very painful. A case of acute glaucoma may be accompanied by a loss of vision, a strong signal for the patient to consult a doctor.

Acute glaucoma is therefore easy to detect and can be treated aggressively. In contrast, almost all other types of glaucoma are painless and are not accompanied by a sudden vision loss. Since the brain disregards blind spots and the disease progresses very slowly, glaucoma is difficult to detect by the patients themselves.

The current gold standard for glaucoma detection is the visual field test. In this test, the subject fixates on the center of a white dome after which a bright spot is projected on the dome's wall. A button has to be pressed as soon as the subject detects a spot using peripheral vision. A computer changes the location of the spot, and registers the subject's output. "Blind spots" occur at locations where the photoreceptors are not connected to the optic nerve, or where the ganglion cells are damaged. The subject is blind at these locations. Nerve fiber layer thinning caused by glaucoma may occur up to six years prior to clinically detectable loss of vision with the visual field test.²⁸ Moreover, up to 40% of the nerves can be irreversibly lost before the visual field test detects glaucoma.^{1, 28-30} The visual field test is a highly subjective test, since it requires subjective input from both the subject and operator. The subject may not be able to participate sufficiently and the operator subjectively translates the results of the visual field test to actual nerve fiber layer damage.

Recently, several commercial objective measurement methods for non-invasive glaucoma detection have emerged. These methods aim to measure nerve fiber layer thickness, nerve fiber retardation, or nerve fiber layer morphology, and do not require any input from the subject.

Scanning laser ophthalmoscope (SLO)

The scanning laser ophthalmoscope (SLO),^{31, 32} which is also known by the commercial names Heidelberg Retinal Tomograph (HRT II, Heidelberg Instruments, Heidelberg, Germany) and Topographic Scanning System (TopSS, Laser Diagnostic Technologies Inc.*, San Diego, CA, USA) is based on confocal microscopy and measures the three-dimensional appearance of the optic nerve head. The morphology of the optic nerve head is affected by glaucoma, and by recording parameters such as the optic disc diameter and cup-to-disc ratio, the instrument supplies objective numbers that can be used for glaucoma diagnosis.

The scanning laser ophthalmoscope consists of a laser source, a scanning mechanism (usually a polygon scanner for fast axis scanning and a galvanometer mirror for slow axis scanning) and a detector behind a pinhole. The pinhole rejects light from layers above and below the focus, thus creating depth-sectioning capability. The human eye has a rather large confocal parameter, since its focal length is approximately 17 *mm*. Even for a maximum beam diameter of 7 *mm*, for dilated eyes, the confocal parameter is only 100-200 μm . This means that the depth resolution as achieved with the scanning laser ophthalmoscope is rather limited. Another limitation

* currently Carl Zeiss Meditec, Dublin, CA

of this modality is that correct measurement of disc topography and associated indices depends on subjective input from the operator, as well as upon intra-ocular pressure and cardiac pulsations.³³

Scanning laser polarimeter (SLP)

The scanning laser polarimeter (SLP) combines the scanning laser ophthalmoscope with a polarization sensitive measurement to measure phase retardation. A product line of commercial nerve fiber layer analyzers has been marketed by Laser Diagnostic Technologies Inc.*, San Diego, CA, USA. The GDx VCC is the most recent version of this line. The microtubules and axon membranes in the nerve fiber layer are birefringent and polarized light that passes through the nerve fiber layer will experience a phase retardation.³⁴ Most of the incident light is reflected from layers beneath the retinal nerve fiber layer, thus double passing the full thickness of the nerve fiber layer.³⁵ The light returning from the eye is analyzed to calculate the phase retardation. As the retinal nerve fiber layer thins due to glaucoma, the amount of phase retardation is reduced. By comparing phase retardation plots from the patient as a function of time, or comparing values with a normative database, glaucoma can be detected. However, the cornea and lens are birefringent, inducing an unknown amount of phase retardation that varies from person to person, making an RNFL phase retardation measurement with SLP unreliable. To overcome this problem, the GDx was recently equipped with a variable corneal compensator (VCC).³⁶

Optical coherence tomography (OCT)

Carl Zeiss Meditec Inc. (Dublin, CA, USA) markets OCT systems for ophthalmic applications. We will explain the OCT technology more elaborately in Chapter 2. It uses spatially coherent light with a low temporal coherence (i.e. broad bandwidth) to make two-dimensional scans of the retina, as in histology. The latest version marketed by Zeiss, the Stratus OCT or OCT-3 has an axial resolution of approximately 10 μm and a lateral resolution of approximately 20-30 μm . Compared to the scanning laser ophthalmoscope and the scanning laser polarimeter, OCT – assuming a constant and correct index of refraction for the retinal nerve fiber layer - is the only system that measures nerve fiber layer thickness.

Comparison of instruments for glaucoma detection

The instruments described above have been compared to each other, or to less objective methods such as red-free photography and perimetry in several studies. However, due to the fast pace of development and improvement of these

* currently Carl Zeiss Meditec, Dublin, CA

instruments, studies become outdated with the introduction of new instrument versions. For instance, the performance of the GDx improved considerably with the introduction of the GDx VCC and the axial resolution of the OCT-3 improved from approximately 15 μm (OCT-1 and 2) to 10 μm . Recently, Medeiros *et al.*² concluded that there was no statistically significant difference between the ability of the most recent versions of the instruments described above to discriminate between normals and glaucoma patients. The following values were reported: GDx VCC, sensitivity 91% at 95% specificity; Stratus OCT-3 sensitivity 92% at 95% specificity; HRT II, sensitivity 86% at 95% specificity. Sensitivity refers to the proportion of subjects with glaucoma who were diagnosed correctly, while specificity refers to the proportion of healthy subjects who had a negative test results. A score of 100% (100% sensitivity and 100% specificity) was not achieved with any of the methods, which practically means that some patients will not receive the proper treatment when diagnosed with any of these instruments alone.

The next step in glaucoma detection would be to have an instrument that could detect glaucoma reliably before any of the currently known methods (including red-free photography and perimetry), since this will truly affect patient care. Patients that are at risk for glaucoma would not have to use any preventive treatment until the disease has been detected.

1.4 Aim of this thesis

Two methods for early detection of glaucoma are proposed in this thesis. Both methods are based on optical coherence tomography. Polarization-sensitive optical coherence tomography (PS-OCT) combines the depth resolution of OCT with the polarization sensitivity of scanning laser polarimetry to image the depth-resolved optical birefringence of biological tissue.³⁷⁻⁴³ The retinal nerve fiber layer is slightly birefringent because of its ordered structure,³⁴ but birefringence is absent in layers that are located below the retinal nerve fiber layer, including the ganglion cell layer. We hypothesize that glaucomatous loss of nerve fiber tissue may be preceded by a change in birefringence, since it is suspected that disintegration of the nerve fiber mesh leads to a change of retinal nerve fiber layer birefringence. Such a change in birefringence compared with normal levels could be an early sign of glaucomatous atrophy of the retinal nerve fiber layer. Experiments - for instance, a longitudinal study with polarization-sensitive OCT on patients at high-risk for development of glaucoma - will either confirm or reject this hypothesis. In addition, polarization-sensitive OCT may enhance specificity in determining retinal nerve fiber layer thickness in structural OCT images, by using changes in tissue birefringence to determine the border between the retinal nerve fiber layer and ganglion cell layer.

Compared to ordinary OCT, also known as time-domain OCT, spectral-domain OCT is a much more sensitive technique. This higher sensitivity can be used to either

improve the image quality, or to acquire more data in the same time span. It allows a shift from two-dimensional scanning to three-dimensional or volume scanning.

The combination of these two technologies, spectral-domain OCT with polarization-sensitive OCT, leads to an ultra-fast system that can determine the depth-resolved birefringence of the retina. Since older glaucoma patients may have difficulties fixating their eyes, short acquisition times are crucial for successful application. We will demonstrate that spectral-domain polarization-sensitive OCT is suitable for measurements in glaucoma patients, and compare results obtained from a healthy patient with those obtained from a glaucoma patient.

In Chapter 2, the optical interface between the eye and these two OCT systems will be discussed. This optical interface is crucial for the acquisition of high-quality data, and will be used in Chapters 3 to 5. Chapter 3 is devoted to polarization-sensitive OCT, while the latest developments in spectral-domain OCT are described in Chapter 4. Finally, in Chapter 5 we describe a spectral-domain polarization-sensitive OCT system and discuss preliminary measurements with this method.

References

1. H.A. Quigley, E.M. Addicks and W.R. Green, "Optic nerve damage in human glaucoma. III. Quantitative correlation of nerve fiber loss and visual field defect in glaucoma, ischemic neuropathy, papilledema, and toxic neuropathy," *Archives of Ophthalmology*, 100, 135-46 (1982).
2. F.A. Medeiros, L.M. Zangwill, C. Bowd and R.N. Weinreb, "Comparison of the GDx VCC scanning laser polarimeter, HRT II confocal scanning laser ophthalmoscope, and stratus OCT optical coherence tomograph for the detection of glaucoma," *Archives of Ophthalmology*, 122, 827-837 (2004).
3. S.S. Hayreh, "Blood Supply of Optic Nerve Head and Its Role in Optic Atrophy, Glaucoma, and Oedema of Optic Disc," *British Journal of Ophthalmology*, 53, 721-& (1969).
4. H.A. Quigley, R.W. Nickells, L.A. Kerrigan, et al., "Retinal Ganglion-Cell Death in Experimental Glaucoma and after Axotomy Occurs by Apoptosis," *Investigative Ophthalmology & Visual Science*, 36, 774-786 (1995).
5. H.A. Quigley and W.R. Green, "The Histology of Human Glaucoma Cupping and Optic-Nerve Damage - Clinicopathologic Correlation in 21 Eyes," *Ophthalmology*, 86, 1803-1830 (1979).
6. The International Bank for Reconstruction and Development - the World Bank. World Development Report. 1993, Oxford: Oxford University Press.
7. H.A. Quigley and S. Vitale, "Models of open-angle glaucoma prevalence and incidence in the United States," *Investigative Ophthalmology & Visual Science*, 38, 83-91 (1997).
8. M.M. Kini, H.M. Leibowitz, T. Colton, et al., "Prevalence of senile cataract, diabetic retinopathy, senile macular degeneration, and open-angle glaucoma in the Framingham eye study," *American Journal of Ophthalmology*, 85, 28-34 (1978).
9. A. Sommer, J.M. Tielsch, J. Katz, et al., "Racial differences in the cause-specific prevalence of blindness in east Baltimore," *New England Journal of Medicine*, 325, 1412-7 (1991).
10. R.P. Mason, O. Kosoko, M.R. Wilson, et al., "National survey of the prevalence and risk factors of glaucoma in St. Lucia, West Indies. Part I. Prevalence findings," *Ophthalmology*, 96, 1363-8 (1989).
11. J. Wallace and H.G. Lovell, "Glaucoma and intraocular pressure in Jamaica," *American Journal of Ophthalmology*, 67, 93-100 (1969).

12. J.M. Tielsch, A. Sommer, J. Katz, et al., "Racial variations in the prevalence of primary open-angle glaucoma. The Baltimore Eye Survey," *JAMA*, 266, 369-74 (1991).
13. M.C. Leske, A.M. Connell, S.Y. Wu, et al., "Incidence of open-angle glaucoma: the Barbados Eye Studies. The Barbados Eye Studies Group," *Archives of Ophthalmology*, 119, 89-95 (2001).
14. I. Dielemans, J.R. Vingerling, R.C. Wolfs, et al., "The prevalence of primary open-angle glaucoma in a population-based study in The Netherlands. The Rotterdam Study," *Ophthalmology*, 101, 1851-5 (1994).
15. M.C. Leske, A.M. Connell, A.P. Schachat and L. Hyman, "The Barbados Eye Study. Prevalence of open angle glaucoma," *Archives of Ophthalmology*, 112, 821-9 (1994).
16. P. Mitchell, W. Smith, K. Attebo and P.R. Healey, "Prevalence of open-angle glaucoma in Australia. The Blue Mountains Eye Study," *Ophthalmology*, 103, 1661-9 (1996).
17. A.J. King, A. Reddy, J.R. Thompson and A.R. Rosenthal, "The rates of blindness and of partial sight registration in glaucoma patients," *Eye*, 14, 613-9 (2000).
18. A.L. Coleman, "Glaucoma," *Lancet*, 354, 1803-10 (1999).
19. Y. Shiose, Y. Kitazawa, S. Tsukahara, et al., "Epidemiology of glaucoma in Japan--a nationwide glaucoma survey," *Japanese Journal of Ophthalmology*, 35, 133-55 (1991).
20. B.E. Klein, R. Klein, W.E. Sponsel, et al., "Prevalence of glaucoma. The Beaver Dam Eye Study," *Ophthalmology*, 99, 1499-504 (1992).
21. M. Coffey, A. Reidy, R. Wormald, et al., "Prevalence of glaucoma in the west of Ireland," *British Journal of Ophthalmology*, 77, 17-21 (1993).
22. M.D. Wensor, C.A. McCarty, Y.L. Stanislavsky, P.M. Livingston and H.R. Taylor, "The prevalence of glaucoma in the Melbourne Visual Impairment Project," *Ophthalmology*, 105, 733-9 (1998).
23. J.M. Tielsch, J. Katz, A. Sommer, H.A. Quigley and J.C. Javitt, "Family history and risk of primary open angle glaucoma. The Baltimore Eye Survey," *Archives of Ophthalmology*, 112, 69-73 (1994).
24. R.C. Wolfs, C.C. Klaver, R.S. Ramrattan, et al., "Genetic risk of primary open-angle glaucoma. Population-based familial aggregation study," *Archives of Ophthalmology*, 116, 1640-5 (1998).
25. H.M. Leibowitz, D.E. Krueger, L.R. Maunder, et al., "The Framingham Eye Study monograph: An ophthalmological and epidemiological study of cataract, glaucoma, diabetic retinopathy, macular degeneration, and visual acuity in a general population of 2631 adults, 1973-1975," *Survey of Ophthalmology*, 24, 335-610 (1980).
26. M.F. Armaly, D.E. Krueger, L. Maunder, et al., "Biostatistical analysis of the collaborative glaucoma study. I. Summary report of the risk factors for glaucomatous visual-field defects," *Archives of Ophthalmology*, 98, 2163-71 (1980).
27. H.A. Quigley, C. Enger, J. Katz, et al., "Risk factors for the development of glaucomatous visual field loss in ocular hypertension," *Archives of Ophthalmology*, 112, 644-9 (1994).
28. A. Sommer, J. Katz, H.A. Quigley, et al., "Clinically detectable nerve fiber atrophy precedes the onset of glaucomatous field loss," *Archives of Ophthalmology*, 109, 77-83 (1991).
29. L.A. Kerrigan-Baumrind, H.A. Quigley, M.E. Pease, D.F. Kerrigan and R.S. Mitchell, "Number of ganglion cells in glaucoma eyes compared with threshold visual field tests in the same persons," *Investigative Ophthalmology & Visual Science*, 41, 741-8 (2000).
30. R.D. Reyes, G. Tomita and Y. Kitazawa, "Retinal nerve fiber layer thickness within the area of apparently normal visual field in normal-tension glaucoma with hemifield defect," *Journal of Glaucoma*, 7, 329-35 (1998).
31. R.H. Webb, G.W. Hughes and O. Pomerantzeff, "Flying Spot Tv Ophthalmoscope," *Applied Optics*, 19, 2991-2997 (1980).
32. R.H. Webb, G.W. Hughes and F.C. Delori, "Confocal Scanning Laser Ophthalmoscope," *Applied Optics*, 26, 1492-1499 (1987).
33. E.Z. Blumenthal and R.N. Weinreb, "Assessment of the retinal nerve fiber layer in clinical trials of glaucoma neuroprotection," *Survey of Ophthalmology*, 45, S305-12; discussion S332-4 (2001).
34. X.R. Huang and R.W. Knighton, "Linear birefringence of the retinal nerve fiber layer measured in vitro with a multispectral imaging micropolarimeter," *Journal of Biomedical Optics*, 7, 199-204 (2002).

35. J.S. Schuman, M.R. Hee, C.A. Puliafito, et al., "Quantification of nerve fiber layer thickness in normal and glaucomatous eyes using optical coherence tomography," *Archives of Ophthalmology*, 113, 586-96 (1995).
36. Q.Y. Zhou and R.N. Weinreb, "Individualized compensation of anterior segment birefringence during scanning laser polarimetry," *Investigative Ophthalmology & Visual Science*, 43, 2221-2228 (2002).
37. J.F. de Boer, T.E. Milner, M.J.C. van Gemert and J.S. Nelson, "Two-dimensional birefringence imaging in biological tissue by polarization-sensitive optical coherence tomography," *Optics Letters*, 22, (1997).
38. J.F. de Boer, T.E. Milner and J.S. Nelson, "Determination of the depth-resolved Stokes parameters of light backscattered from turbid media by use of polarization-sensitive optical coherence tomography," *Optics Letters*, 24, 300-302 (1999).
39. C.E. Saxer, J.F. de Boer, B.H. Park, et al., "High-speed fiber-based polarization-sensitive optical coherence tomography of in vivo human skin," *Optics Letters*, 25, 1355-1357 (2000).
40. B.H. Park, C. Saxer, S.M. Srinivas, J.S. Nelson and J.F. de Boer, "In vivo burn depth determination by high-speed fiber-based polarization sensitive optical coherence tomography," *Journal of Biomedical Optics*, 6, 474-9 (2001).
41. B. Cense, T.C. Chen, B.H. Park, M.C. Pierce and J.F. de Boer, "In vivo depth-resolved birefringence measurements of the human retinal nerve fiber layer by polarization-sensitive optical coherence tomography," *Optics Letters*, 27, 1610-1612 (2002).
42. B. Cense, T.C. Chen, B.H. Park, M.C. Pierce and J.F. de Boer, "In vivo birefringence and thickness measurements of the human retinal nerve fiber layer using polarization-sensitive optical coherence tomography," *Journal of Biomedical Optics*, 9, 121-125 (2004).
43. B. Cense, T.C. Chen, B.H. Park, M.C. Pierce and J.F. de Boer, "Thickness and birefringence of healthy retinal nerve fiber layer tissue measured with polarization-sensitive optical coherence tomography," *Investigative Ophthalmology & Visual Science*, 45, 2606-2612 (2004).

2. Slit lamp-based ophthalmic imaging with optical coherence tomography

*Abstract**

Eye measurements with optical coherence tomography (OCT) require a special interface. Great care was paid to the construction of such an interface, designed around pupil and image planes, making stable measurements of the retina possible. Furthermore, the volunteer's eye could be stabilized by means of a fixation spot and different areas of the retina could be imaged. The addition of a charged coupled device (CCD) camera to the setup allowed for an optimization of the location of OCT scans on the retina.

* This chapter was partly published in the following three peer-reviewed articles:

B. Cense, T.C. Chen, B.H. Park, M.C. Pierce and J.F. de Boer, "In vivo depth-resolved birefringence measurements of the human retinal nerve fiber layer by polarization-sensitive optical coherence tomography," *Optics Letters*, 27, 1610-1612 (2002).

B. Cense, T.C. Chen, B.H. Park, M.C. Pierce and J.F. de Boer, "In vivo birefringence and thickness measurements of the human retinal nerve fiber layer using polarization-sensitive optical coherence tomography," *Journal of Biomedical Optics*, 9, 121-125 (2004).

B. Cense, N.A. Nassif, T.C. Chen, et al., "Ultrahigh-resolution high-speed retinal imaging using spectral-domain optical coherence tomography," *Optics Express*, 12, 2435-2447 (2004).

2.1 Introduction

A crucial part of every setup for optical coherence tomography is the interface with the sample tissue. For easily accessible tissue such as the human skin, this can be a hand piece, and for internal organs such as the human esophagus and the vocal cords an optical catheter is the optimal interface. For the human eye, a special interface is necessary. The eye is one of our most sensitive organs. It reacts to light by opening and closing of the iris. The visual system induces involuntary eye motion to improve visual acuity, but a negative side effect for retinal imaging is that the retina experiences small lateral shifts, decreasing the image quality. The human cardiac and respiratory cycle affect the eye's stability even more. A stable eye is crucial for ophthalmic imaging. The optics of the eye, such as the lens and cornea pose another problem. In order to cover an area of the retina with a scan, a special interface is required for retinal measurements with OCT. After discussing the basics of time-domain optical coherence tomography, the necessary steps to make a setup suitable for ophthalmic imaging with OCT will be described.

2.2 Principle of time-domain OCT

Optical coherence tomography^{1, 2} is a non-invasive measurement method that uses light with low temporal coherence to create two- and three dimensional tomograms of biological tissue *in vivo* such as the retina,³ skin,⁴ esophagus⁵ and coronary artery.⁶

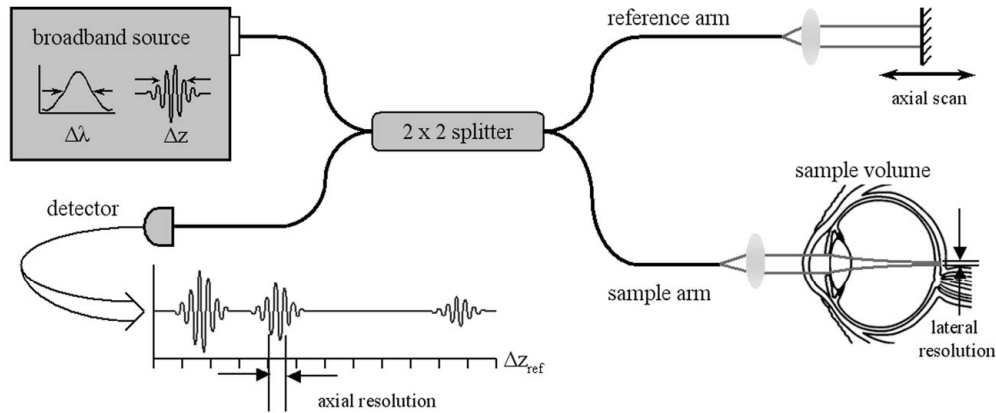


Figure 3: Schematic of a fiber-based setup for optical coherence tomography. Light from a broadband source is divided between reference and sample arms. The optical path length of the reference arm is modulated, and light returning from the two arms is recombined in the 50/50 splitter. Fifty percent of the light goes to the detector arm. A photosensitive detector records interference fringes only when the lengths of sample and reference arms match to within one coherence length. A color image can be found on page 119.

An OCT system is built around an interferometer, usually a Michelson interferometer, and consists of a source-, sample-, reference- and detector arm. In the source arm, a broadband source emits light with different wavelengths (low temporal coherence), preferably spatially confined. An optical isolator may be used to protect the source from back reflection. The source light enters the interferometer, where it is split between the sample and reference arms. In the first OCT systems a 50/50 splitter was used, where 50% of the power was sent towards the reference arm and 50% towards the sample arm. The reference arm's main component is a mirror and the arm is constructed such that its optical path length can be modulated rapidly. It may also contain a means of dispersion compensation, as in a rapid scanning delay line,⁷ or glass prisms with different indices of refraction.⁸ The sample arm comprises an interface that permits one- or two-dimensional optical scanning of (human) tissue. To simplify Figure 3, a lens replaces the interface. In section 2.3 a slit lamp based interface for ophthalmic imaging will be discussed in detail.

Light that reflects from the reference mirror interferes with light returning from the tissue in the sample arm. Constructive interference may occur when the optical path lengths of sample and reference arms match within one coherence length (l_{coh}). In all other cases, the interference is not constructive such that no interference fringes occur. A second condition is that the sample reflects light at that particular depth. In the return path, the interference signal is again split between source and detector arms, and when using a 50/50 splitter, a maximum of only 25% of the source power can be used efficiently. The efficiency of modern fiber-based OCT system can be improved in several ways. For most applications, especially those that use a center wavelength of 1310 nm (skin, esophagus, coronary artery) the efficiency can be improved by combining an optical circulator with a fiber coupler.⁹ In these applications, the tissue can withstand high optical intensity, up to several mW. For ophthalmic applications however, the amount of power at a wavelength of 800 nm that can be sent towards the eye is limited to 610 μ W by ANSI standards.¹⁰ One can optimize the efficiency of the system by using a splitting ratio different from 50/50. The smaller amount, preferably close to ANSI standard limits, is sent towards the eye, and upon return a relatively large amount can be detected in the detection arm. For instance, when using a 70/30 splitter,¹¹ 70% of the light returning from the eye is available for interference.

An optical detector in the detection arm registers the optical signal returning from the interferometer. The detected information is stored on a PC and can be analyzed in real time¹² or with post-processing. As the optical path length in the reference arm cycles between shortest and longest possible lengths, a so-called A-line is registered in the detection arm. By scanning the position of the beam in the sample arm in one direction, a two-dimensional scan or B-scan can be made. A second axis in the sample arm can be used to image a three-dimensional volume.

The image quality of an OCT image depends on several factors, most importantly the signal-to-noise ratio (SNR) and the resolution. In Chapter 4 we will discuss the SNR of OCT systems in detail. The lateral resolution of an OCT system depends on the imaging optics. With use of high numerical aperture lenses, small spot sizes can be generated, improving the lateral resolution. For instance, when one combines a Gaussian beam at wavelength λ with a lens with a focal length f and filled aperture D_{beam} , a $1/e^2$ spot size $2\omega_0$ is created according to:

$$2\omega_0 = \frac{4 \cdot \lambda \cdot f}{\pi \cdot D_{beam}} \quad \text{Eq. 1}$$

The axial resolution of an OCT system is defined as its coherence length l_{coh} related to the center wavelength of the source λ_0 and its bandwidth $\Delta\lambda$,¹³ and is determined at the full width at half maximum (FWHM) of the coherence function, which is assumed to be shaped like a Gaussian distribution:

$$l_{coh} = \frac{2 \ln 2 \cdot \lambda_0^2}{n \cdot \pi \cdot \Delta\lambda} \quad \text{Eq. 2}$$

The coherence length of a source is in general quantified by measuring a reflection from a reflector, for instance a mirror or a microscope slide. For such a measurement, the scanning mechanism that generates two- or three-dimensional volumes is not run. An example of a coherence length measurement can be found in Figure 4B, where we used a high-power superluminescent diode (SLD-317-HP, Superlum, Russia) in the source arm. The graph shows the interference intensity (vertical axis) recorded with an optical detector, while varying the path length difference (horizontal axis). The high-frequency modulation of the coherence function was caused by the rapid scanning delay line in the measurement setup, and does not affect the coherence function measurement. The source spectrum is depicted in Figure 4A. With a center wavelength of approximately 839 nm and an optical bandwidth of 50 nm , the coherence length in water ($n = 1.33$) becomes 4.7 μm according to Eq. 2.

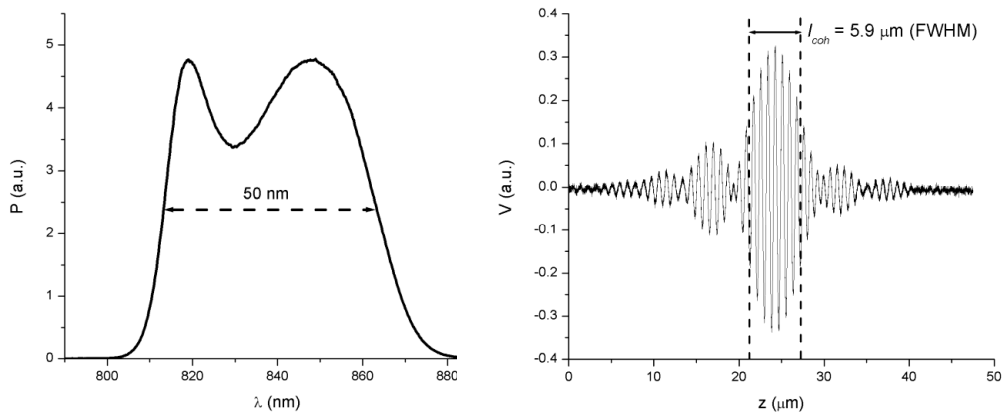


Figure 4: Spectrum of a high-power superluminescent diode (SLD-371-HP, Superlum, Russia) on the left and its coherence function measured from a mirror in a water-filled model eye on the right. Both the power of the source spectrum and the measured coherence function are specified in arbitrary units. The spectral width of the SLD was 50 nm, and a coherence length (l_{coh}) of 5.9 μm (FWHM) was measured in water. The high frequency modulation in the coherence function graph was induced by the rapid scanning delay line. This modulation does not affect the coherence length measurement.

Comparing the theoretical result of 4.7 μm with the measured result of 5.9 μm , we find a difference of 20%. With a Gaussian-shaped source spectrum the difference would have been smaller, and the side lobes that are currently visible would not be present.

The eye behind the pupil is highly transparent for visible light, as well as near infra red light. If we model the eye as a volume of water,¹⁴ it absorbs NIR radiation starting at wavelengths of approximately 920 nm and continuing well into the infra red. For retinal measurements, a center wavelength of 800-830 nm is seen as ideal, since it transmits well through the vitreous and ANSI standards allow a much higher intensity than for visible wavelengths.¹⁰ For instance, at 600 nm, the maximum permissible exposure rate is equal to approximately 80 μW . Furthermore, powerful commercial broadband sources such as SLDs and titanium sapphire lasers are widely available at a center wavelength of 830 nm. Another center wavelength commonly used for OCT is 1310 nm. This wavelength is particularly suitable for corneal measurements,¹⁵ but does not transmit well enough through the vitreous to create images of the human retina. For instance, only 5% of the power incident on the cornea reaches the retina after transmission through 20 mm of vitreous. Upon double-pass and assuming a perfectly reflecting retina, only less than 0.5% returns at 1310 nm, see also Figure 5.¹⁶

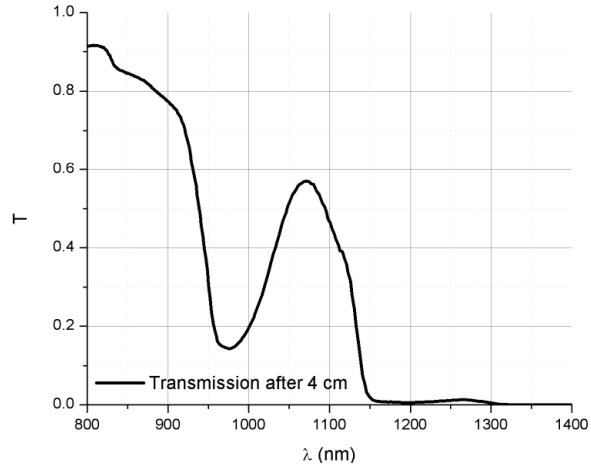


Figure 5: The transmission of light through 4 *cm* of water (double-passing the vitreous in the human eye) as a function of wavelength. The most transmissive window ends around 920 *nm*, and beyond 1150 *nm* the transmission is negligible.

2.3 Slit lamp interface

A slit lamp is an instrument commonly used by ophthalmologists for routine corneal and retinal exams and consists of a bio-microscope on a movable table with a headrest. The operation of the instrument is fairly simple. The patient's head is stabilized by a chin- and head rest, after which the microscope can be brought towards the eye. In its basic form, the bio-microscope can be used to inspect the front of the eye, i.e. the cornea. Well-balanced illumination is vital for a good result. Too much light may irritate the patient, while low light levels result in a dark image. An illuminated slit can be imaged onto the cornea, for instance for inspection of the tear film. This special type of illumination gives the system its name. Combined with an ophthalmic lens the slit lamp can be used to image the retina. Light that returns from the retina through the unaccommodated lens and cornea of an eye with perfect vision is collimated. By means of the ophthalmic lens, this collimated light is focused on the image plane of the slit lamp, at the previous position of the cornea during normal operation. One can compensate for defocus in myopic eyes by shifting the position of the ophthalmic lens closer or further away from the image plane.

We combined a slit lamp with a NIR-sensitive charged coupled device (CCD) camera, a retinal scanner and an OCT system, so that we could make OCT images of the retina while simultaneously keeping track of involuntary retinal motion with the CCD camera.¹¹ To stabilize the eye, we offered a fixation spot to the volunteer's eye that was under investigation.¹⁷

The system was built around image- and pupil planes, necessary for the creation of high quality images of the optic nerve head in the retinal image plane, while scanning through a narrow iris, the pupil plane. The area of interest for the OCT scan and CCD camera was the area around the optic nerve head. The fixation spot was tilted such that the optic nerve head aligned with the optic axis of the CCD camera when the subject looked at the fixation spot. In this design, the OCT beam, the fixation spot beam, the illumination beam and the optic axis of the CCD camera have to overlap as much as possible in the pupil plane. Both the OCT beam and the fixation beam are collimated in the pupil plane. Their diameters are small compared to the size of the iris. The illumination beam is slightly focused in this plane, so that it can pass through a narrow iris. In the following schematic, the beam distribution at the pupil is given.

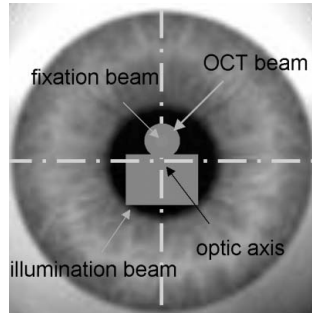


Figure 6: Reconstruction of the pupil plane. The fixation beam, OCT beam and illumination beam pass through the pupil. The fixation beam and OCT beam are slightly offset with respect to the optic axis of the CCD camera (crossed lines), while the illumination beam slightly overlaps with this axis. A color image can be found on page 120.

In the image plane, the illumination beam diverges (Figure 7), while both the OCT beam and fixation beam are focused on the retina. Although the fixation beam and OCT beam overlapped in the pupil plane, the fixation spot in the image plane was located in the fovea, while the OCT beam was scanned around the optic nerve head. This image plane was reconstructed using two fundus camera images (not taken with our system) and an image taken with our CCD camera of the area around the optic nerve head. Fundus images and the CCD image were taken from the same eye of the same volunteer. As can be seen in Figure 7, the field of view of the CCD camera was rather limited, but sufficient for proper location of the OCT beam and registration of eye motion. The fixation spot was artificially added in this image. The illumination slit is much smaller than the illumination used for the fundus camera, leaving half of the CCD image dark. Later, we will come back to this issue.

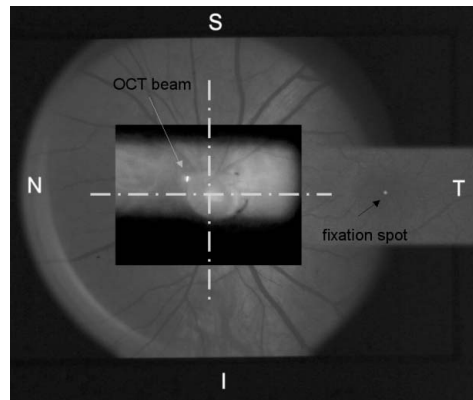


Figure 7: A composition of fundus images of the area around the optic nerve head (left) and around the fovea (right), both in color. The field of view of the CCD camera was much smaller than the field of view of the fundus camera, with an even smaller illuminated field. The cross indicates the position of the optic axis of the CCD camera. The fixation spot was added artificially. A color image can be found on page 120.

Figure 8 gives a schematic representation of the optics in the slit lamp-based retinal scanner. As explained before, the slit lamp was located in the sample arm of our fiber-based OCT system, and was connected with the OCT system by a single mode fiber. After source light entered the slit lamp, it was first collimated. The collimated beam was XY raster scanned with two closely spaced galvanometer mirrors, one for each direction. The short distance between the two galvanometers was important as the exiting beam virtually came from a single point, such that the scanner became a pupil plane. The collimated beam was focused by means of a focusing lens on an image plane, after which the ophthalmic lens collimated it again just before the light entered the pupil. In order to use the image plane simultaneously for retinal inspection by means of a CCD camera, a dichroic mirror was positioned at 45 degrees between the focusing lens and the image plane. The optic axis of the CCD camera should overlap as much as possible with the pupil plane, for optimal efficiency for light entering the eye and reflecting from the retina. The dichroic mirror transmits visible light, necessary for visual illumination and monitoring, but reflects NIR light, the light that is used for OCT. The OCT beam that reflected off the dichroic mirror towards the image plane, ophthalmic lens, cornea and retina returned through the same path. A perfect dichroic mirror would not transmit any of the OCT light at 830 *nm* towards the CCD camera, making it impossible to monitor the OCT beam in the retina. Fortunately, the spectral window did not exactly match the spectrum of the source, and a very small part of the OCT beam was transmitted, allowing the OCT

beam to be seen at the retina. The sensitivity of the CCD camera was matched with respect to the available OCT beam spectrum and power by removing the standard NIR absorption filter and adding a short wave pass filter. This spectral filter left the image of the illuminated retina unaffected, but cut out enough power from the OCT beam such that it was clearly visible without saturation.

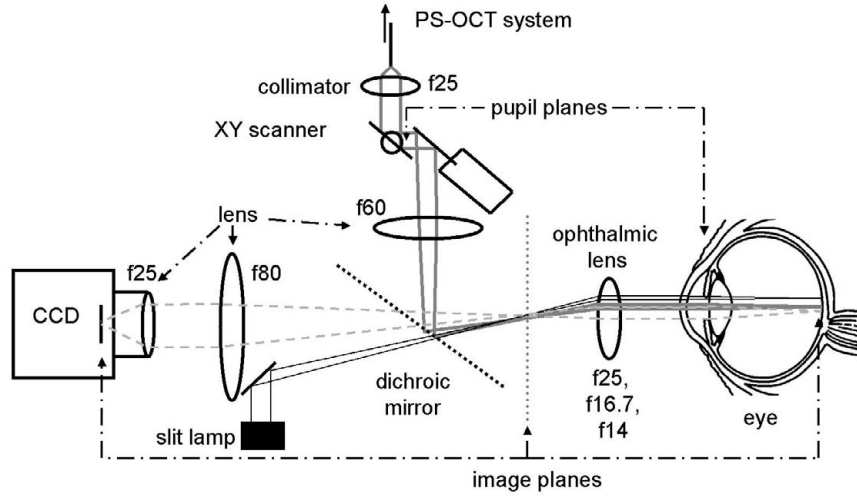


Figure 8: Schematic overview of the optical paths in the slit lamp. A single-mode fiber and collimator guided the OCT beam into an XY galvanometer scanner. An f_{60} lens focused the PS-OCT beam in the image plane. The XY galvanometer scanner was located in the back focal plane of this lens. The ophthalmic lens imaged the PS-OCT spot from the image plane onto the retina. Ophthalmic lenses with a variety of focal lengths could be used here. During scanning, the sample beam pivoted in the pupil plane, positioned near the corneal surface. The incident and returning OCT beam follow the same path. The retina was illuminated by the incandescent source of the slit lamp. The ophthalmic lens formed an image of the retina in the image plane, which was projected on the CCD chip through a dichroic splitter, transparent for visible light and highly reflective for near-infrared light. To avoid specular reflections that decreased the quality of recorded video images, the OCT beam and the illumination beam propagated off-axis through the ophthalmic lens. The hardware necessary for a fixation spot is not shown in this particular image and will be discussed later.

2.3.1 Optimal spot size and magnification

The image quality of an ophthalmic OCT image strongly depends on the amount of light that returns from the retina back into the OCT system. In a perfect eye, a collimated beam is focused down to a diffraction-limited spot and its spot size decreases with increasing beam diameter as described earlier by Eq. 1. In addition, the amount of light that returns from the retina will increase too with beam diameter, since more of the returning cone of light is collected by the optical system. In practice,

aberrations in the eye limit the useful diameter of the collimated beam, with an optimum beam diameter of approximately 1.5 to 2 *mm*.¹⁸

2.3.2 Retinal illumination

A well-balanced retinal illumination is vital for a good view of the retina. A photographic camera with a flashlight may cause a “red eye effect”. The redness is caused by a reflection from the retina, which strongly reflects in the red. More expensive photo cameras that have a larger distance between the flashlight and the camera’s aperture will not suffer from the red eye effect, since the light that enters the eye does not reflect back towards the camera. In this sense, the slit lamp can be compared to a cheap photo camera. Obviously, the slit lamp has a constant and much less intense source, but both have in common the fact that the axis of illumination overlaps with the imaging axis. One problem that arises from this design is that reflections in the ophthalmic lens are likely. This ophthalmic lens is the last lens in the slit lamp before the light enters the eye. A small percentage of the light reflects from the ophthalmic lens’ surface towards the CCD camera. Such a specular reflection can be bright enough to seriously distort the visual image. To avoid this problem, the light was sent at an angle towards the ophthalmic lens, as can be seen in Figure 8. A disadvantage of this approach is that since both the OCT and illumination beams do not overlap with the optic axis of the CCD camera, dilated eyes with a large pupil are crucial for simultaneous visual inspection and OCT imaging. For undilated eyes, one can also chose to overlap all beams, and remove specular reflections from the ophthalmic lens with crossed polarizers. One polarizer covers the illumination source, while the analyzer covers the camera. The disadvantage of this technique is that the reflections from the retina will be attenuated as well by the analyzer, resulting in lower contrast.

ANSI standards allow bright full field retinal illumination in the visible part of the spectrum, up to approximately 30 *mW*.¹⁰ However, such a high level is irritating for the eye, and may temporarily reduce vision. A practical value for the maximum amount of NIR light that can be sent towards the eye is 100 μ *W*. In order to reduce the intensity without reducing video image quality, the retina was illuminated with NIR light. The illumination spectrum ranged from approximately \sim 700-800 *nm*. Wavelengths above 800 *nm* were blocked by the dichroic mirror.

2.3.3 Fixation spot

The hardware for the fixation spot was mounted between the *f*25 and *f*80 lenses in front of the CCD camera (see Figure 9).

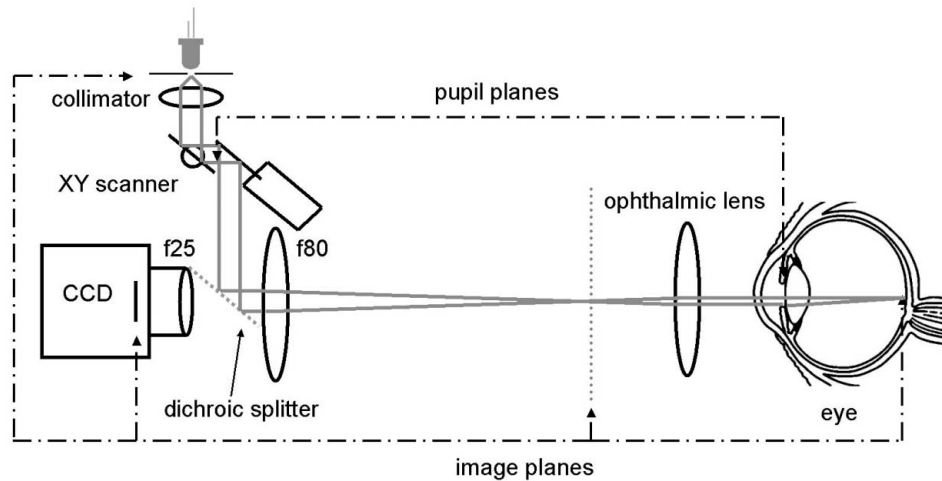


Figure 9: Design of the optical elements that were used to create a fixation spot. Collimated light from a pinhole, illuminated by a green LED, was deflected by two galvanometer scanners and a dichroic beam splitter and focused on the image plane. From there, an ophthalmic lens in combination with the optics of the eye focused the green light onto the retina.

The design of a scanner for the fixation spot is very similar to the design of the OCT scanner itself, since both scanner mechanisms have to create a small spot in the image plane of the retina, while pivoting through the pupil plane of the iris. A pinhole illuminated by a green LED was chosen as a target. Light from the pinhole was collimated and deflected by means of two galvanometer mirrors. These scanners were positioned in a virtual pupil plane. After being deflected from the scanner mirrors, a dichroic beam splitter coupled the light into the beam path in front of the CCD camera. This dichroic mirror reflects green light, but transmits red light, such that the red light returning from the retina could transmit through the dichroic towards the CCD camera. The green light was then focused by means of the f_{80} mm lens onto the image plane, after which it continued towards the ophthalmic lens.

In order to overlap with the OCT beam and illumination beam, the scanners for the fixation spot had to be mounted slightly off-axis. The fixation spot overlaps with the illumination when it enters the pupil. The eye sees a bright green spot, overlapped with a bright reddish glow that is caused by the retinal illumination. The position of the green spot can be shifted in the image plane by means of the galvanometer scanners. When the eye follows the spot, the OCT beam can probe large retinal areas such as the macular area and optic nerve head, while maintaining the same raster scanning pattern and position.

2.4 Adaptive ranging for motion compensation

The fixation spot described in 2.3.3 reduces involuntary motion of the eye perpendicular to the probing beam. Head motion due to the cardiac pulse or respiratory motion that is parallel to the direction of the probing beam cannot be avoided using the fixation spot. However, parallel motion can be counteracted by means of adaptive ranging (AR).¹⁹ This method detects the location of the retina and adjusts the reference delay-scanning offset so that the retinal data is always in the imaging window, even when the eye is shifted parallel to the direction of the probing beam. The AR technology operates in real-time and does not require major hardware modifications to conventional OCT systems.

2.5 Summary

OCT is a technology that uses light to make two- or three-dimensional scans of tissue. Compared to other parts of the human body, the retina of a transparent eye is relatively easy to access with OCT, but because of the optics of the eye a special interface is required. An ophthalmic interface was constructed around several image and pupil planes, where the main image plane is located at the position of the retina, and the main pupil plane is in the iris or pupil of the eye. The collimated OCT beam pivots in the pupil plane and is focused in the image plane, where it can be used to make area scans.

A spectral window between approximately 700 and 900 *nm* is optimal for OCT imaging of the human retina. The damage threshold of the eye decreases quickly below 700 *nm*, while water in the aqueous humor absorbs NIR light at wavelengths above 920 *nm*. Broadband sources, such as superluminescent diodes and titanium sapphire lasers are widely available in this range.

The alignment and focusing procedure of the beam on the retina becomes easier with use of a CCD camera and retinal illumination. A fixation spot in the image plane can be used to stabilize the eye and to find areas of interest on the retina.

References

1. D. Huang, E.A. Swanson, C.P. Lin, J.S. Schuman, W.G. Stinson, W. Chang, M.R. Hee, T. Flotte, K. Gregory, and C.A. Puliafito, "Optical coherence tomography," *Science* 254, 1178-81 (1991).
2. A.F. Fercher, C.K. Hitzenberger, W. Drexler, G. Kamp, and H. Sattmann, "In-Vivo Optical Coherence Tomography," *American Journal of Ophthalmology* 116, 113-115 (1993).
3. E.A. Swanson, J.A. Izatt, M.R. Hee, D. Huang, C.P. Lin, J.S. Schuman, C.A. Puliafito, and J.G. Fujimoto, "In-Vivo Retinal Imaging by Optical Coherence Tomography," *Optics Letters* 18, 1864-1866 (1993).
4. J.M. Schmitt, M.J. Yadlowsky, and R.F. Bonner, "Subsurface Imaging of Living Skin with Optical Coherence Microscopy," *Dermatology* 191, 93-98 (1995).

5. B.E. Bouma, G.J. Tearney, C.C. Compton, and N.S. Nishioka, "High-resolution imaging of the human esophagus and stomach in vivo using optical coherence tomography," *Gastrointestinal Endoscopy* 51, 467-474 (2000).
6. I.K. Jang, G.J. Tearney, D.H. Kang, Y.C. Moon, S.J. Park, S.W. Park, K.B. Seung, S.L. Houser, M. Shishkov, E. Pomerantsev, H.T. Aretz, and B.E. Bouma, "Comparison of optical coherence tomography and intravascular ultrasound for detection of coronary plaques with large lipid-core in living patients," *Circulation* 102, 509-509 (2000).
7. G.J. Tearney, B.E. Bouma, and J.G. Fujimoto, "High-speed phase- and group-delay scanning with a grating-based phase control delay line," *Optics Letters* 22, 1811-1813 (1997).
8. W. Drexler, U. Morgner, F.X. Kartner, C. Pitris, S.A. Boppart, X.D. Li, E.P. Ippen, and J.G. Fujimoto, "In vivo ultrahigh-resolution optical coherence tomography," *Optics Letters* 24, 1221-1223 (1999).
9. B.E. Bouma, and G.J. Tearney, "Power-efficient nonreciprocal interferometer and linear-scanning fiber-optic catheter for optical coherence tomography," *Optics Letters* 24, (1999).
10. A.N.S.I., Safe use of lasers. 1993, Laser Institute of America: New York.
11. B. Cense, T.C. Chen, B.H. Park, M.C. Pierce, and J.F. de Boer, "In vivo birefringence and thickness measurements of the human retinal nerve fiber layer using polarization-sensitive optical coherence tomography," *Journal of Biomedical Optics* 9, 121-125 (2004).
12. B.H. Park, M.C. Pierce, B. Cense, and J.F. de Boer, "Real-time multi-functional optical coherence tomography," *Optics Express* 11, 782-793 (2003).
13. E.A. Swanson, D. Huang, M.R. Hee, J.G. Fujimoto, C.P. Lin, and C.A. Puliafito, "High-Speed Optical Coherence Domain Reflectometry," *Optics Letters* 17, 151-153 (1992).
14. A.H. Harvey, J.S. Gallagher, and J. Sengers, "Revised formulation for the refractive index of water and steam as a function of wavelength, temperature and density," *Journal of Physical and Chemical Reference Data* 27, 761-774 (1998).
15. J.A. Izatt, M.R. Hee, E.A. Swanson, C.P. Lin, D. Huang, J.S. Schuman, C.A. Puliafito, and J.G. Fujimoto, "Micrometer-Scale Resolution Imaging of the Anterior Eye in-Vivo with Optical Coherence Tomography," *Archives of Ophthalmology* 112, 1584-1589 (1994).
16. K.F. Palmer, and D. Williams, "Optical-Properties of Water in near-Infrared," *Journal of the Optical Society of America* 64, 1107-1110 (1974).
17. B. Cense, T.C. Chen, B.H. Park, M.C. Pierce, and J.F. de Boer, "Thickness and birefringence of healthy retinal nerve fiber layer tissue measured with polarization-sensitive optical coherence tomography," *Investigative Ophthalmology & Visual Science* 45, 2606-2612 (2004).
18. F.W. Campbell, and D.G. Green, "Optical and Retinal Factors Affecting Visual Resolution," *Journal of Physiology-London* 181, 576-593 (1965).
19. N.V. Ifimia, B.E. Bouma, J.F. de Boer, B.H. Park, B. Cense, and G.J. Tearney, "Adaptive ranging for optical coherence tomography," *Optics Express* 12, 4025-4034 (2004).

3. Polarization-Sensitive Optical Coherence Tomography

*Abstract**

Polarization-sensitive optical coherence tomography (PS-OCT) is a technology that uses polarized light to measure the depth-resolved birefringence of tissue. A fiber-based system was built and measurements were performed on healthy volunteers as well as glaucoma patients. The peripapillary area (the area around the optic nerve head) is most sensitive to changes induced by glaucoma. Concentric scans with increasing diameters up to 2.6 mm were made around the optic nerve head. The measurement time for each scan was 6 seconds, and eyes were dilated prior to an imaging session. Birefringence of healthy retinal nerve fiber layer was shown to be constant as a function of scan radius but varying as a function of position around the optic nerve head, with higher values occurring superior and inferior to the optic nerve head. Measured double pass phase retardation per unit depth around the optic nerve head of two healthy subjects varied between 0.10 and 0.35 °/ μm . These values are equivalent to birefringence values of 1.2×10^{-4} and 4.1×10^{-4} , measured at a wavelength of 840 nm. Measurements of glaucomatous retinas demonstrated nerve fiber layer thinning due to glaucoma. The time-domain PS-OCT measurements of glaucomatous retinal nerve fiber layer were not sensitive enough to measure birefringence reliably.

* This chapter is based on three articles that were previously published in peer-reviewed journals:

B. Cense, T.C. Chen, B.H. Park, M.C. Pierce and J.F. de Boer, "In vivo depth-resolved birefringence measurements of the human retinal nerve fiber layer by polarization-sensitive optical coherence tomography," *Optics Letters*, 27, 1610-1612 (2002).

B. Cense, T.C. Chen, B.H. Park, M.C. Pierce and J.F. de Boer, "In vivo birefringence and thickness measurements of the human retinal nerve fiber layer using polarization-sensitive optical coherence tomography," *Journal of Biomedical Optics*, 9, 121-125 (2004).

B. Cense, T.C. Chen, B.H. Park, M.C. Pierce and J.F. de Boer, "Thickness and birefringence of healthy retinal nerve fiber layer tissue measured with polarization-sensitive optical coherence tomography," *Investigative Ophthalmology & Visual Science*, 45, 2606-2612 (2004).

3.1 Introduction

Glaucoma is the world's second leading cause of blindness. The disease causes damage to the retinal ganglion cells, resulting in thinning of the retinal nerve fiber layer (RNFL). In addition, nerve fiber layer tissue loss may be preceded by changes in birefringence. As ganglion cells die and axons in the RNFL are replaced by a less organized and amorphous tissue composed of glial cells,¹ birefringence changes should be expected to occur. When glaucoma is detected at an early stage, further loss of vision can be prevented by treatment. The visual field test is the current standard method of detecting loss of peripheral vision in glaucoma. However, measurements show that up to 40% of nerves are irreversibly damaged before loss of peripheral vision can be clinically detected.¹

New instruments have been introduced that determine RNFL thinning. For example, optical coherence tomography (OCT) can produce structural cross-sections of the human retina and RNFL.² Variations in optical scattering and absorption allow differentiation between the cell layers of the retina. In scanning laser polarimetry (SLP), the retina in and around the optic nerve head (ONH) is probed with polarized light to detect RNFL phase retardation, which is converted to RNFL thickness.^{3,4} The RNFL is slightly birefringent because of its ordered structure,⁵ but birefringence is absent in layers that are located below the RNFL, including the ganglion cell layer. Birefringent elements in the eye, such as the cornea, the RNFL and Henle's fiber layer in the fovea, change the polarization state of the incident light. The polarization state of light that is reflected from all retinal structures and that has double-passed the RNFL is compared with the input polarization state. Assuming that RNFL birefringence is constant as a function of location and is constant between subjects, RNFL thickness can be calculated from the measured change in the polarization state or the phase retardation of the reflected light.

Polarization-sensitive optical coherence tomography (PS-OCT) combines the depth resolution of OCT with the polarization sensitivity of SLP to image the depth-resolved optical birefringence of biological tissue.⁶⁻⁹ We hypothesize that glaucomatous loss of nerve fiber tissue may be preceded by a change in birefringence, since it is suspected that disintegration of the nerve fiber mesh leads to a change of RNFL birefringence. Such a change in birefringence compared with normal levels could be an early sign of glaucomatous atrophy of the RNFL. Experiments - for instance, a longitudinal study with PS-OCT on patients at high-risk for development of glaucoma - will either confirm or reject this hypothesis. In addition, PS-OCT may enhance specificity in determining RNFL thickness in structural OCT images by using changes in tissue birefringence to determine the border between the RNFL and ganglion cell layer.

The author performed the first *in vivo* human retinal polarization-sensitive optical coherence tomography measurements in the superior area near the optic nerve head of a 38-year-old healthy volunteer.¹⁰ The mean double-pass phase retardation per unit depth (DPPR/UD) of the human retinal nerve fiber layer was equal to 0.39 ± 0.06 $^{\circ}/\mu\text{m}$. These measurements were performed without co-registration of retinal scan locations with a CCD camera. Using a modified setup equipped with a CCD camera and a broadband source with larger output power, more measurements were performed on the same volunteer.¹¹ Measured retinal nerve fiber layer DPPR/UD values around the optic nerve head varied between 0.18 and 0.37 $^{\circ}/\mu\text{m}$. Recently, extensive measurements with the same broadband source, but with an optimized measurement method were performed on the eyes of two young healthy volunteers.¹²

In this chapter, the most recent measurement method and results from two young healthy volunteers will be described in detail. Additional measurements on three other young healthy volunteers and preliminary measurements on two glaucoma patients will be discussed as well.

3.2 Polarization-sensitive OCT theory

The goal of a polarization-sensitive OCT measurement is to extract depth-resolved birefringence data. The phase retardation (δ) between orthogonal polarization components and birefringence (Δn) are related to each other by:

$$\delta = \frac{2\pi \cdot \Delta n \cdot x}{\lambda} \tag{Eq. 3}$$

with x equal to the distance traveled through the birefringent medium at a wavelength λ .

The microtubules and membranes of the axons of the ganglion cells in the retinal nerve fiber layer are the only birefringent elements in the human retina.^{5, 13} According to Eq. 3, the birefringence of a medium such as the retinal nerve fiber layer can be measured by measuring the thickness (x) and phase retardation (δ) separately at a known wavelength. Recently, the retinal nerve fiber layer birefringence of 26 volunteers was determined by measuring RNFL thickness by OCT and phase retardation by scanning laser polarimetry (GDx VCC).¹⁴ Assuming a constant birefringence value in Eq. 3, the GDx VCC itself calculates retinal nerve fiber layer thickness based on the measured phase retardation. Before we continue on this topic and explain why the GDx thickness measurement is incorrect, we first will introduce polarization-sensitive OCT.

With polarization-sensitive OCT, the depth resolved birefringence is determined directly with a single system by measuring the Stokes parameters of backscattered light as a function of depth.⁶ The Stokes parameters describe the polarization state of the

light and by analyzing Stokes vectors as a function of depth, the depth-resolved phase retardation of a sample can be determined.

First, we will elaborate a little more on Stokes vectors and the Poincaré sphere. The Stokes vector contains four parameters: I , Q , U and V . The *irradiance* is described by the I Stokes parameter. Only when the degree of polarization is 1, then $I^2 = Q^2 + U^2 + V^2$. The parameters Q , U and V are normalized to the irradiance I . The Q Stokes parameter describes how well the light is polarized along the horizontal axis ($Q = +1$) or vertical axis ($Q = -1$). The U parameter describes the amount of light polarized along the $+45^\circ$ ($U = +1$) or -45° ($U = -1$) axis and similarly the V parameter describes if the light is circularly right ($V = +1$) or left ($V = -1$) polarized. The Poincaré sphere has three axes (one for each Stokes component) that are perpendicular to each other. A Stokes vector is built from these three components and a vector points from the center of the sphere to a certain location on the surface of the sphere.

In an OCT setup, Stokes vectors can be measured by using a polarization-sensitive detector in the detection arm, which consists of two detectors set up around a polarizing beam splitter or prism. The two detectors detect horizontal and vertical electric field components that were separated by the polarizing beam splitter. A collimated quasi-monochromatic light beam propagating in the z direction with a frequency ω can be defined by two electrical field components, along the x (horizontal) and y (vertical) axis:

$$\begin{aligned} E_x &= A_1 \cdot e^{i(\theta_1(t) + \omega t)} \\ E_y &= A_2 \cdot e^{i(\theta_2(t) + \omega t)} \end{aligned} \tag{Eq. 4}$$

The Stokes parameters can be determined from the electric fields by:¹⁵

$$\begin{aligned} I &= \langle E_x E_x^* \rangle + \langle E_y E_y^* \rangle, \\ Q &= \langle E_x E_x^* \rangle - \langle E_y E_y^* \rangle, \\ U &= \langle E_x E_y^* \rangle + \langle E_x^* E_y \rangle, \\ V &= i \left[\langle E_x E_y^* \rangle - \langle E_x^* E_y \rangle \right] \end{aligned} \tag{Eq. 5}$$

where the asterisk denotes the complex conjugate and the $\langle \rangle$ brackets indicate time averaging.

In earlier free-space PS-OCT systems, the tissue was usually probed with circularly polarized light.^{6, 7, 16} A circularly polarized incident state is preferred, since it will always interact with birefringent tissue that has an optic axis in a plane perpendicular to the propagation direction of the beam. For instance, a linear polarization state that is aligned with the optic axis of the material will not experience

any phase retardation since no component is aligned with the slow axis. Only when two orthogonal polarization components resolved along the fast and slow axis of the material are present simultaneously, one component can be delayed with respect to the other, because it experiences a different index of refraction. In free-space PS-OCT systems, the polarization state of reflected light is compared with the incident circular state in order to determine the depth-resolved phase retardation. Compared to open-air systems, it is easier to construct a human eye measurement interface with fiber-based PS-OCT systems. However, in a fiber-based PS-OCT system, it is difficult to maintain a circular polarization state at the sample surface, since stress in the fibers and a noncircular shape of the fiber core will change the polarization state of the light traveling through the fiber. In previous fiber-based PS-OCT systems, this problem was overcome by using a relative measurement method in which the tissue was probed with first four^{8,9} and later two different polarization states.¹⁷

In the retinal nerve fiber layer studies presented in this thesis, two incident polarization states - perpendicular in a Poincaré sphere representation - were used.¹⁰⁻¹² An example of a combination of two polarization states that obey this requirement are linearly and circularly polarized light. Since both states travel through the same medium, they will experience the same birefringence. Diattenuation (polarization dependent loss) is assumed to be negligible in single mode fibers and in the sample tissue. Circular birefringence is present in optical fibers, but cannot be measured in our system since it cancels out in forth and back propagation. Circular birefringence can therefore not be measured in reflection in a sample. Variations in temperature and fiber stress are not expected in the time span between two A-lines. While traveling through birefringent media, the two polarization states change, but their Stokes vectors will always remain perpendicular within a Poincaré sphere representation.⁹ In the absence of diattenuation, the latter condition ensures that at least one of the polarization states incident on the retina will experience phase retardation due to the birefringent tissue.

3.3 Measurement method

3.3.1 Experimental Setup

The two polarization states, 90° apart on the Poincaré sphere, were generated by means of a piezo-driven polarization modulator in the source arm. A high-power superluminescent diode (Superlum, Russia) generated a broadband spectrum with a power of 4.6 mW (after polarization by the isolator) and with a full width at half maximum (FWHM) bandwidth of 50 nm centered at 839 nm . The coherence function was measured using a mirror in water ($n = 1.33$), giving an FWHM coherence length of $5.9 \text{ }\mu\text{m}$ (Chapter 2). In the retina, the axial resolution becomes $5.7 \text{ }\mu\text{m}$, assuming an index of refraction of 1.38. As shown in Figure 10, a fiber coupler divided the light

between sample and reference arms. The fiber coupler ratio in the interferometer was chosen as 80/20, since the power that could be sent continuously into the eye had to be below the ANSI standard limit of $610 \mu W$.¹⁸

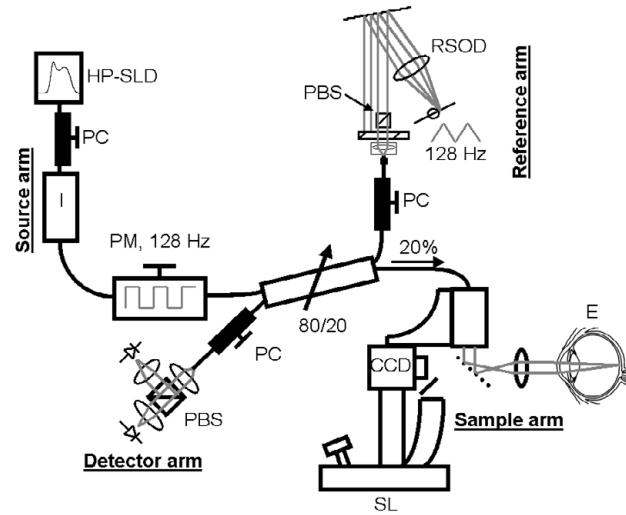


Figure 10. Schematic overview of the fiber-based PS-OCT setup. Near-infrared light from a high-power superluminescent diode (HP-SLD) was sent through an isolator (I), after which its polarized state was modulated (PM) and split by means of a 80/20 fiber coupler. Eighty percent of the light was sent into the rapid scanning optical delay line (RSOD), where a polarizer (PBS) ensured that light was always in the same linear state, regardless of changes in the polarization state in the fiber before the RSOD. Twenty percent of the power was directed toward the slit lamp (SL) in the sample arm. Light reflected back from the sample arm and delay line interfered in the detection arm and was split by a polarizing beamsplitter (PBS), after which both orthogonal states were detected by means of two silicon detectors.

The sample arm consisted of a telecentric XY retinal scanner and a headrest from a standard slit lamp, with the sample beam pivoting about the center of the entrance pupil of the eye (described in Chapter 2). The incident power on the eye was $495 \pm 5 \mu W$, which is well below the maximum level specified in the ANSI standards. The eye under investigation could be stabilized with a fixation spot, as described in Chapter 2.

A charge-coupled device (CCD) camera was available for visual inspection of the retina and localization of PS-OCT scans in the retina. During a PS-OCT B-scan 48 CCD images were acquired and stored on a hard disk. While 20% of the power was sent to the sample, the remaining 80% was directed toward the reference arm, which consisted of a rapid scanning optical delay line (RSOD).¹⁹ A polarizing beamsplitter was used as a polarizer in order to ensure that the light in the RSOD was always in the same linear state, regardless of changes in the polarization state in the fiber before the

RSOD. A polarization controller placed before the RSOD was aligned so that the power reflected from the RSOD was constant for both input polarization states. Dispersion in sample and reference arms was matched by adjusting the grating to lens distance in the delay line.¹⁸ The delay line's scanning mirror was positioned off-axis and driven by a triangular waveform with a frequency of 128 Hz synchronized with the polarization modulator, which was driven by a block wave at the same frequency. The carrier signal was approximately 330 kHz and signals were digitally bandpass filtered with a bandwidth of 80 kHz centered at the carrier frequency. Owing to the enhanced splitter ratio, 80% of the returned light from the sample arm went to the detection arm, while 20% of the light returning from the RSOD reached the detectors. The detection arm consisted of a polarization controller and a polarizing beamsplitter that split the light into two orthogonal components before detection by two silicon detectors.

Signal detection was shot-noise-limited. The two signals were digitized with a 12-bit 2.5-MHz analog to digital (A/D) board and immediately stored on a hard disk. During each circular B-scan of 6 seconds duration, 1536 A-lines over a depth of 1 mm were acquired. Each A-line consisted of 8192 samples. In real time, both intensity and phase retardation B-scans were displayed.²⁰ The former allowed us to detect the position of the retina in real time. A correction signal was calculated and added to the driving waveform of the RSOD galvanometer, compensating for small shifts of up to approximately 1 mm due to the volunteer's movement in the direction of depth scanning.²¹

3.3.2 System accuracy measurement

The accuracy of the phase retardation measurement was determined by measuring a calibrated mica wave plate with 58.6° single-pass retardance. Since the setup was designed to measure samples in a human eye through the cornea and lens, the setup had to be adapted for this calibration. An image of the wave plate was created in the image plane (see Figure 10) by shifting the ophthalmic lens and increasing the scan length of the delay line to approximately 3 mm . The wave plate was slightly tilted so that a small amount of light was reflected back into the PS-OCT system. Data were taken at two different optic axis orientations of the wave plate that were 90° apart.

3.3.3 Data analysis

By processing the acquired interference fringe data as described in section 3.2 the 8192 samples within one A-line were converted to 1024 Stokes parameters I , Q , U , and V .⁷⁻⁹ For these measurements, the surface Stokes vector was calculated $5 \mu\text{m}$ below the surface edge, which was determined from the I Stokes parameter by a threshold function preceded by a 5×5 median filter. We compared Stokes vectors at the RNFL's surface with Stokes vectors at lower depths to determine the double-pass

phase retardation (DPPR) and optic axis orientation.⁷⁻⁹ For the RNFL thickness analysis, structural intensity OCT images were corrected for axial motion artifacts, according to a method described by Swanson *et al.*²² PS-OCT structural intensity images were gray-scale encoded on a logarithmic scale, with white pixels representing low reflectivity and a black pixel indicating high reflectivity (see Figure 12). To reduce the influence of speckle noise (grainy noise caused by interference of coherent light), a moving-average filter with a length of $\sim 10 \mu\text{m}$ was applied in the axial direction.

The image of a circular scan was projected as a B-scan and divided into 48 sectors of 32 A-lines, each covering 7.5° of the circular scan starting temporal to the optic nerve head (ONH) and analyzed with a custom made program written in commercial software (Visual C++; Microsoft Corp., Redmond, WA).^{9, 10}

The data sets of the first two healthy volunteers were analyzed in detail by the author. Using analysis criteria set up by the author, all other data sets were analyzed by a student.

3.3.4 Volunteer inclusion and exclusion criteria

All experiments were performed under a protocol that adhered to the tenets of the Declaration of Helsinki and was approved by the Institutional Review Boards of both the Massachusetts Eye and Ear Infirmary and Massachusetts General Hospital. For this study, six healthy volunteers and five patients with different stages of glaucoma were enrolled.

Healthy volunteers

After giving informed consent, subjects underwent a complete ophthalmic examination at the Massachusetts Eye and Ear Infirmary (Boston, MA). This examination included a detailed medical history, visual acuity testing, intraocular pressure (IOP) measurement, and slit lamp examination. Eyes were dilated with phenylephrine hydrochloride 5.0% and tropicamide 0.8% for a complete retinal examination. Only normal eyes with refractive errors between +5.00 and -5.00 diopters (D) were included. Subjects were excluded if they had a history of intraocular surgery or laser therapy or had any evidence of retinal disease or glaucoma. Subjects were also excluded if they had occludable angles or any other disease state that would preclude safe pharmacologic pupil dilation. One healthy volunteer was excluded from the study because of evidence of possible early glaucoma. Five healthy volunteers were accepted. After pupil dilation they were measured with PS-OCT. Data sets were analyzed to determine the accuracy of the system and to map RNFL thickness and DPPR/UD.

Glaucoma patients

Patients with various stages of open angle glaucoma (primary, pigmentary, and pseudoexfoliation forms) were recruited from the glaucoma practice of Teresa Chen, M.D. at the Massachusetts Eye and Ear Infirmary. Medical records were used to determine if patients were eligible for the study. Patients underwent ophthalmic examinations similar to the healthy volunteers, but eyes were not subject to any refractive limitations. Four out of five glaucoma patients were imaged with PS-OCT, and two data sets from the two patients with the highest image quality were analyzed.

3.4 Results

3.4.1 Wave plate measurement

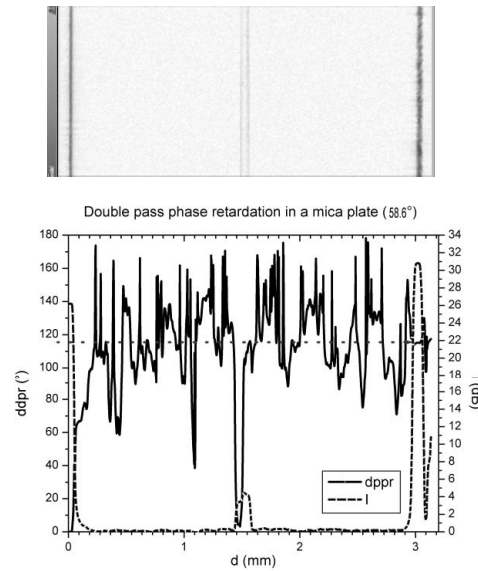


Figure 11: Structural intensity image (top) obtained with PS-OCT from a mica wave plate. The mica retarder was approximately $50 \mu\text{m}$ thick and glued between two glass plates. The image is rotated by 90° to match the graph (bottom). The graph shows the DPPR and intensity as a function of depth. The black line represents the DPPR, and touches the dotted red line at depths of approximately 1.45 mm and 3 mm . At these locations, the DPPR is equal to approximately 118° . The wave plate was measured by the manufacturer at 830 nm , yielding a phase retardation of 58.6° (single-pass). A color image can be found on page 121.

The top image shows a structural intensity image of the wave plate, consisting of a thin mica slab glued between two thicker glass plates. The mica retarder was approximately $50 \mu\text{m}$ thick. The image was rotated by 90° so that it could be

compared with the intensity and phase retardation measurements (bottom plot). The phase retardation was determined by comparing Stokes parameters at the front surface ($d = 0 \text{ mm}$) with those at the back of the retarder, since these two locations had the strongest reflections. Other possibilities were using the front surface of the mica retarder (around $d = \sim 1.5 \text{ mm}$) and the back of the retarder or the last glass to air surface (around $d = \sim 3.0 \text{ mm}$). However, the intensity at the first glass to mica interface was not as high as the first air to glass interface, making this surface a less reliable candidate than the front surface.

The phase retardation graph is noisy, with large variations around a mean value of approximately 120° . This noisy behavior is caused by a very low signal returning from positions within the glass and mica plates, and is therefore not reliable. The signal is only reliable at the interface between two slabs. To decrease the influence of speckle noise, results were averaged over 12 measurements, and divided by a factor of two to determine the single-pass phase retardation. The mean single-pass phase retardation was equal to $58.5^\circ \pm 1.5^\circ$, independent of the orientation of the optic axis of the wave plate. We concluded that the system was accurate within 3%. This number represented the accuracy of the system.

In our *in vivo* results, obtained from the retina of healthy volunteers, we determined the standard error in the data caused by a combination of speckle noise, biological variation in the sample, and accuracy of the system by making repeated measurements on a single eye.

3.4.2 Detailed measurements in two healthy volunteers

Best corrected visual acuity was 20/20 in both healthy volunteers. Both subjects had intraocular pressure less than 21 *mm* Hg, a normal- appearing ONH, and normal confrontational visual fields. Volunteer 1 was a 25-year-old white female (left eye) and volunteer 2 was a 39-year-old white male (right eye).

PS-OCT Intensity Images

Figure 12 is a typical example of a structural-intensity OCT image of the retina in the left eye of volunteer 1, obtained with a circular scan of radius 2.1 *mm* around the ONH. The image measures 13.3 *mm* in width and is 0.9 *mm* deep, and is shown at an expanded aspect ratio in depth for clarity.

The dynamic range within the intensity image was approximately 36 *dB*. For this particular image, speckle noise was removed in each A-line with a moving average filter with a length of $\sim 7 \mu\text{m}$ in the axial direction. On the left (Figure 12), the scan starts temporal to the ONH. Structural layers such as the RNFL, the interface between the inner and outer segments of the photoreceptors, and the RPE can be seen.²³

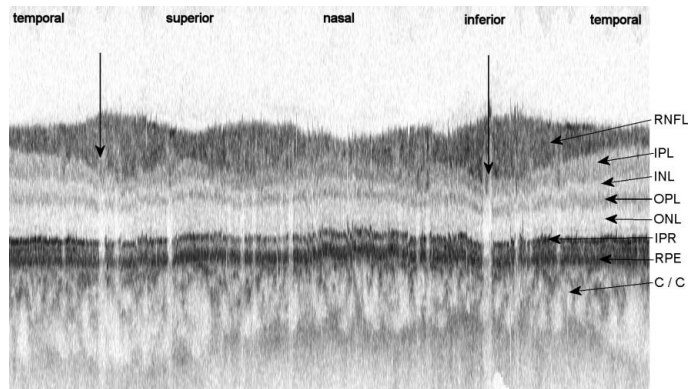


Figure 12. A realigned OCT intensity image created with a 2.1-mm radius circular scan around the ONH. The image was realigned based on the first moment (mean) of the intensity. Since the interface between the inner and outer segments of the photoreceptor layer (IPR) and retinal pigmented epithelium (RPE) are the darkest elements in the image, the image is realigned on those structures. The dynamic range of the image is ~ 36 dB. Black pixels represent strong reflections. The image measures 13.3 mm wide and 0.9 mm deep. Visible structures: retinal nerve fiber layer (RNFL); inner plexiform layer (IPL); inner nuclear layer (INL); outer plexiform layer (OPL); outer nuclear layer (ONL); interface between the inner and outer segments of the photoreceptor layer (IPR); retinal pigmented epithelium (RPE); and choriocapillaris and choroid (C/C). Vertical arrows: locations of the two largest blood vessels. Other smaller blood vessels appear as vertical white areas in the image.

Example of combined thickness and phase retardation measurements

In Figure 13, two examples of a combined thickness and DPPR measurement are given, one of a sector temporal to the ONH (A), the other of a sector superior to the ONH (B). In these plots, the intensity and double-pass phase retardation averaged over all A-lines within a sector are plotted as a function of depth. A least-squares fit through data points considered to belong to the RNFL is used to calculate the DPPR/UD of the RNFL. The RNFL thickness can be determined in two ways. First, a decrease in intensity is a sign of the lesser light-scattering ganglion cell layer and inner plexiform layer deep to the highly light-scattering RNFL tissue. Second, a transition from linearly increasing double-pass phase retardation to a constant level indicates a change from birefringent tissue to tissue without birefringence. The combination of these two methods helps in accurately determining the RNFL boundary. For noisy time-domain measurements, the average DPPR value below the RNFL was used to calculate the DPPR/UD. The average DPPR value would be divided by the thickness of the RNFL to calculate the DPPR/UD.

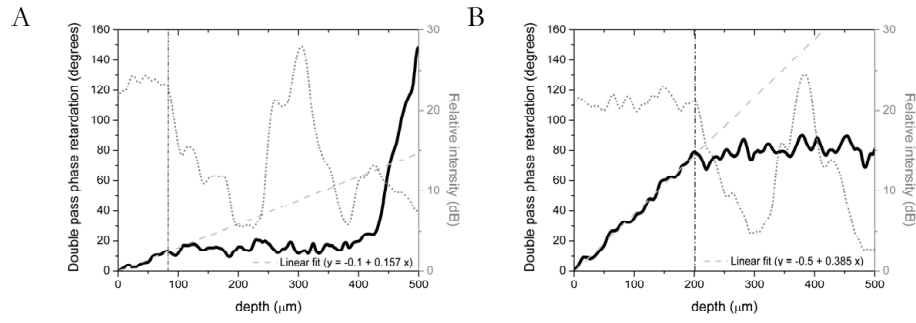


Figure 13. Thickness (dotted line) and DPPR (solid line) plots of an area temporal (A) and superior (B) to the ONH. DPPR data corresponding to the RNFL is fit with a least-squares linear fit. The slope in the equation represents the DPPR/UD. The vertical line indicates the boundary of the RNFL, as determined from the intensity and DPPR data. In (A), the increase in DPPR at a depth beyond 450 μm is caused by either a relatively low signal-to-noise ratio, or by the presence of a highly birefringent material - for instance, collagen in the sclera.

Figure 13 also demonstrates that the RNFL was birefringent, and the retinal layers below the RNFL were not. The DPPR/UD was solely determined from the slope of the linear fit through RNFL data points in the double-pass phase retardation plot, which makes this method less dependent on an accurate thickness measurement.^{10, 11}

The measurements displayed in Figure 13 were based on the Stokes vector analysis. Using a Poincaré sphere representation, we can determine whether the observed retardation is truly the result of birefringence. To determine the DPPR of the RNFL we compared Stokes vectors at the RNFL's surface with Stokes vectors at lower depths to determine DPPR and optic axis orientation.⁷⁻⁹ Figure 14 shows the evolution of the two incident Stokes states over the surface of the Poincaré sphere with increasing depth of tissue for a region of 32 A-lines temporal (A) and superior (B) to the optic nerve head. The rotation of both states over an arc about a single axis explicitly demonstrates birefringence with a single optic axis, as expected for the regularly oriented fibers in the RNFL. The angle of rotation, starting at the places marked X, corresponds to accumulated DPPR as a function of depth. The angle between two equidistant Stokes vectors was approximately 90°.

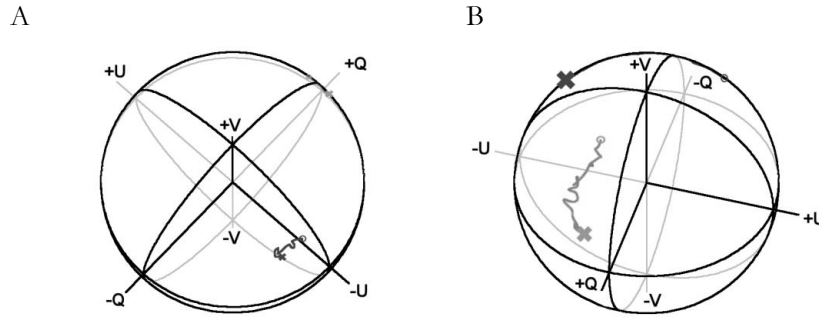


Figure 14. Evolution of the Stokes vectors with depth, from data averaged over 32 A-lines. The Poincaré sphere is oriented such that the axis of rotation is pointing out of the plane of the drawing. The two thick lines show the change in Stokes vectors over a distance of 85 μm in the RNFL (A), and 200 μm in the RNFL (B) and X's indicate the surface Stokes states. Circles indicate the Stokes state that is deepest in the tissue. The DPPR is derived from the angle of rotation about the optic axis, starting with the Stokes vector that belongs to the surface and finishing with the vector that belongs to a certain depth. A color image can be found on page 121.

With our PS-OCT system, thickness and DPPR/UD can be measured simultaneously and quantitatively. Figure 15 is a typical example of a combined thickness and DPPR/UD measurement obtained from volunteer 1, with the OCT structural intensity image plotted in the background. RNFL thicknesses and DPPR/UD values are displayed as a function of sector of 32 A-lines. The thickness plot indicates that the thickest RNFL was located superiorly and inferiorly. For the DPPR/UD plot, a similar pattern was seen. The DPPR/UD was relatively high superiorly and inferior and lower temporally and nasally.

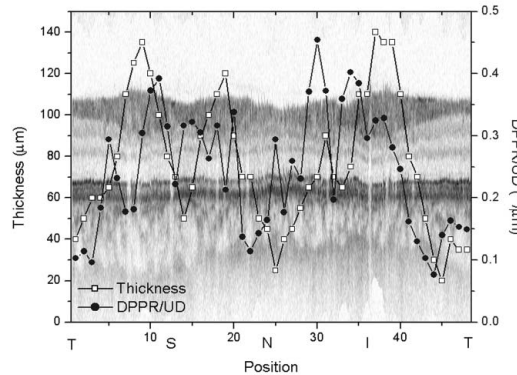


Figure 15. A typical example of combined RNFL thickness and phase retardation measurements along a circular scan around the ONH. The intensity image is plotted in the background. The RNFL is relatively thick superior (S) and inferior (I) to the optic nerve head. A similar development can be seen in the phase retardation plot. The phase retardation is relatively higher in the thick areas, whereas it is lower in the thinner temporal (T) and nasal (N) areas.

Overview of thickness and retardation measurements around the ONH

Although 12 circular scans were made in each eye, only scans outside the ONH were analyzed. In general, this means that the inner two circular scans that lay inside the ONH were not analyzed.

Thickness

In Figure 16A, RNFL thickness is plotted as a function of sector and scan radius around the ONH of the left eye of volunteer 1.

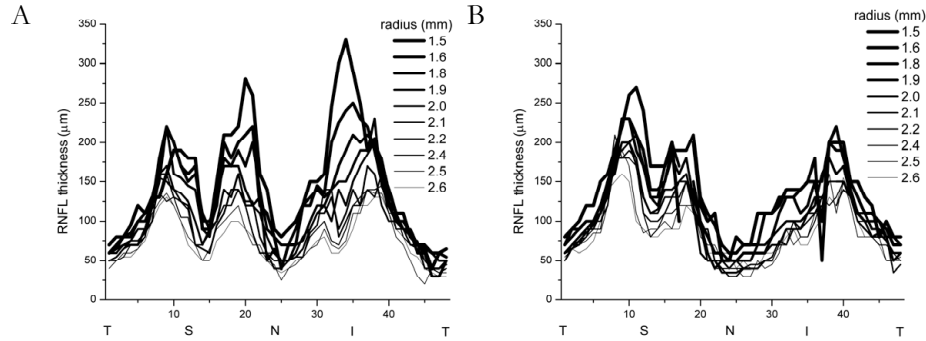


Figure 16. RNFL thickness as a function of relative position to and distance from the ONH. (A) Left eye of volunteer 1; (B) right eye of volunteer 2. RNFL thicknesses are given as a function of position (x-axis) and scan radius (line style). Positions are relative to the ONH. T, temporal; S, superior; N, nasal; I, inferior.

The smallest scan had a radius on the retina of 1.5 *mm*, whereas the largest scan had a radius of 2.6 *mm*. The different plots demonstrate that an increased distance from the ONH was associated with a thinner RNFL. The thickness variation pattern with higher thicknesses inferior and superior was largely constant as a function of radius. This consistent RNFL thickness pattern can be explained by the fact that most nerves from the retina and fovea enter the ONH inferiorly and superiorly.²⁴ The data set of volunteer 2 (Figure 16B) showed characteristics similar to those of the data set of volunteer 1. One major difference is that the RNFL was thickest superior to the ONH of this volunteer.

Using the data sets obtained from volunteer 2, we estimated the standard error on the RNFL thickness measurement from three scans ($n = 3$) with equal radii of 1.8 *mm*. Two of those scans were made on one day, while the third one was made a few days later. All three scans were centered similarly on the ONH. Each scan was divided into 48 sectors of equal length. The mean thickness and standard error were calculated for

each sector. Involuntary retinal movements created a larger error within sectors in which the thickness varied significantly, compared with sectors with a more uniform thickness. The average standard error of sectors where the RNFL thickness did not change significantly was estimated to be $\pm 5 \mu\text{m}$, but in sectors where the change of thickness was high (e.g., sectors 22 and 32 in Figure 16A), it was estimated to be $\pm 10 \mu\text{m}$. These errors may vary depending on the amount of eye movement.

Double-pass phase retardation per unit depth

The same data sets of volunteers 1 and 2 that were used for the thickness mapping in Figure 16 were analyzed for DPPR/UD information. All measurements per sector of 10 circular scans with increasing radius were plotted as a function of sector. In Figure 17A and Figure 17C (with Figure 17A containing data of volunteer 1 and Figure 17C containing the data of volunteer 2) each of 48 measurements at a certain radius is labeled with the same symbol. Although we did not prove yet that averaging is permitted (averaging over sectors from different radii yields incorrect values when there is a trend as a function of radius), the mean value per sector and its standard error were plotted and neighboring means were connected with a line. The standard error can be found by dividing the standard deviation by the square root of the number of measurements per sector. In this case, with measurements at 10 radii, it is equal to the square root of 10.

To demonstrate whether averaging is permitted, data sets obtained at different radii were compared with each other. The data in Figure 17 (A, C) were low-pass filtered with a fast Fourier transform (FFT)-based filter that retained the lowest nine Fourier components. The processed data sets of volunteers 1 and 2 are displayed in Figure 17B and Figure 17D. Thick lines represent filtered data of circular scans closer to the ONH and scans farther away are marked with thinner lines. The processed data set of volunteer 1 indicate an increase of DPPR/UD with radius in the RNFL bundles superiorly and inferiorly around sectors 16 and 36, although a similar trend was not found inferiorly around sector 32. In the data set of volunteer 2, a similar trend was found in the RNFL bundle superiorly. These trends indicate that the means, as displayed in Figure 17A and Figure 17C, do not represent the scans close and far away from the ONH. No trend was observed in the other sectors, which permitted the averaging over sectors. For both subjects, the DPPR/UD pattern is similar to the thickness pattern. At all scan radii, DPPR/UDs were relatively high in superior and inferior areas. In volunteer 1, the highest DPPR/UD occurred superiorly and was $0.35 \pm 0.03 \text{ } ^\circ/\mu\text{m}$. Volunteer 2's highest DPPR/UD of $0.37 \pm 0.04 \text{ } ^\circ/\mu\text{m}$ occurred inferiorly. Both volunteers exhibited low mean measurements in the temporal area: $0.10 \pm 0.03 \text{ } ^\circ/\mu\text{m}$ (volunteer 1) and $0.11 \pm 0.05 \text{ } ^\circ/\mu\text{m}$ (volunteer 2). For volunteer 1, the difference between the highest and lowest DPPR/UD is equal to 8 SEs, indicating

that the observed difference is statistically significant. The same trend holds for the difference observed in volunteer 2's data, which were more than 5 to 7 SEs apart.

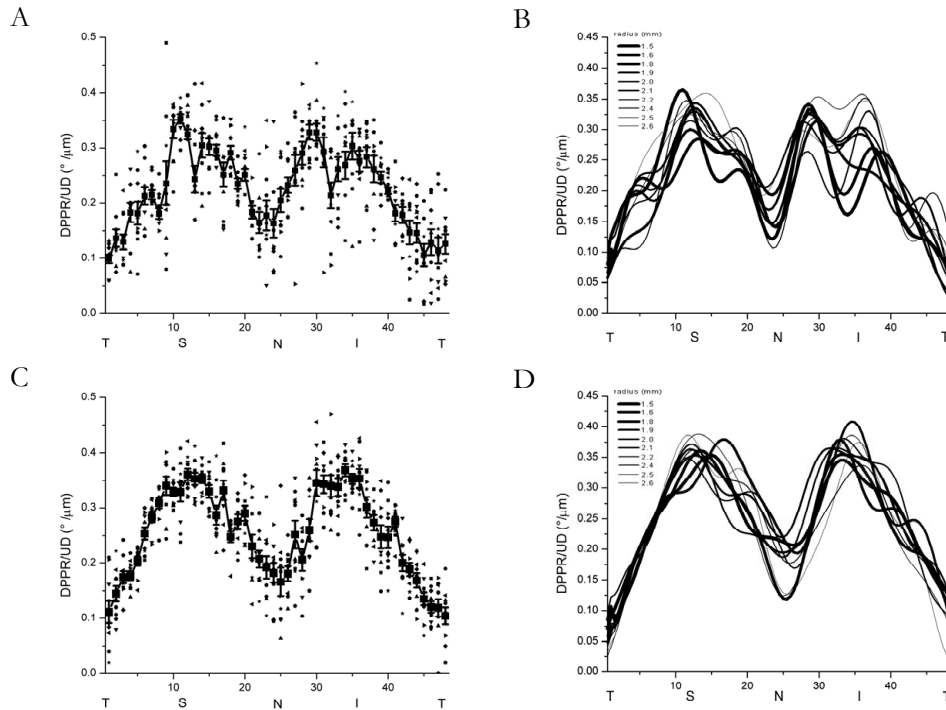


Figure 17. (A, C) the RNFL DPPR/UD is plotted as a function of relative position with respect to the ONH. (A, B) Left eye of volunteer 1; (C, D) right eye of volunteer 2. DPPR/UD was measured in all 48 sectors of 10 scans with radii between 1.5 and 2.6 mm around the ONH. Results from sectors at a certain radius are marked with the same symbol. The mean DPPR/UD was marked with a larger symbol and connected with a line. Error bars, SE. (B, D) Same data after filtering with a low-pass FFT filter reveals possible trends in DPPR/UD as a function of radius and indicates whether averaging is permitted.

To determine the reliability of the DPPR/UD measurements, three scans repeated with the same radius of 1.8 mm were analyzed. All three scans were obtained in the same eye of volunteer 2 during one measurement session. Figure 18 shows the average RNFL thickness plot combined with a plot of the average DPPR/UD and standard error of the average DPPR/UD to demonstrate the dependence of the DPPR/UD standard error on RNFL thickness.

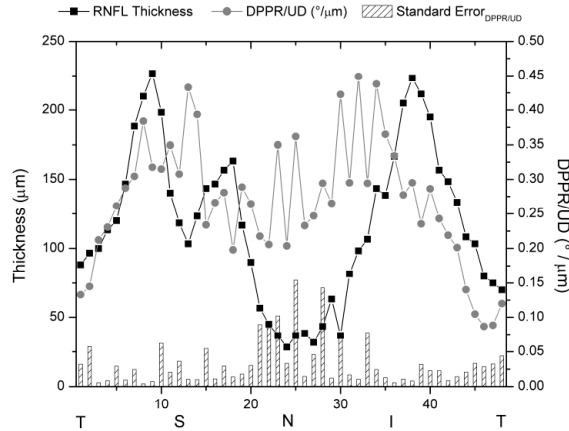


Figure 18. RNFL thickness, average DPPR/UD, and standard error of the DPPR/UD are plotted. In the nasal area, where the thickness was below $75 \mu m$, the DPPR/UD standard error increased, suggesting that DPPR/UD measurements made with the current setup are most reliable in thicker RNFL areas (S and I). Positions are relative to the ONH: T, temporal; S, superior; N, nasal; and I, inferior.

The average standard error in DPPR/UD is approximately $\pm 0.03 \text{ }^\circ/\mu m$, except for the thin nasal area, in sectors 20 to 30, where the thickness is below $75 \mu m$. In this area, the average standard error is estimated to be $\pm 0.10 \text{ }^\circ/\mu m$. The standard error was found by dividing the SD with the square root of the number of measurements, in this case the square root of 3. The standard errors of Figure 18 ($n = 3$) and ($n = 10$) yield similar standard deviations, since the standard deviation is equal to the standard error times square root of the sample size. With a sample size of 10 measurements instead of three, the standard error of Figure 18 is expected to approximate those of Figure 17. In areas with blood vessels, DPPR/UD values became less reliable because of attenuation of the signal by blood. If we had excluded all areas encompassing blood vessels, too many sectors would have been excluded. However, blood vessels became smaller and less visible in the intensity images that were taken farther away from the ONH. Some of them sank toward the layer below the RNFL. As a consequence, at a scan radius of 1.8 mm or more, DPPR/UD measurements were less influenced by the presence of blood vessels. Both volunteer 1 and 2 had lower DPPR/UDs ($\sim 0.10 \text{ }^\circ/\mu m$) temporal to the ONH, a value equivalent to a birefringence of 1.2×10^{-4} , measured at a wavelength of 840 nm . Compared with the birefringence of a well-known birefringent material such as collagen, this value is approximately 10 times lower.²⁵ Superior and inferior to the optic nerve head, higher DPPR/UDs of $\sim 0.35 \text{ }^\circ/\mu m$, equivalent to a birefringence of 4.1×10^{-4} were noted.

3.4.3 Measurements in other healthy volunteers

Best visual acuity was 20/20 in volunteers 3 and 5. Volunteer 4's best visual acuity after correction was 20/50, probably caused by anisometropic amblyopia ("lazy eye"). All three healthy subjects had intraocular pressures less than 21 *mm* Hg, normal-appearing ONH, and normal confrontational visual fields. Volunteer 3 (A, B) was a 30-year-old white male (left eye), volunteer 4 (C, D) was a 47-year-old black female (right eye) and volunteer 5 (E, F) was a 23 year old white male (left eye).

As can be seen in plots A, C and E, the thickness plots of these subjects are similar to the plots from volunteers 1 and 2. The RNFL thins with increasing distance from the optic nerve head, and has highest values superiorly and inferiorly to the optic nerve head. The irregularities in the nasal area of the thickness plot of Figure 19A are most likely caused by blood vessels. The CCD camera footage showed that volunteer 4 (C, D) blinked relatively often and did not fixate as well as the other healthy volunteers. This explains the missing data points with a scan radius of 1.5 and 1.6 *mm* around sector 40.

Regarding the phase retardation plots, Figure 19B and F develop similarly to the phase retardation plots displayed earlier in Figure 17. Highest DPPR/UD values occur superiorly and inferiorly to the optic nerve head, while lowest values are found in the temporal area. Figure 19D shows high values superiorly to the optic nerve head, while DPPR/UD values increase between the nasal and inferior area. The highest value that occurs in the inferior area is only slightly higher than the nasal values. Consistent with the other healthy volunteers, lowest values occur temporal to the optic nerve head.

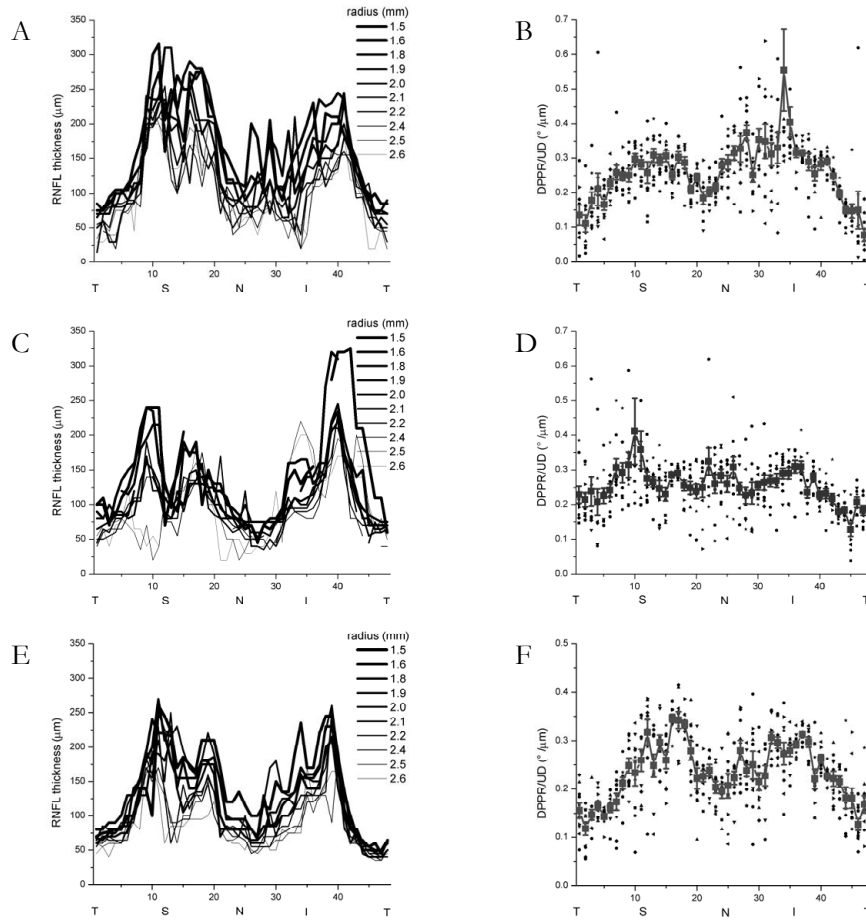


Figure 19. Thickness (A, C, E) graphs of volunteers 3, 4 and 5. DPPR (B, D, F) graphs of volunteers 3, 4 and 5. Comparing these thickness graphs with the thickness graphs from Figure 16, a similar thickness development can be observed. The RNFL thins with increased distance from the ONH. The thickness variation pattern with higher thicknesses inferior and superior was largely constant as a function of radius. Except for plot D (volunteer 4, the oldest volunteer in this study), the DPPR/UD plots are very similar to the plots of the first two volunteers as seen in Figure 17. Higher DPPR/UD values occur superiorly and inferiorly to the optic nerve head. The spikes in plot A are explained by blood vessels and the inexperience of the operator with the software. The y-axis of plot B was expanded in order to display all DPPR/UD values.

3.4.4 Results obtained from two glaucoma patients

The eyes of four glaucoma patients were imaged. Two of the data sets had a signal-to-noise ratio that was found to be good enough for analysis. The other two data sets were too noisy, most likely due to inefficient transmission of the OCT beam through the pupil and cornea. This can be explained as follows. First, some eyes that are affected by glaucoma do not dilate as well as healthy eyes and OCT imaging becomes more difficult through small pupils, as described in Chapter 2. For the measurements on these two patients, the slit lamp interface did not function properly, and imaging and illumination beams did not overlap. Furthermore, especially when the imaging beam does not exactly pivot through the pupil, or when the beam does not pass through the center of the pupil, clipping of the beam may occur, leading to a reduced image quality. Second, the transmission quality of the eye can be affected by the state of the cornea. Older eyes usually dry out faster than young eyes, especially when patients don't blink sufficiently. In this study, we asked patients to blink only if necessary, but this may have affected the quality of the tear film and therefore the optical quality of the cornea. The tear film may act as an index matching fluid, filling up irregularities that could cause major aberrations. Third, glaucoma patients tend to be older and these patients tend to have more cataracts, which can decrease image quality due to scattering and absorption.

Best-corrected visual acuity was 20/20 in both patients, each of whom had intraocular pressures below 21 *mm* Hg. The left eye of patient 1, a 55-year-old black male, was diagnosed with glaucoma in the mid 1990's and had been treated since 2002. The left eye of glaucoma patient 2, a 65-year-old white female, was diagnosed with glaucoma in 1987, and the glaucoma in the eye has been stable since then.

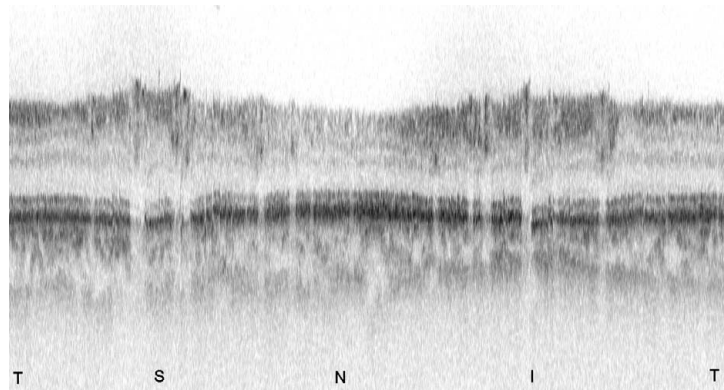


Figure 20. A realigned OCT intensity image created with a 1.9-*mm* radius circular scan around the ONH of glaucoma patient 1. The dynamic range of the image is ~ 34 *dB*. Black pixels represent strong reflections. The image measures 11.9 *mm* wide and 0.8 *mm* deep and is expanded in the vertical direction for clarity. Compared to the scans made in healthy volunteers, the RNFL is thinner, while the contrast between the RNFL and ganglion cell layer is lower.

Compared to the other glaucoma patients, patients 1 and 2 fixated well, and in addition, their pupils dilated well. Glaucoma patient 1 had severe glaucoma, resulting in a relatively thin nerve fiber layer (Figure 20). From the detailed measurements in healthy volunteer 2, it was concluded that the DPPR/UD analysis becomes unreliable when the RNFL thickness is smaller than $75 \mu\text{m}$. After analyzing the thickness in the first 6 scans closest to the optic nerve head (Figure 21A), which are supposed to be the thickest, we concluded that the DPPR/UD data was unreliable (Figure 21B). Furthermore, comparing the backscattering intensity from the RPE with the intensity returning from the RNFL, the glaucomatous RNFL does not seem to scatter as well as those of healthy volunteers in Figure 12. In addition to a thinner RNFL, the lower signal-to-noise ratio of the RNFL data decreases the reliability of the DPPR/UD measurements.

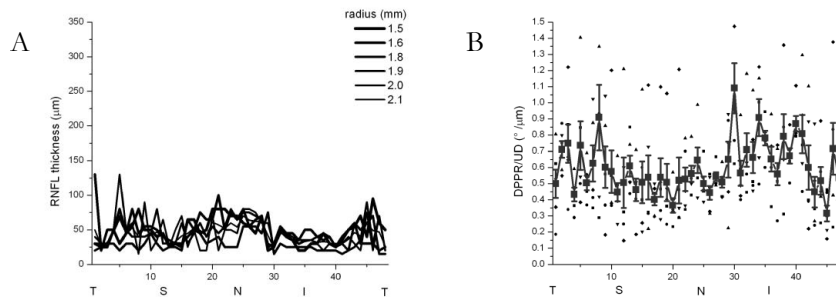


Figure 21. Thickness (A) and DPPR/UD (B) graph of glaucoma patient 1. Compared to the healthy volunteers, the RNFL thickness is low, with thickness values consistently below $75 \mu\text{m}$, making the DPPR/UD analysis (B) unreliable. The DPPR/UD values average around $0.6^\circ/\mu\text{m}$, which is approximately twice as high as the DPPR/UD values in healthy volunteers. The SE in this Figure was based on 6 measurements.

Glaucoma patient 2 was diagnosed with glaucoma 17 years ago. She had been on medication since then, regularly visiting the glaucoma clinic. As can be seen in Figure 22, her nerve fiber layer thickness was not affected as severely as patient 1's nerve fiber layer.

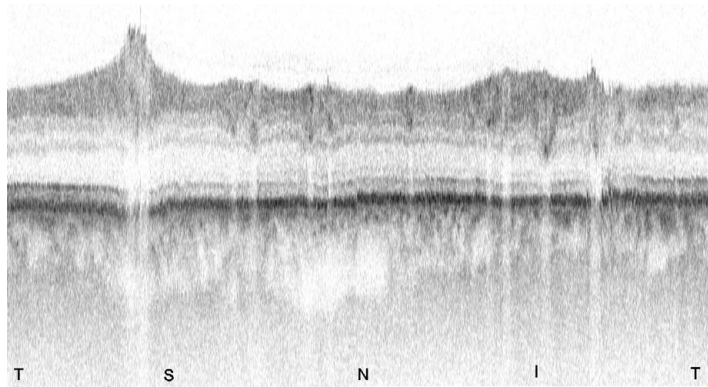


Figure 22. Realigned structural intensity image of glaucoma patient 2. The dynamic range within the image is 35 dB. The RNFL tissue is thickest around the blood vessels.

In Figure 23A where thickness and DPPR/UD are given as a function of sector and radius, it can be seen that the RNFL is thinnest temporal and nasal to the optic nerve head. In the structural intensity image, the tissue aggregates around thick blood vessels. The DPPR/UD results of Figure 23B are therefore questionable, even when the thickness values in certain sectors surpass the 75 μm limit. The values in these sectors vary between 0.2 and 0.3 $^{\circ}/\mu m$, which is relatively low for tissue located in the inferior and superior area.

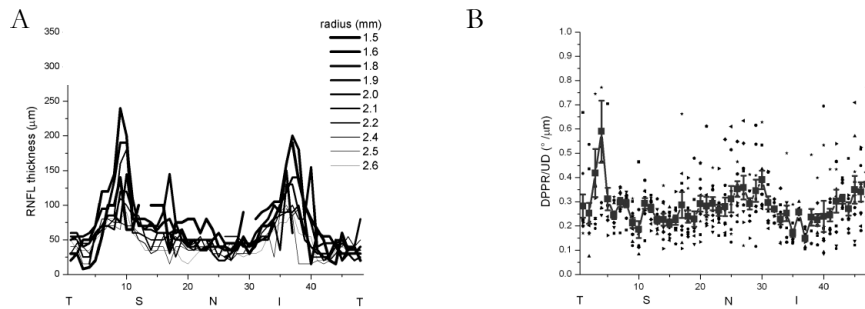


Figure 23. Thickness (A) and DPPR/UD (B) graph for glaucoma patient 2. Superior and inferior areas are still relatively thick, but with an overall thickness which is below that of a healthy subject. The DPPR/UD graph does not show the variation that can be seen in healthy subjects.

The main conclusion that can be derived from the glaucoma patient measurements is that the PS-OCT measurements are not sensitive enough to quantify DPPR/UD in areas of thin RNFL.

3.5 Discussion

Our measurements demonstrate that in the healthy retina of four young volunteers, the DPPR/UD varied as a function of sector around the ONH, with the lowest values ($0.10^\circ/\mu\text{m}$) occurring temporally and the highest values ($\sim 0.35^\circ/\mu\text{m}$) occurring inferiorly and superiorly. In SLP, a constant DPPR/UD is used as a conversion factor to convert measured DPPR to RNFL thickness. Because DPPR/UD varies as a function of sector, SLP phase retardation to thickness conversion does not yield accurate RNFL thicknesses in all sectors. Our DPPR/UD measurement does not rely on an accurate determination of the RNFL thickness. The DPPR/UD is determined from the slope of the phase retardation with depth as determined from a PS-OCT depth-resolved phase-retardation measurement.

Weinreb *et al.*³ found a correlation between RNFL thickness and phase retardation at different locations in the primate retina, but they did not consider a change in birefringence as a function of sector, which could explain the considerable variation around the regression line. Although the RNFL thickness of young healthy subjects may not be measured accurately with SLP, RNFL thinning induced by glaucoma changes the amount of phase retardation, which can be detected with SLP. In addition, phase-retardation changes caused by a change in RNFL birefringence, as we hypothesized earlier, are detected with SLP. With SLP, the combined effect of RNFL thickness and birefringence is measured as a DPPR of the RNFL, which makes it impossible to separate thickness from birefringence. SLP is sensitive to a combination of birefringence change and thickness change. PS-OCT measures RNFL thickness and the depth-resolved birefringence simultaneously and independently. Our data do not invalidate the clinical value of a phase-retardation measurement, such as is obtained with SLP, but affects the conversion of phase-retardation to RNFL thickness.

Thickness measurements of two glaucoma patients demonstrate the loss of retinal nerve fiber layer tissue as a result of glaucoma. Due to the thin RNFL, the DPPR/UD measurement becomes unreliable.

In order to measure glaucoma patients more reliably, the image signal-to-noise ratio has to be improved. This can be done by either improving the imaging optics, or by improving the sensitivity of the OCT system. Using a PS-OCT system that is based on spectral-domain technology, a sensitivity improvement of more than ~ 20 dB can be achieved.²⁶

The two groups of glaucoma patients and healthy volunteers were not age matched. For a good comparison between these two groups, patients and volunteers should have been selected from the same age groups, since the nerve fiber layer thins with age. The measurements in the oldest healthy volunteer of these experiments suggest that the phase retardation pattern of higher inferior and superior values becomes less pronounced with age. More measurements in that age group are needed to confirm this hypothesis.

3.6 Conclusion

The birefringence of healthy RNFL is constant as a function of scan radius but varies as a function of position around the ONH, with higher values occurring superior and inferior to the ONH. Measured DPPR/UDs around the ONH in two healthy subjects varied between 0.10 and 0.35 $^{\circ}/\mu\text{m}$. These values are equivalent to birefringence values of 1.2×10^{-4} and 4.1×10^{-4} , measured at a wavelength of 840 nm. Consequently, when assuming a spatially constant birefringence around the ONH, the conversion of SLP phase retardation measurements may yield incorrect thicknesses. Glaucoma patient measurements demonstrate nerve fiber layer thinning due to glaucoma. The PS-OCT measurements of glaucomatous RNFL are not sensitive enough to measure birefringence reliably.

References

1. H.A. Quigley, E.M. Addicks and W.R. Green, "Optic nerve damage in human glaucoma. III. Quantitative correlation of nerve fiber loss and visual field defect in glaucoma, ischemic neuropathy, papilledema, and toxic neuropathy," *Archives of Ophthalmology*, 100, 135-46 (1982).
2. D. Huang, E.A. Swanson, C.P. Lin, et al., "Optical coherence tomography," *Science*, 254, 1178-81 (1991).
3. R.N. Weinreb, A.W. Dreher, A. Coleman, et al., "Histopathologic Validation of Fourier-Ellipsometry Measurements of Retinal Nerve-Fiber Layer Thickness," *Archives of Ophthalmology*, 108, 557-560 (1990).
4. R.N. Weinreb, C. Bowd and L.M. Zangwill, "Glaucoma detection using scanning laser polarimetry with variable corneal polarization compensation," *Archives of Ophthalmology*, 121, 218-224 (2003).
5. Q.Y. Zhou and R.W. Knighton, "Light scattering and form birefringence of parallel cylindrical arrays that represent cellular organelles of the retinal nerve fiber layer," *Applied Optics*, 36, 2273-2285 (1997).
6. J.F. de Boer, T.E. Milner, M.J.C. van Gemert and J.S. Nelson, "Two-dimensional birefringence imaging in biological tissue by polarization-sensitive optical coherence tomography," *Optics Letters*, 22, (1997).
7. J.F. de Boer, T.E. Milner and J.S. Nelson, "Determination of the depth-resolved Stokes parameters of light backscattered from turbid media by use of polarization-sensitive optical coherence tomography," *Optics Letters*, 24, 300-302 (1999).
8. C.E. Saxer, J.F. de Boer, B.H. Park, et al., "High-speed fiber-based polarization-sensitive optical coherence tomography of in vivo human skin," *Optics Letters*, 25, 1355-1357 (2000).
9. B.H. Park, C. Saxer, S.M. Srinivas, J.S. Nelson and J.F. de Boer, "In vivo burn depth determination by high-speed fiber-based polarization sensitive optical coherence tomography," *Journal of Biomedical Optics*, 6, 474-9 (2001).
10. B. Cense, T.C. Chen, B.H. Park, M.C. Pierce and J.F. de Boer, "In vivo depth-resolved birefringence measurements of the human retinal nerve fiber layer by polarization-sensitive optical coherence tomography," *Optics Letters*, 27, 1610-1612 (2002).
11. B. Cense, T.C. Chen, B.H. Park, M.C. Pierce and J.F. de Boer, "In vivo birefringence and thickness measurements of the human retinal nerve fiber layer using polarization-sensitive optical coherence tomography," *Journal of Biomedical Optics*, 9, 121-125 (2004).
12. B. Cense, T.C. Chen, B.H. Park, M.C. Pierce and J.F. de Boer, "Thickness and birefringence of healthy retinal nerve fiber layer tissue measured with polarization-sensitive optical coherence tomography," *Investigative Ophthalmology & Visual Science*, 45, 2606-2612 (2004).

13. R.P. Hemenger, "Birefringence of a Medium of Tenuous Parallel Cylinders," *Applied Optics*, 28, 4030-4034 (1989).
14. X.R. Huang, H. Bagga, D.S. Greenfield and R.W. Knighton, "Variation of peripapillary retinal nerve fiber layer birefringence in normal human subjects," *Investigative Ophthalmology & Visual Science*, 45, 3073-3080 (2004).
15. L. Mandel and E. Wolf, *Optical Coherence and Quantum Optics*. 1995, Cambridge, England: Cambridge University Press.
16. M.J. Everett, K. Schoenenberger, B.W. Colston and L.B. Da Silva, "Birefringence characterization of biological tissue by use of optical coherence tomography," *Optics Letters*, 23, 228-230 (1998).
17. M.C. Pierce, B.H. Park, B. Cense and J.F. de Boer, "Simultaneous intensity, birefringence, and flow measurements with high-speed fiber-based optical coherence tomography," *Optics Letters*, 27, 1534-1536 (2002).
18. A.N.S.I., *Safe use of lasers*. 1993, Laser Institute of America: New York.
19. G.J. Tearney, B.E. Bouma and J.G. Fujimoto, "High-speed phase- and group-delay scanning with a grating-based phase control delay line," *Optics Letters*, 22, 1811-1813 (1997).
20. B.H. Park, M.C. Pierce, B. Cense and J.F. de Boer, "Real-time multi-functional optical coherence tomography," *Optics Express*, 11, 782-793 (2003).
21. N.V. Ifúmia, B.E. Bouma, J.F. de Boer, et al., "Adaptive ranging for optical coherence tomography," *Optics Express*, 12, 4025-4034 (2004).
22. E.A. Swanson, J.A. Izatt, M.R. Hee, et al., "In-Vivo Retinal Imaging by Optical Coherence Tomography," *Optics Letters*, 18, 1864-1866 (1993).
23. W. Drexler, H. Sattmann, B. Hermann, et al., "Enhanced visualization of macular pathology with the use of ultrahigh-resolution optical coherence tomography," *Archives of Ophthalmology*, 121, 695-706 (2003).
24. H.A. Quigley and W.R. Green, "The Histology of Human Glaucoma Cupping and Optic-Nerve Damage - Clinicopathologic Correlation in 21 Eyes," *Ophthalmology*, 86, 1803-1830 (1979).
25. D.J. Maitland and J.T. Walsh, Jr., "Quantitative measurements of linear birefringence during heating of native collagen," *Lasers in Surgery & Medicine*, 20, 310-8 (1997).
26. J.F. de Boer, B. Cense, B.H. Park, et al., "Improved signal-to-noise ratio in spectral-domain compared with time-domain optical coherence tomography," *Optics Letters*, 28, 2067-2069 (2003).

4. Spectral-domain optical coherence tomography

*Abstract**

In a time-domain system, only those photons returning from a certain depth (within the coherence window) are detected, making this technology rather inefficient. In spectral-domain optical coherence tomography (SD-OCT), photons returning from all depths are recorded simultaneously, making the technology more efficient than the time-domain variant. We theoretically and experimentally demonstrated a sensitivity improvement of SD-OCT over TD-OCT by a factor of 148 (21.7 dB). In addition, we demonstrated ultrahigh-speed *in vivo* human retinal OCT imaging at 29,300 depth profiles/s, resulting in cross-sectional imaging at a video rate with 6 μm resolution. Motion artifacts, commonly present in both research and commercial ophthalmic OCT systems were greatly reduced, thus minimizing the image distortion by involuntary eye movement.

We built a spectral-domain system with an ultra-broadband source. One disadvantage of such a source is that chromatic dispersion is induced, which decreases the axial resolution. After dispersion compensation in software, the coherence length measured from a mirror in air was equal to 4.0 μm ($n = 1$). The dispersion-compensated axial resolution obtained from a reflecting spot in the fovea was equal to 3.5 μm ($n = 1.38$). To our knowledge, this was the first coherence length measured in the human eye *in vivo*. The combination of high axial resolution measurements at a high data acquisition rate allows us to identify features that have not been seen in the human retina before with OCT. Comparing the performance of our ultrahigh-resolution SD-OCT system with a conventional high-resolution time-domain OCT system, the A-line rate of the spectral-domain OCT system was 59 times higher at a 5.4 dB lower sensitivity.

* This chapter is based on four articles that were earlier published in peer-reviewed journals:

J.F. de Boer, B. Cense, B.H. Park, et al., "Improved signal-to-noise ratio in spectral-domain compared with time-domain optical coherence tomography," *Optics Letters*, 28, 2067-2069 (2003).

N. Nassif, B. Cense, B.H. Park, et al., "In vivo human retinal imaging by ultrahigh-speed spectral domain optical coherence tomography," *Optics Letters*, 29, 480-482 (2004).

N.A. Nassif, B. Cense, B.H. Park, et al., "In vivo high-resolution video-rate spectral-domain optical coherence tomography of the human retina and optic nerve," *Optics Express*, 12, 367-376 (2004).

B. Cense, N.A. Nassif, T.C. Chen, et al., "Ultrahigh-resolution high-speed retinal imaging using spectral-domain optical coherence tomography," *Optics Express*, 12, 2435-2447 (2004).

4.1 Introduction

Glaucoma is a disease that affects the ganglion cells and their axons in the retina. When glaucoma is detected at an early stage, further loss of vision can be prevented by surgery or medication. The visual field test is the current standard method of detecting loss of peripheral vision in glaucoma. However, measurements show that up to 40% of nerves are irreversibly damaged before loss of peripheral vision can be clinically detected.¹ Evidence of glaucoma can be found from a decrease in thickness of the retinal nerve fiber (RNFL). A measurement method that can spatially map the thickness of the RNFL could be used in clinics to monitor the state of the RNFL. Thickness changes observed in follow-up measurements could be an indicator for glaucoma. Such a system could help clinicians to diagnose glaucoma at an early stage.

The development of a highly sensitive spectral-domain system for ultra-high resolution measurements was a process consisting of several steps. First, we proved theoretically and experimentally that spectral-domain (SD) OCT gives a considerable sensitivity advantage over time-domain (TD) OCT.² Next, we built a fast (29,300 spectra per second) spectrometer, where we optimized the efficiency such that as few photons as possible were lost.^{3, 4} An SD-OCT setup with this spectrometer in the detection arm was used for imaging of the human retina *in vivo*. In the last step, we replaced the ordinary broadband source with an ultra broadband source ($\Delta\lambda > 120 \text{ nm}$) and demonstrated ultra-high resolution imaging without a significant signal-to-noise penalty.⁵ Over the course of this process, a 150-fold sensitivity improvement and a nearly 100-fold imaging speed improvement was demonstrated.

4.2 Principle and sensitivity gain of SD-OCT

Here, we will derive expressions for the signal-to-noise ratio (SNR) for time-domain and spectral-domain systems.² By means of OCT measurements on an onion and on a weak-reflecting surface, the difference in SNR between these two systems will be demonstrated.

4.2.1 Theoretical derivation

The SNR of a TD-OCT system was first analyzed by Sorin and Baney⁶ and later by Hoeling *et al.*⁷ First, an expression for the signal will be derived followed by an expression for the noise terms in a shot-noise-limited TD-OCT system. In such a system, the signal is created by interference between reference and sample arm power. The signal, defined in terms of electrical power at the detector, can be expressed as:

$$S_{\text{signal}} = 2\eta^2 e^2 P_{\text{ref}} P_{\text{sample}} / E_v^2 \quad [A^2] \quad \text{Eq. 6}$$

Here η is the quantum efficiency of the detector, e is the charge of an electron, and E_v is the energy of a photon, which can be calculated from $E_v = hc/\lambda$ and h being Planck's constant, c is the speed of light in vacuum and λ is the wavelength. The reference and sample arm powers can be calculated from their respective measured spectra by integration:

$$P_{ref, sample} = \int S_{ref, sample}(\omega) d\omega \quad \text{Eq. 7}$$

When there is no spectral attenuation in the system, both the sample and reference spectra will be shaped like the source spectrum ($S(\omega)$, with $\omega = 2\pi f$, and f the frequency of the light) with the sample arm spectrum being strongly attenuated because of low sample reflectivity, i.e. $S_{ref}(\omega) = S(\omega)$ and $S_{sample}(\omega) = \alpha S(\omega)$ and $\alpha \ll 1$. Combining this information with the first two equations yields:

$$S_{signal} = 2\eta^2 e^2 \alpha \left(\int S(\omega) d\omega \right)^2 / E_v^2 \quad \text{Eq. 8}$$

Sorin and Baney and Hoeling *et al.* derived an expression for the contributions of thermal noise (detector noise), shot noise and relative intensity noise (RIN):^{6, 7}

$$N_{noise} = \frac{4kT}{R_{fb}} + \frac{2\eta e^2 P_{ref}}{E_v} + 2 \left(\frac{\eta e P_{ref}}{E_v} \right)^2 \tau_{coh} \quad [A^2 / Hz] \quad \text{Eq. 9}$$

In Eq. 9, a degree of polarization of 1 was assumed and k is Boltzmann's constant, T is the temperature [K], R_{fb} is the value of the transimpedance amplifier feedback resistor, used to model the electronic amplifier noise, and τ_{coh} is the coherence time of the source, equal to $\tau_{coh} = (2 \ln 2 / \pi)^{1/2} \lambda_0^2 / (c \Delta \lambda)$,⁸ with $\Delta \lambda$ equal to the full spectral width at half-maximum of a Gaussian source. A TD-OCT system is shot-noise-limited when the shot noise term dominates the other noise components, in other words when the second term in Eq. 9 is larger than the other two terms. From Eq. 6 to Eq. 9, the SNR of a shot-noise-limited TD-OCT system is given by:

$$SNR_{TD-OCT} = \frac{\eta \alpha P_{ref}}{E_v BW} \quad \text{Eq. 10}$$

where BW is the signal bandpass. As will be shown in section 4.2.2, the signal bandpass depends on the optical bandwidth, the scan speed and the depth range. In Eq. 9, we assumed a detection arm with one detector. If we spectrally disperse the shot-noise-limited detection signal over multiple (M) detectors, the amount of reference power on a single detector is equal to P_{ref} / M , and the electronic bandwidth

per detector (in Hz) is equal to the total bandwidth divided by the number of detectors, resulting in a noise contribution per detector of:

$$N_{noise} = \frac{2\eta e^2 P_{ref}}{E_v M} \frac{BW}{M} = \frac{2\eta e^2 P_{ref} BW}{E_v M^2} \quad [A^2] \quad \text{Eq. 11}$$

The total shot noise is equal to the sum of the shot noise on each detector, or $M \cdot N_{noise}$. Since the signal remains the same as in Eq. 8, the SNR of a system with multiple detectors becomes:

$$\frac{S_{signal}}{N_{noise}} = \frac{\eta P_{sample} M}{E_v BW} \quad \text{Eq. 12}$$

In a shot-noise-limited system where the light is spectrally dispersed over multiple detectors, the signal-to-noise ratio can therefore be improved by a factor equal to the number of detectors. The maximum number of detector elements M is determined by shot noise dominance, i.e. the shot noise term in Eq. 9 should be higher than the first and last terms. By increasing the number of detectors M , the coherence time in Eq. 9 increases by a factor equal to M , since the optical bandwidth per detector decreases (note that Eq. 9 is given in A^2 / Hz), increasing the RIN noise contribution. The maximum number of detector elements is reached when RIN noise and shot noise become equal. One could lower the RIN noise contribution by use of balanced detection, to allow a further increase in the number of detector elements M .

In a fully parallel SD-OCT system, the detected photons can be spectrally dispersed and temporally summed in a charged coupled device (CCD).⁹⁻¹¹ By use of Nyquist's theorem, the bandwidth per detector element (BW/M) is replaced by $1/(2\tau_i)$, where τ_i is the integration time of the array. Since fully parallel SD-OCT measures only the real part of the complex cross-spectral density (the interferometric signal in frequency-domain), the signal is reduced by a factor of 2, resulting in a SNR for a spectral-domain system as follows:

$$\frac{S_{signal}}{N_{noise}} = \frac{\eta P_{sample} \tau_i}{E_v} \quad \text{Eq. 13}$$

A similar equation was derived by Mitsui *et al.*¹² and Leitgeb *et al.*¹³ The SNR of a spectral-domain system improves with integration time and sample arm power. Interestingly, the SNR does not depend on bandwidth, as it does for a time-domain system (Eq. 10). In section 4.4, we will use this advantage to build an ultra-high resolution spectral-domain system.

4.2.2 Example calculation

In our experimental comparison, which will be described in the next section, we will measure an onion with both time-domain and spectral-domain systems. With use of Eq. 10 and Eq. 13, we can calculate the expected SNR gain of SD-OCT over TD-OCT. In the two systems, the sample arm power and energy of a photon will be equal. The quantum efficiency η for both systems is also assumed to be equal. The electronic bandwidth (BW) of the time-domain system was equal to approximately 80 kHz . This was calculated as follows. The A-line rate was 256 A-lines per second, with an A-line length of 1.4 mm , resulting in a velocity of the reference mirror of $1.4 \cdot 256 = 358 \text{ mm} / s$. The center wavelength of the source was approximately 840 nm , while the wings of the spectra started and ended at approximately 800 and 880 nm (see Figure 4 of Chapter 2). Therefore, the electronic bandwidth in this TD-OCT setup was equal to:

$$\Delta f = f_2 - f_1 = \frac{2 \cdot v}{\lambda_2} - \frac{2 \cdot v}{\lambda_1} = \frac{717 \cdot 10^{-3}}{800 \cdot 10^{-9}} - \frac{717 \cdot 10^{-3}}{880 \cdot 10^{-9}} = 81 kHz \quad \text{Eq. 14}$$

The integration time τ_i was equal to 4 ms . The ratio between the SNR of a spectral-domain system and a time-domain system can be determined by:

$$\frac{SNR_{SD-OCT}}{SNR_{TD-OCT}} = \tau_i \cdot BW = 4 \cdot 10^{-3} \cdot 81 \cdot 10^3 = 324 \quad \text{Eq. 15}$$

The SNR of the SD-OCT system will be a factor of 324, or 25 dB higher than the SNR of a TD-OCT system, assuming identical detector sensitivities.

4.2.3 Image reconstruction in SD-OCT

The spectra that are acquired with a spectrometer in a SD-OCT setup are the result of interference between light returning from sample and reference arms. One can describe the measured intensity in the detection arm $I(k)$, with $k=2\pi/\lambda$ as a function of the intensities in the sample arm, $I_s(k)$, and reference arm, $I_r(k)$ by:⁴

$$I(k) = I_r(k) + 2\sqrt{I_s(k)I_r(k)} \sum_n \alpha_n \cos kz_n + I_s(k) \quad \text{Eq. 16}$$

with α_n equal to the square root of reflectivity values at different depths z_n in the sample. A Fourier transformation links z and k space. Because of the nonlinear relation between k and λ , spectra have to be interpolated first to create evenly spaced samples in the k -domain.¹¹ The middle term contains the depth-dependent information, and consists of a modulation of the source spectrum. In fact, a single mirror surface in the sample arm yields a modulation of the detected spectrum at one single frequency. This frequency increases when the path length difference between sample and reference arm increases. Since additional surfaces will superimpose

modulations, the so-called cross-spectral density function is the spectrum as measured by the spectrum analyzer that contains all spectral modulations caused by reflections at different depths in the sample arm.

One can reconstruct the locations and amplitudes of these reflections by a Fourier transform, yielding the following convolution:^{4,10}

$$FT^{-1}(I(k)) = \Gamma(z) \otimes (1 + \sum_n \alpha_n \delta(z - z_n) + \sum_n \alpha_n \delta(z + z_n) + O[I_s(k)]) \quad \text{Eq. 17}$$

with the coherence function represented by $\Gamma(z)$; the second and third terms describe the interference of the reference arm with the sample arm. The final term represents the autocorrelation due to interference within the sample arm; this term is ignored. After taking the absolute value of this Fourier transform, an A-line is created with reflected intensities encoded as a function of distance z . Multiple adjacent A-lines can be reconstructed in a B-scan or structural intensity image.

4.2.4 Preliminary experimental comparison

To quickly verify the sensitivity gain of SD-OCT over TD-OCT, we built a measurement setup (see Figure 24) using off the shelf components and an existing TD-OCT setup. This system could measure *in vitro* samples with both concepts without any signal loss due to connector changes.

For the TD-OCT measurements, we modified a fiber-based setup that was previously used for polarization-sensitive retinal nerve fiber layer birefringence measurements as described in Chapter 3.¹⁴ For the SD-OCT measurements, we used a commercially available spectrometer (Ocean Optics HR-2000) in the detection arm. Both systems operated in the shot noise limit. The spectrometer was adequate for the experiment described here, but was not optimized for our operation wavelength. The line scan chip in the optical spectrometer had its highest sensitivity around 500 *nm*. In the near-infrared part of the spectrum around 800 *nm* the sensitivity was expected to drop by a factor of 4.¹⁵ Furthermore, the spectrometer was employed with a reflection diffraction grating, which is not as efficient as a state of the art transmission diffraction grating ($\sim 30\%$ efficiency versus $\sim 95\%$ efficiency).¹⁵

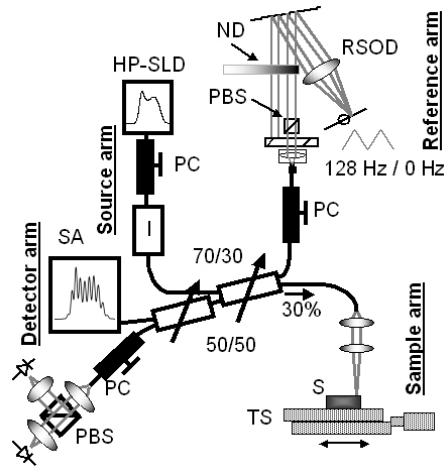


Figure 24: Setup for SNR comparison measurement. A high-power superluminescent diode (HP-SLD) was coupled through an isolator (I), with maximum transmission achieved by alignment of the major polarization component of the source with the optic axis of the isolator by means of a polarization controller (PC). Light was split by a fiber coupler with 70% sent towards a rapid scanning delay line (RSOD) with a variable neutral density filter (ND) and a polarizing beam coupler (PBS) and 30% towards the sample arm. In the sample arm, a sample (S) was positioned in the focal plane of the focusing lens. The spot size diameter was approximately $20\ \mu\text{m}$. By means of a computer-controlled translation stage, the beam could be scanned across the sample. Light returning from the sample interfered with light returning from the reference arm, after which it could be detected in the detector arm. Here, a 50/50 fiber coupler divided the interference signal equally over a time-domain based detector – a polarization-sensitive detector consisting of a PBS and two silicon detectors - and an Ocean Optics optical spectrum analyzer (SA), the spectral-domain based detector.

For the measurements described here, the polarization controllers of the polarization sensitive setup were set such that all light was sent towards one single detector, guaranteeing optimal transmission. A high-power superluminescent diode, protected and polarized by an isolator, generated a spectrum with a FWHM bandwidth of $50\ \text{nm}$, centered around $840\ \text{nm}$ with an output power of approximately $4.6\ \text{mW}$. 70 percent of the light was directed towards a rapid scanning optical delay line (RSOD) in the reference arm, while 30 percent was sent towards the sample arm by means of a 70/30-fiber coupler. The sample arm comprised a collimator, a focusing lens and a computer controlled translation stage. B-scans with a length of $2.5\ \text{mm}$ were made in 2 seconds by shifting the translation stage. In the detection arm, a 50/50 fiber coupler directed half of the light towards the time-domain detector and the other half to the Ocean Optics spectrum analyzer, allowing for a quick change between imaging systems without sample arm changes and transmission losses. The detector in the TD-OCT setup consisted of a silicon PIN detector in a

transimpedance configuration. Data was acquired through a National Instruments AD board and stored to hard disk. During one TD-OCT B-scan, 512 A-lines were acquired in 2 seconds. The acquired data was analyzed afterwards, as described in Chapter 3. Each A-line had a length of 1 *mm* in tissue ($n = 1.38$) and a B-scan was 2.5 *mm* wide. In order to compare the time-domain data with spectral-domain data, the part of the image that was affected by variations in the speed of the translation stage was cut out.

The setup as described above was slightly modified for the SD-OCT measurements. The galvanometer mirror in the RSOD was not powered and set in one position, since depth scanning in a SD-OCT system occurs in the detector arm. In addition, a variable neutral density filter wheel in the RSOD attenuated the reference arm power until the signal in the spectrum analyzer was just below saturation. After each translation of 5 μm , a pause was introduced to stabilize the translation stage, after which a spectrum was grabbed with the spectrometer and transferred to hard disk. One B-scan comprised of 512 steps. The integration time per spectrum was 4 *ms*, thus making it equal to the time it took to acquire one A-line with the TD-OCT configuration.

To extract an A-line from a spectrum, the spectrum was first converted to k -space with k being equal to $2\pi/\lambda$. From this data, an A-line was created by means of a Fourier transformation. After squaring and adding up real and imaginary parts, values were plotted on a logarithmic scale. A complete image consisted of 512 A-lines with a width of 2.5 *mm* and a depth equal to approximately 3 *mm*. The image was cut such that it overlapped well with the time-domain data.

Measurements were performed on an onion and samples were covered with water and a microscope cover slide. The slide was put at an angle with respect to the scanning beam to avoid specular reflections.

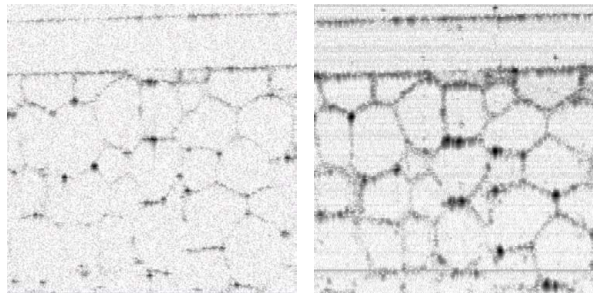


Figure 25: TD-OCT image (left, 1 x 1 *mm*, dynamic range of 45 *dB*) compared with SD-OCT image (right, 1 x 1 *mm*, 55 *dB*) of an onion. Individual onion cells covered with a microscope slide can be seen. Horizontal lines in the SD-OCT image are caused by fixed pattern noise.

Figure 25 demonstrates an SNR improvement of SD-OCT over TD-OCT, with a gain of approximately 10 *dB*. Earlier in section 4.2.2, we calculated that the SD-OCT system should outperform the TD-OCT system by 25 *dB*. The difference of 15 *dB* is most likely caused by losses in the spectrometer due to an inefficient transmission grating and a line scan chip that was not optimized for our wavelength.¹⁵ Additional measurements indicated that the efficiency of the spectrometer was only 2%, which is a factor of 40, or 16 *dB* smaller than the 85% quantum efficiency of the time-domain system. This number matched well with the 15 *dB* difference that was observed in the onion data.

With this experiment, we validated the earlier described theory and demonstrated the signal-to-noise gain of a spectral-domain system.

4.3 High-speed spectral-domain optical coherence tomography

After the preliminary experiments on the onion using off the shelf components, we built an efficient ultra high-speed spectrometer,^{3, 4} used it in the detection arm of our interferometer to quantify its performance, and created images and movies of the human retina *in vivo*.

4.3.1 Setup

In Figure 26 the experimental setup is shown. Briefly, the source was a superluminescent diode (Superlum, Moscow, Russia) with a polarized power of 4.6 *mW* and a FWHM spectral width of 50 *nm* centered at 840 *nm*. In the interferometer configuration employed here, an 80-20 fiber coupler was used, such that 20% of the source light was directed to the slit lamp, where the power incident on the eye was limited to 600 μ *W* by the American National Standards Institute (ANSI) maximum permissible exposure.¹⁶ Upon return from the slit lamp, 80% of the light was directed to the detection arm, resulting in improved collection efficiency. To acquire the cross-spectral density in the detection arm, a high-speed spectrometer was constructed. The light emitted from the detection arm fiber tip was collimated by a lens with a focal length of 50 *mm*. The collimated beam was incident on a 1200-lines/*mm* transmission grating with a diffraction efficiency of 95%. Diffracted light was then focused onto a 2048-element line scan camera (Basler, Ahrensburg, Germany) with a pixel size of 10 μ *m* x 10 μ *m* by a three-element lens with a focal length of 100 *mm*. The maximum line rate of the camera was 29.3 *kHz* and data could be transferred continuously to computer host memory by CameraLink at a resolution of 10 bits/pixel. The quantum efficiency η of the spectrometer–detector combination was 28%, which was determined by the ratio of the optical power detected by the line scan camera and the power measured at the detection arm fiber tip with an optical power meter. The spectral range of the spectrometer was 150 *nm*, and the design spectral resolution $\delta\lambda$

was 0.075 nm (150 nm optical bandwidth distributed over 2048 pixels) at a center wavelength λ_0 of 840 nm .

In SD-OCT the depth range z_{max} is inversely proportional to the spectral resolution $\delta\lambda$ and is given by:¹⁰

$$z_{max} = \frac{\lambda_0^2}{4n\delta\lambda} \quad \text{Eq. 18}$$

resulting in a depth range of 2.3 mm in air or 1.7 mm assuming a refractive index of $n = 1.38$ in the eye.

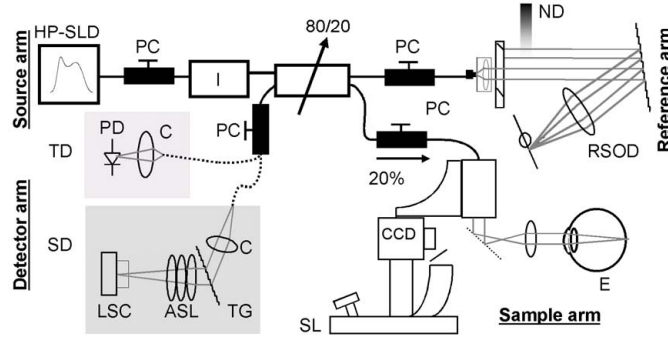


Figure 26. Schematic of the experimental setup. HP-SLD, source; I, polarizer and isolator; 80-20, fiber-based 80-20 coupler; RSOD, rapid-scanning optical delay line; ND, neutral-density filter; SL, slit-lamp-based telecentric scanner; E, eye; TD, TD-OCT configuration; C, collimator; PD, photodiode; SD, SD-OCT configuration; TG, transmission grating; ASL, three-element air-spaced lens; LSC, line scan camera; PC, polarization controller. For SD-OCT measurements, the RSOD was not scanned and was used for dispersion compensation only.

Spectrometer calibration

The spectra that were acquired with the high-speed spectrometer were not linearly spaced in wavelength space. The grating equation and three-element air-spaced lens in the spectrometer determined the distribution of wavelengths over the CCD-array. In section 4.2.4, a similarly laid-out Ocean Optics spectrometer was used which calibrated by the manufacturer, such that the intensity was linear as a function of wavelength, allowing a direct interpolation of the data from wavelength to k -space. In the high-speed spectrometer – simplified - four parameters influenced the wavelength distribution:

- the angle of the collimated beam incident on the grating,
- the distance between two lines in the grating,
- the distance between the focusing lens and the CCD array,
- the position of the center wavelength on the CCD array.

Before a conversion of the acquired data to k -space, these parameters were used to determine how the wavelengths were spaced on the CCD array. With this new wavelength array, the data was mapped to k -space.

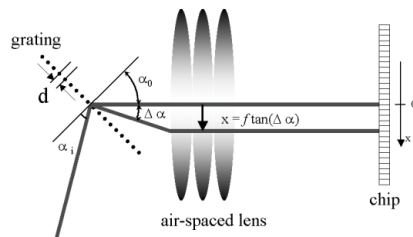


Figure 27: Collimated light that is incident on a transmission grating is dispersed and focused on a linear CCD array. In our system, when the center wavelength λ_0 makes an angle α_0 with the grating, this wavelength component is imaged onto the center of a CCD line scan chip. Wavelengths different from λ_0 are dispersed with angles smaller and larger than θ_0 . The position of λ on the chip depends on the focal length of the lens, the distance between two lines (d) in the grating, and the angle incident on the chip α_i .

We used the following expression, based on the grating equation, to determine the wavelength distribution on the camera:

$$\lambda(x) = d \left(\sin \left(\sin^{-1} \left(\left(\frac{\lambda_0}{d} \right) - \sin(\alpha_i) \right) \right) + \tan^{-1} \left(\frac{x}{f_{length}} \right) + \sin(\alpha_i) \right) \quad \text{Eq. 19}$$

with the distance between two lines in the grating d , a center wavelength λ_0 , an incident angle α_i , a focal length f and a distance x from the location of λ_0 . In our case, the incident angle was 30° , resulting in a factor of 0.5, since $\sin(30^\circ) = 0.5$. The size of one pixel was $10 \mu m$, a number that was necessary to convert the pixel location to x .

By comparing the phase $\theta(k)$ measured from a mirror at different path length differences, we found that it is relatively easy to determine the correct spectrometer parameters, through a process shown schematically in Figure 28.

At least three measurements on a mirror were performed for this calibration. Measurements were performed at various path length differences covering the full imaging depth. With use of an analysis program, a matrix of multiple focal length and center wavelength value combinations was used to map (M) and interpolate (I) the data multiple times to k -space. Then, the phase $\theta(k)$ for each measurement and each of these combinations was determined. To determine the phase term $\theta(k)$, the spectrum was Fourier transformed to ζ -space, where it was shifted such that the coherence function was centered on the origin. A complex spectrum in k -space was obtained after an inverse Fourier transformation. The phase term $\theta(k)$ was equal to the arctangent of the imaginary component divided by the real component. Only with an optimized combination of focal length and center wavelength did the mapping yield

phases that were the same for measurements obtained at all different path length differences.

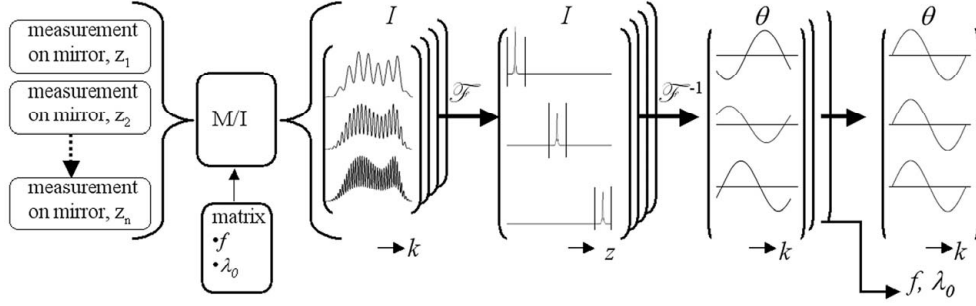


Figure 28. Flow chart for the determination of optimized spectrometer parameters, focal length (f) and center wavelength (λ_0). Measurements at several path length differences on a mirror were mapped (M) and interpolated (I) to k -space with use of several combinations of focal length and center wavelength values. The resulting spectra were Fourier transformed to z -space, after which the coherence function was cut out and return transformed. For each combination of focal length and center wavelength, the phase (θ) was determined. A combination of the optimized center wavelength and focal length lead to phase graphs that did not change as function of depth (z).

Finally, with the correct parameters established, a new wavelength array $\lambda(n)$, with $1 \leq n \leq$ maximum number of pixels used, was made with which raw data was mapped to k -space. In addition, this method could be used to compensate for dispersion compensation in the setup. We will come back to this later in section 4.4.1, when we discuss the use of ultra-broadband sources.

4.3.2 Noise performance

The different noise components present in the system were measured and analyzed to demonstrate that the system's performance was shot-noise-limited. The output of the line scan camera is related to the number of photons that are incident on each pixel, and since these photons release electrons from the semiconductor material, we will first derive an expression for the relationship between the incident reference power $P_{ref}(\lambda)$ on a certain bin of the camera, and the mean number of detected electrons:

$$\bar{N}_e(\lambda) = \frac{\eta P_{ref} \tau_i}{E_v(\lambda)} \quad [\# \text{ of electrons}] \quad \text{Eq. 20}$$

An OCT system is shot-noise-limited when the shot noise dominates other noise terms such as thermal noise and relative intensity noise. Shot noise is caused by quantization of light and charge, and results in a fluctuation of the number of detected electrons as a function of time. Per definition, the shot noise is equal to the square

root of the number of detected electrons:

$$N_{sn}(\lambda) = \sqrt{\left\langle \left(N_e(\lambda) - \bar{N}_e(\lambda) \right)^2 \right\rangle} = \sqrt{\bar{N}_e(\lambda)} \quad [\# \text{ of electrons}] \quad \text{Eq. 21}$$

where the $\langle \rangle$ brackets indicate ensemble averaging (averaging over a large number of measurements). The CCD camera measures the number of detected electrons as a pixel value, with values ranging from 0 to 1024 (10-bits). Using an analogue-to-digital conversion resolution of Δe , which corresponds to the number of electrons required for an incremental increase of 1 pixel value, we obtain the following expression for the pixel value:

$$I_{e,pv}(\lambda) = \frac{N_e(\lambda)}{\Delta e} \quad [\text{pixel value}] \quad \text{Eq. 22}$$

where $I_{e,pv}(\lambda)$ is the noise-free value of a certain bin in pixel values. The variance is a quantity that can help us determine if the system is shot-noise-limited. The variance of the number of detected electrons is defined as:

$$\begin{aligned} \sigma_e^2 &= \frac{1}{n-1} \sum_{j=1}^n (N_{e,j} - \bar{N}_e)^2 = \left\langle \left(N_e - \bar{N}_e \right)^2 \right\rangle \quad [\# \text{ of electrons}^2] \\ \sigma_e^2(\lambda) &= \left\langle \left(\frac{N_e(\lambda)}{\Delta e} - \frac{\bar{N}_e(\lambda)}{\Delta e} \right)^2 \right\rangle \quad [\text{pixel value}^2] \end{aligned} \quad \text{Eq. 23}$$

In a system that is purely shot-noise-dominated, the variance in pixel value is entirely caused by shot noise. Using Eq. 21, $\sigma_e^2(\lambda)$ can be written as:

$$\sigma_e^2(\lambda) = \frac{\bar{N}_e(\lambda)}{\Delta e^2} = \frac{\Delta e \bar{I}_{e,pv}}{\Delta e^2} = \frac{\bar{I}_{e,pv}}{\Delta e} \quad [\text{pixel value}^2] \quad \text{Eq. 24}$$

According to this last expression, the variance in a shot-noise-limited signal is equal to the noise-free pixel value, divided by Δe . In addition to shot noise, the line camera also has read-out and dark noise:

$$\sigma^2(\lambda) = \frac{I_{e,pv}(\lambda)}{\Delta e} + \sigma_{r+d}(\lambda)^2 \quad [\text{pixel value}^2] \quad \text{Eq. 25}$$

The first term on the right hand side of Eq. 25 is the shot noise contribution and the second term is the read-out contribution to the total noise. The measured read-out and shot noise at a 29.3 kHz read-out rate are shown in Figure 29. The noise was determined by calculating the variance at each camera pixel for 1000 consecutive spectra. Dark noise measurements were taken with the source light off. Only light

returning from the reference arm was used to measure the shot noise in the system. The noise component $I_{sn,PV}$ was averaged out from the mean intensity $I_{e,PV}$ by averaging over 1000 spectra. The CCD well depth was determined by fitting the theoretical expression for shot noise to the measured shot noise, using Δe and $I_{e,PV}$ as the fitting parameters and limiting the fit to the central 700 pixels. From this measurement, Δe was calculated to be 173 electrons. Assuming that the maximum pixel value corresponds to the full well depth, a well depth of 177,000 electrons was calculated. Shot-noise-dominated read-out and dark noise when the intensity reached 6% of the saturation value, i.e. shot-noise-limited detection was achieved over 90% of the useful bandwidth of the spectrum. Relative intensity noise (RIN) is never dominant in this setup, since the maximum power per pixel (4.6 nW) at a 34.1 μs integration time does not meet the criteria for RIN dominated noise, as was expressed in Eq. 9.

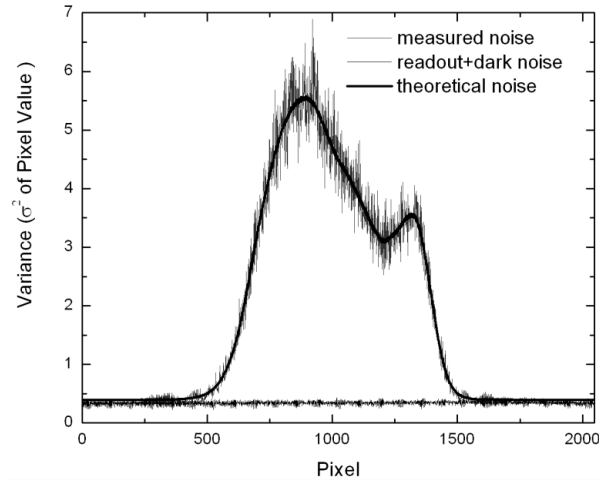


Figure 29. Noise components in the spectrometer. The shot noise level was determined with illumination of the reference arm only, and was used to determine the A/D resolution of the detector. The theoretical shot noise curve was fit using Eq. 24 to the measured average spectrum ($I_{e,PV}$), giving an analogue to digital conversion Δe of 173 electrons and a corresponding well depth of 177,000 electrons. A color image can be found on page 122.

4.3.3 Sensitivity analysis

In SD-OCT, signal sensitivity is strongly dependent on depth within an image. This is partly the result of the finite width of the pixels in the detector array, which spatially integrate the interference spectrum. Hence higher frequencies are washed out, and all frequencies receive a SNR penalty. This effect can be counteracted somewhat by use of a zero-padding technique,^{17, 18} where the number of samples in detector space is increased. For instance, the spectrum presented in Figure 29

contained 2048 points. We can increase the density of points by for instance a factor of four, by Fourier transforming the spectrum, padding the edge of the array with $7(n \times 2 - 1 = 7)$ times 2048 zeros such that the return Fourier transform displays the same spectrum distributed over 8192 points (the negative Fourier components are ignored). Zero-padding reduces aliasing effects at the high frequencies, as is evident from the resulting noise floor as a function of frequency, as demonstrated in Figure 31. To characterize our system sensitivity as a function of ranging depth, 1000 A-lines were acquired at an acquisition speed of $34.1 \mu\text{s}/\text{A-line}$ for 9 different positions of a weak reflector in the sample arm. The reflected sample arm power was 1.18 nW for all reflector positions. Without zero-padding, the noise floor decayed by 5 dB between a depth of $500 \mu\text{m}$ and 2 mm , and the peak signal dropped by 21.7 dB over the first 2 mm .

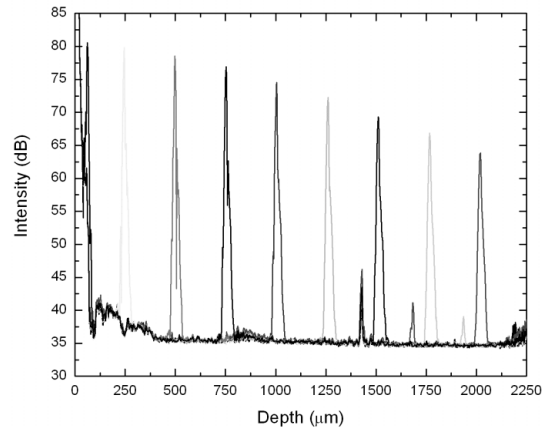


Figure 30. The depth-dependent loss in signal sensitivity from a weak reflector. The signal decayed 16.7 dB between 0 and 2 mm . The peaks at 1.4 mm , 1.6 mm , and 1.85 mm are caused by fixed pattern noise.

In spectral-domain OCT, the reference arm power returning to the detection arm may contain multiple superimposed discrete oscillations at different frequencies that, when recorded by the line scan camera in the spectrometer, produce horizontal lines in the structural intensity image. We call these artifacts “fixed pattern noise”. Due to fixed-pattern noise, the true noise floor could not be determined between 0 and $500 \mu\text{m}$. After zero-padding, a 16.7 dB loss in peak signal was noted across the first 2 mm , whereas the noise level dropped by only 0.4 dB between $500 \mu\text{m}$ (35.1 dB) and 2 mm (34.7 dB), as seen in Figure 30. The zero-filling method produced a nearly constant noise level and improved the signal by more than 5 dB at the greatest depths in the scan. Although zero-filling did not change the local SNR, this method eliminated the shoulders that are present at larger scan depths.¹⁷ The decay in both the signal and the noise level across the entire scan length of 2.4 mm have been theorized to amount to 4 dB as a result of the finite pixel width.¹³ As demonstrated by the experimental data, the

noise level decayed by less than 4 *dB* over the entire scan length, which we attribute to the statistical independence of the shot noise between neighboring pixels of the array. Thus, the finite pixel width does not introduce a decay of the noise level.

The finite spectrometer resolution introduces a sensitivity decay¹⁹ similar to that introduced by the finite pixel size.¹³ Convolution of the finite pixel size with the Gaussian spectral resolution yields the following expression for the sensitivity reduction, *R*, as a function of imaging depth *z*:¹⁹

$$R(z) = \frac{\sin^2(\pi z / 2d)}{(\pi z / 2d)^2} e^{\left(\frac{\pi^2 \omega^2 (z/d)^2}{8 \ln 2} \right)} \quad \text{Eq. 26}$$

where *d* is the maximum scan depth, and ω is the ratio of the spectral resolution to the sampling interval. Equation 32 was fit to the signal decay data presented in Figure 30 with ω as a free parameter, and the result shown in Figure 31. Due to its proximity to the autocorrelation peak, the first data point was not included in the fit. The value for ω obtained from the fit was 1.85, demonstrating that the working spectral resolution was 0.139 *nm*. The design spectral resolution was 0.075 *nm*.

The SNR was determined by the ratio of the peak at 250 μm (79.8 *dB*) and the noise level. Due to the fixed-pattern noise at 250 μm , the noise level was determined to be 35.2 *dB* by extrapolation of the linear region between 0.5 and 2 *mm*. The resulting SNR of 44.6 *dB* for 1.18 *nW* returning to the detection arm was 2.2 *dB* below the theoretical value given by Eq. 13 of 46.8 *dB*, for an integration time of 34.1 μs , a central wavelength of 840 *nm* and a spectrometer efficiency of 28%. With 600 μW of power incident on an ideal reflector in the sample arm, the measured power returning to the detection arm was 284 μW . The sum of the SNR at 1.18 *nW* (44.6 *dB*) and the 10 log ratio of maximum (284 μW) over measured (1.18 *nW*) power (53.8 *dB*) gives a sensitivity of 98.4 *dB*.

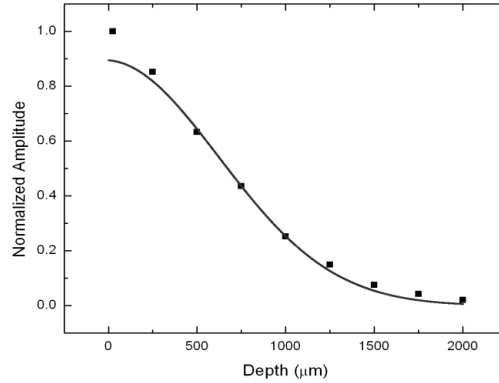


Figure 31. Decay of sensitivity across the measurement range. Symbols: Peak intensities of data presented in Figure 30. Solid line: Fit of Eq. 26 to the data points.

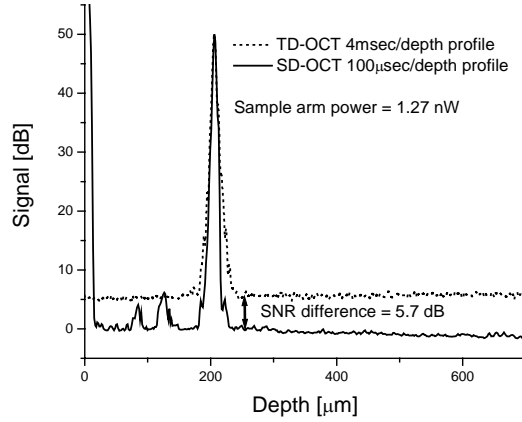


Figure 32. Comparison of SNR in TD-OCT and SD-OCT with the same weak-reflecting surface in the sample arm. Dotted curve, average of 256 depth profiles with the TD-OCT system. Solid curve, average of 256 depth profiles from the SD-OCT system. The large peak at zero in the SD-OCT profile is due to the DC term of the spectrum. The SD-OCT system has a 5.7 *dB* higher SNR than the TD-OCT system, at a 40-fold higher acquisition speed. The depth axis was scaled to reflect ranging assuming a medium with a refractive index of $n = 1.38$.

To compare directly the SNR performance of TD-OCT and SD-OCT, a weak reflector was placed in the sample arm of our system. The power reflected by the weak reflector measured at the fiber tip in the detection arm was 1.3 *nW*. The polarization states of sample and reference arm light were carefully aligned to maximize interference. First, 256 depth profiles at a speed of 4 *ms* per depth profile were acquired with our TD-OCT system, scanning over a depth of 1.4 *mm* in air. The signal pass bandwidth (*BW*) was 100 *kHz*. Then the detection arm was connected to the spectrometer, and 256 spectra were acquired at a speed of 100 μ s per spectrum. To reduce fixed pattern noise in the SD-OCT measurement,¹³ each individual spectrum was divided by the average of 1000 reference arm spectra. The resulting spectrum was multiplied by a Gaussian function to reshape the spectrum.²⁰ Spectra were then interpolated to create evenly spaced samples in the *k*-domain¹¹ before Fourier transformation of the spectra to generate depth profiles. Figure 32 shows 256 averaged depth profiles acquired with each configuration, demonstrating a SNR of 44.3 and 50 *dB* for TD-OCT and SD-OCT, respectively. Both depth profiles were normalized on the reflectivity peak and the TD-OCT measurement was shifted such that the peaks coincide. Some fixed pattern noise was still present in the SD-OCT measurement, resulting in peaks at 84 and 126 μ m. Since the SD-OCT system was 5.7 *dB* more sensitive and operated at a speed 40 times faster (corresponding to 16 *dB*) than the TD-OCT system, the combined sensitivity improvement was 21.7 *dB* or a factor of 148. The theoretical shot-noise-limited SNR in TD-OCT and SD-OCT are

46.7 *dB* and 51.9 *dB*, where $\eta = 0.85$ was used for a photodiode in TD-OCT. The measured TD-OCT and SD-OCT SNRs were 2.4 and 1.9 *dB* less than the theoretical optimal performance respectively, where 1 *dB* in TD-OCT was determined to be due to thermal noise contributing to the total noise. The measured coherence function FWHM was 8.3 μm in air, corresponding to 6 μm in tissue ($n = 1.38$).

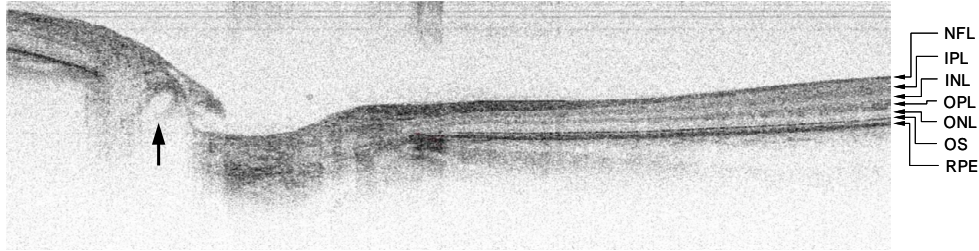


Figure 33. *In vivo* SD-OCT image of the human retina around the optic nerve head, consisting of 1000 depth profiles acquired in 34 *ms*. Dimensions are 6.4 *mm* wide x 1.7 *mm* deep. The dynamic range within the image was 40 *dB*. The image shows features that can be identified as²¹ the nerve fiber layer (NFL), inner plexiform layer (IPL) inner nuclear layer (INL), outer plexiform layer (OPL), outer nuclear layer (ONL), interface between the inner and outer segments of the photoreceptors (OS), and retinal pigmented epithelium (RPE). A blood vessel (indicated with an arrow) can be distinguished near the left side of the optic nerve head.

To demonstrate the ability of our SD-OCT system to acquire high-quality retinal images *in vivo* at ultrahigh speed, the right eye of one human volunteer was measured using an incident power on the cornea of 580 μW . Figure 33 shows an image of an area around the optic nerve head, acquired in 34.1 *ms*, constructed from 1000 consecutive spectra with an integration time per spectrum of 34.1 μs . To reduce the fixed pattern noise, individual spectra were not corrected with a separately acquired reference spectrum,¹³ but with a spectrum obtained by averaging over the same 1000 spectra from the image. The ratio of the maximum value within the image to the average noise level at a depth of 500 μm was 40 *dB*. To optimize the display, the image was grayscale coded over a dynamic range of 40 *dB*, from 4 *dB* below the maximum value (saturating a small number of data points) to 4 *dB* below the average noise level at 500 μm . The image shows detailed structures of the optic nerve head and layers of the retina, similar to TD-OCT imaging of the retina.²¹ The presence of fixed pattern noise is visible as horizontal lines in the image.

4.4 Ultrahigh-resolution SD-OCT

Compared to histology, one drawback of TD-OCT is its limited lateral and axial resolution. The lateral resolution of the technique is limited by the optics of the eye, i.e. the focal length, corneal aberrations and pupil diameter,²² and the optical design of the setup. Without adaptive optics, the combination of these parameters leads to a lateral resolution of approximately 20-30 μm . The axial resolution of an OCT system may be defined in terms of the coherence length, l_{coh} , which is determined by the center wavelength and bandwidth of the source and the index of refraction of the medium. The relationship between these four quantities is:²³

$$l_{coh (FWHM)} = \frac{2 \ln 2 \cdot \lambda_0^2}{\pi \cdot \Delta \lambda \cdot n} \quad \text{Eq. 27}$$

with λ_0 the center wavelength, $\Delta \lambda$ the spectral full width at half maximum (FWHM) of the source, and n the refractive index of the medium. The axial resolution can therefore be improved by either decreasing the value of the center wavelength, or increasing the bandwidth of the source. Shifting the center wavelength towards the blue is not practical because sources with shorter center wavelengths are not widely available, and the maximum permissible retinal exposure decreases significantly with decreasing wavelength.¹⁶ *In vivo* OCT measurements with an axial resolution of $\sim 1 \mu m$ can be made using a Ti:sapphire laser with a bandwidth of 350 nm centered around 800 nm.²⁴ Drexler *et al.* obtained retinal images with an axial resolution of 3 μm ,²¹ using a technique called ultrahigh-resolution optical coherence tomography (UHR-OCT).^{21, 24, 25}

The image quality or signal-to-noise ratio (SNR) of a shot-noise-limited TD-OCT system depends on several factors, as explained earlier in this chapter.²³ In this section, we will expand the earlier derived expression:

$$SNR_{TD-OCT} = \frac{\eta \cdot P_{sample}}{E_v \cdot BW} \propto \frac{P_{sample} \cdot l_{coh}}{l_{depth} \cdot A_{rate}} \quad \text{Eq. 28}$$

with η the quantum efficiency of the system, P_{sample} the power incident on the sample, E_v the energy of a photon, BW the detection bandwidth, l_{depth} the scan length of an A-line and A_{rate} the A-line rate. From Eq. 28, application of a source with a larger bandwidth decreases SNR due to the increased detection bandwidth required. In order to maintain the same SNR, either A-line rate or axial scan length should be decreased, or the power incident on the sample should be increased. A slower A-line

rate increases the chance of motion artifacts due to involuntary eye movement, while a shorter axial scan length makes it more difficult to keep the image window locked on the human retina during *in vivo* measurements. If the dwell time of the imaging spot on the retina is kept short, ANSI standards allow an increase in sample arm power.¹⁶ Short dwell times can be achieved if the OCT beam is scanned sufficiently fast over the retina. Hitzenberger *et al.* performed ophthalmic TD-OCT with short dwell times and incident power of up to 10 *mW*.²⁶ In previous measurements with our ophthalmic TD-OCT system, the power incident on the eye was less than 600 μW , because this power level is known to be safe for dwell times of up to eight hours.^{14, 27} An increase in sample arm power to 10 *mW* could result in more than a tenfold increase in SNR. However, more power is required and inexpensive powerful sources with a large bandwidth are not readily available. For current clinical ophthalmic applications of UHR-OCT, either a lower SNR or a slower A-line rate is taken as a penalty. One may be able to avoid such a penalty by using a more sensitive technique.

In the first part of this chapter, we introduced spectral-domain optical coherence tomography (SD-OCT). The SNR of a shot-noise-limited SD-OCT system was earlier defined in Eq. 13 as $\eta P_{\text{sample}} \tau_i / E_p$. The SNR performance of an SD-OCT system improves with increasing sample arm power or increased integration time. Most importantly, Eq. 13 shows that the SNR performance of an SD-OCT system is independent of the bandwidth of the source. In theory, by combining SD-OCT with an ultra-broadband source, high-resolution imaging at high acquisition rates should become within reach. This new technique may facilitate the diagnosis and monitoring of several ocular diseases, such as glaucoma, diabetic retinopathy, cancer and age-related macular degeneration. The first *in vivo* retinal SD-OCT images were presented by Wojtkowski *et al.*¹¹ Earlier in this chapter, we demonstrated an SD-OCT system suitable for *in vivo* video-rate ophthalmic imaging.^{3, 4} This system had a sensitivity of 98.4 *dB*, an acquisition rate of 29,300 A-lines per second and an axial resolution of 6 μm in the eye at a safe ocular exposure level of 600 μW . Here we will quantify the dynamic range within a structural intensity image and the axial resolution of an SD-OCT system equipped with an ultra-broadband source and identify previously unseen features in the retina.

One difficulty that arises from using ultra-broadband sources in a fiber-based OCT setup for ophthalmic imaging is chromatic dispersion in optically-dense materials like glass, tissue and water. The speed of light in the material depends on the refractive index $n(k)$, slowing down certain spectral components to a greater extent than others, hence dispersing the light. The total amount of dispersion increases linearly with the length of a dispersing medium, while chromatic dispersion in air is negligible. Considerable amounts of dispersion can be tolerated if the dispersion in the two arms of the interferometer is equal, thus creating a coherence function that will be free of dispersion artifacts. However, when sample and reference arms contain different lengths of optical fiber or other dispersive media, a dispersion mismatch

occurs. In the sample arm, the introduction of an eye with unknown diameter creates a similar effect. The coherence function will not only be broadened by dispersion, but its peak intensity will decrease as well. Second order or group-velocity dispersion can be compensated for by changing the lens-to-grating distance in a rapid scanning optical delay line.²⁸ However, this method does not compensate for higher orders of dispersion. One can completely balance dispersion in an OCT system by inserting blocks of BK7 and fused silica in the delay line.²⁴ The previously-mentioned unknown factor introduced by an unknown eye diameter requires a flexible method for dispersion compensation. An alternative to compensation in hardware is dispersion compensation in software. De Boer *et al.* induced dispersion in the delay line of a TD-OCT system equipped with an AFC source ($\lambda_0 = 1310 \text{ nm}$, $\Delta\lambda = 75 \text{ nm}$), and numerically compensated for dispersion artifacts in structural intensity images obtained from an onion.²⁹ Fercher *et al.* numerically compensated for dispersion induced by a glass sample. Their broadband spectrum was generated by a high-pressure mercury lamp.³⁰ In our analysis we will compensate in software for dispersion induced by an ultra-broadband source and subsequently remove artifacts in structural intensity images obtained from the retina.

The combination of ultrahigh-resolution imaging and high-speed imaging may allow us to identify features in the human retina that have not been seen before. In the near future, this technology may facilitate the application of ultrahigh-resolution systems in the clinic.

4.4.1 Dispersion compensation theory

A dispersion mismatch between sample and reference arms introduces a phase shift $e^{i\theta(k)}$ in the complex cross-spectral density $I(k)$. Since spectrometer data is acquired as a function of wavelength, data has to be transformed to k -space first. The relation between the phase $\theta(k)$ and the multiple orders of dispersion can best be described by a Taylor series expansion:

$$\theta(k) = \theta(k_0) + \left. \frac{\partial\theta(k)}{\partial k} \right|_{k_0} (k_0 - k) + \frac{1}{2} \cdot \left. \frac{\partial^2\theta(k)}{\partial k^2} \right|_{k_0} (k_0 - k)^2 + \dots + \frac{1}{n!} \cdot \left. \frac{\partial^n\theta(k)}{\partial k^n} \right|_{k_0} (k_0 - k)^n \quad \text{Eq. 29}$$

with λ_0 the center wavelength and k_0 equal to $2\pi/\lambda_0$. The first two terms describe a constant offset and group velocity, respectively, and are not related to dispersive broadening. The third term represents second order or group-velocity dispersion. Dispersion mismatch in sample and reference arms is largely compensated by this term, although adjustment of higher order dispersion can be necessary as well, especially when an ultra-broadband source is used. Dispersion can be removed by multiplying the dispersed cross-spectral density function $I(k)$ with a phase term $e^{-i\theta(k)}$. To determine this phase term for dispersion compensation of data obtained in the human eye *in vivo* requires a coherence function obtained from a well-reflecting

reference point in the eye. We found that it is possible to use the center of the fovea for this purpose, because this part of the eye acts as a good reflector. To determine the phase term, after linear interpolation to k -space, the spectrum is Fourier transformed to κ -space, where it is shifted such that the coherence function is centered on the origin. A complex spectrum in k -space is then obtained after an inverse Fourier transformation. The phase term $\theta(k)$ is equal to the arctangent of the imaginary component divided by the real component, and indicates by how much subsequent wave numbers k are out of phase with each other. This function was fit to a polynomial expression of 9th order, yielding a set of coefficients α_{1-9} . Individual spectra obtained from a volunteer were first multiplied with a phase $e^{-i\theta(k)}$ as determined from the last seven polynomial coefficients and then inverse Fourier transformed into A-lines, thus removing dispersion. The first two coefficients can be neglected: α_1 is a constant that does not affect the data, while the second coefficient α_2 induces a constant offset of the data.

4.4.2 Setup

The turn-key ultra-broadband source was a BroadLighter (Superlum, Russia), in which two superluminescent diodes at center wavelengths of approximately 840 nm and 920 nm were combined in one system with a center wavelength of 890 nm , a FWHM bandwidth of over 150 nm and an optical output power of approximately 4.5 mW . Figure 34 shows the source spectrum and a reference arm spectrum that were recorded with a commercial optical spectrum analyzer (OSA). The reference spectrum was also recorded with our high-speed spectrometer (HS-OSA). By comparing the solid and dash-dotted curves of Figure 34, one can see a significant drop in sensitivity of the line scan camera above 850 nm . The plot amplitudes are adjusted so that all three curves fit within the same graph.

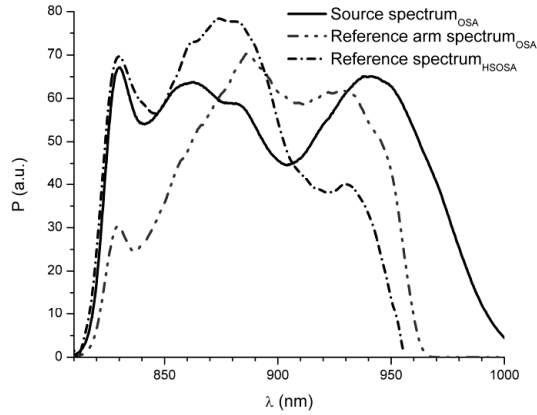


Figure 34. Source spectrum of the BroadLighter (solid line); spectrum returning from the reference arm (dash-dot-dot). Both spectra were measured with a commercial optical spectrum analyzer. The reference spectrum was recorded with our high-speed spectrometer (dash-dot), and by comparing this line with the recording from the commercial OSA it demonstrates the decrease in sensitivity of the line scan camera at wavelengths above 850 nm. Spectral amplitudes were adjusted so that all three curves fit within the same graph.

A detailed description and drawing of the setup can be found in Figure 26, where for these experiments the time-domain detector was omitted. Back reflected light was isolated from the source with a broadband isolator. Without the isolator, back reflections induce noise in the OCT system. After isolation, the power was split with a fiber coupler. The splitting ratio of this coupler was optimized to 80/20 at 830 nm. At longer wavelengths, the splitting ratio approaches 50/50. The manufacturer’s specification (Gould Fiber Optics, Millersville, MD) of wavelength dependent shift in splitting ratio is 0.3% / nm. The larger fraction was sent towards a stationary rapid scanning optical delay line, in which the lens-to-grating distance was optimized to minimize group-delay or second order dispersion. The smaller fraction of the power was sent towards the sample arm, where a slit lamp-based scanner apparatus was available for retinal scanning (Chapter 2). Previously, we used a dichroic coupler in the slit lamp, so that the location of scans could be monitored by a charged coupled device (CCD) camera. In order to reduce the losses in the slit lamp, this dichroic mirror was replaced by a gold mirror. After this replacement, the total attenuation in the slit lamp was 1 dB in single-pass. Longer wavelengths were blocked with a short-pass filter with a cut-off wavelength of 950 nm, since wavelengths above 920 nm do not reach the retina because of absorption in the vitreous. Including this part of the spectrum would not be beneficial, and would decrease the sensitivity performance of the system. The power that was incident on the cornea after low-pass filtering was

equal to $395 \pm 5 \mu W$. This power is well below the allowed maximum for scanning beams as specified by the ANSI standards.¹⁶ Power returning from the eye and the reference arm interfered in the 80/20 fiber coupler. Interference fringes were detected with the high-speed spectrometer, described in section 4.3.1. The galvanometer mirror in the delay line was set in a neutral position and was not driven for these measurements. Since the source bandwidth was larger than the bandwidth of the spectrometer, the spectrum was clipped at one side by offsetting the reference arm mirror such that longer wavelengths were not reflected back into the interferometer. The reference arm power was adjusted with a neutral density filter in the delay line. In the spectrometer, consecutive interference spectra were read out using a custom-made program written in Visual C++. Data was stored on a hard disk. The continuous acquisition rate was 29,300 spectra per second. The integration time per spectrum was equal to $34.1 \mu s$. The duty cycle was 98%, i.e. data was acquired during 98% of the total imaging time.

4.4.3 Measurement procedure

In order to compensate for dispersion, coherence functions were obtained from a reflecting spot in the center of the fovea of a human eye, from a mirror in a water-filled model eye (Eyetechn Ltd.) and from a mirror in air. The sensitivity of the OCT system and the calibration of wavelength-to- k -space mapping were tested with use of a mirror. The slit lamp setup was not used for this particular measurement. Instead, a collimator, a focusing lens and a mirror on a translation stage were used. In order to extrapolate the results to the slit lamp experiments where longer wavelengths are absorbed by the vitreous, a low pass filter ($\lambda_{cut-off} = 950 \text{ nm}$) was inserted in the beam path. The sample arm power could be attenuated with a variable neutral density filter. To verify that the system was free from any depth-dependent dispersion induced by the spectrometer, the reference arm length was changed and measurements were taken at different positions. The depth-dependent attenuation was measured as well. In order to determine whether the system was shot-noise-limited, the variance of 1000 reference arm spectra was determined, and fit with a theoretical expression for the shot noise.⁴

In vivo measurements were performed on the undilated right eye of a healthy volunteer. The right eye was stabilized using an external fixation spot for the volunteer's contralateral eye. Multiple sets of B-scans were taken in the macular area at an acquisition rate of 29,300 spectra per second. During acquisition, a refresh rate on screen of three frames per second was maintained without dispersion compensation. For each frame, the fast axis of the retinal scanner was deflected once, while the slow axis of the scanner could be stepped between frames. B-scans that contained specular reflections from the surface of the fovea were analyzed in detail to compensate for dispersion.

4.4.4 Analysis

Data was analyzed after acquisition with a custom-made program written in Matlab. Raw data was processed in several steps to extract structural intensity images^{3, 4, 19} as well as Doppler flow data.³¹ In addition, we compensated for dispersion using a phase $e^{-i\theta(k)}$, built with a set of polynomial coefficients α_{3-9} obtained from a specular reflection in the human retina. For the coherence length determination, the density of points within each A-line was increased eightfold by zero-padding the spectral data.¹⁹ For all data obtained from a mirror, we averaged over 100 A-lines to reduce the influence of noise. The dispersion analysis in software, which required input from the operator, took approximately five minutes in Matlab. To improve sensitivity, two consecutive spectra were summed before Fourier transformation, and provided the two spectra were more or less identical, and did not have a substantial difference in phase, the summation of the two spectra yielded a signal that was twice as high. For such a summation it was crucial that the two spectra were recorded at the same location. Since our beam spot diameter at the retina was approximately 20-30 μm , and the scan was approximately 3.1 mm long, containing 1000 samples, the distance between the locations of two neighboring spectra (3 μm) was substantially smaller than the spot size. From data recorded at 7.5 kHz we found that the system was very stable, and that phase instabilities occurred at a much lower frequency. The summation of two spectra acquired at 29,200 Hz therefore yielded a signal that was twice as high.

At an effective A-line rate of 14,600 per second and an effective integration time of 68 μs per spectrum, images containing 500 A-lines each with a length of 1024 pixels were created.

4.4.5 Dispersion compensation

In the graph of Figure 35, the phase term $\theta(k)$ obtained from a mirror in a model eye (averaged over 100 A-lines) and from a specular reflective spot in the fovea (averaged over 5 A-lines) are shown. The differences between the measured phase terms and polynomial fits (9th order) to the data are shown as well, with the corresponding axis on the right. The inclusion of more than 9 coefficients in the polynomial fit did not significantly improve the resulting coherence function. Both phases show the same pattern, which indicates that both the model eye and the real eye experience similar amounts of dispersion. All *in vivo* data was compensated using the phase that was obtained from the specular reflection of the fovea itself (thin solid curve of Figure 35).

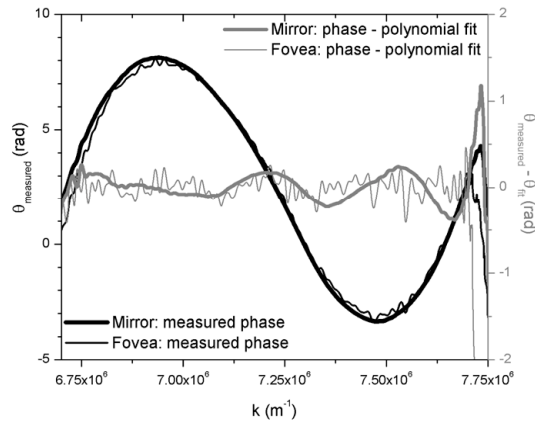


Figure 35: The phase $\theta(k)$ obtained from a mirror in a model eye and from a specular reflection in the fovea (left axis). The residual dispersion not compensated for by the polynomial fit is given as a function of k (right axis).

In the graph of Figure 36, the coherence function obtained from a mirror in air is plotted. The data shows the amplitude as a function of depth, where the amplitude is given by the absolute value of the Fourier components after transform of the measured spectrum. In the same graph, a coherence function compensated for dispersion is plotted. For this plot, the same technique as applied in Figure 35 was used, yielding a different set of coefficients, since in this case the mirror was not located in the water-filled model eye.

The dispersion compensation technique gives a significant reduction in coherence length as well as a threefold increase in peak height. Without dispersion compensation, the coherence length was $27.0 \mu\text{m}$. After dispersion compensation it was estimated to be $4.0 \mu\text{m}$ ($n = 1$), equivalent to $2.9 \mu\text{m}$ in tissue with a refractive index of $n = 1.38$. After dispersion compensation, side lobes are present at both sides of the coherence function. These side lobes are a result of the non-Gaussian shaped reference arm spectrum (Figure 34).

In Figure 37, coherence functions obtained from a mirror in air at different path length differences are plotted. The coherence function plotted with a solid line was dispersion compensated, using the previously mentioned dispersion compensation technique. This process yielded a dispersion compensation phase $e^{i\theta(k)}$. All other data sets were multiplied with the same phase before Fourier transformation. Coherence functions from different depths were overlapped for comparison. The point density of all curves was increased by a factor of 8, using zero padding. The coherence length for path length differences up to $1200 \mu\text{m}$ was $4.0 \mu\text{m}$ in air. At $z = 1700 \mu\text{m}$, the

coherence length increased to $4.1 \mu\text{m}$ and at $z = 2200 \mu\text{m}$ it further increased to $4.3 \mu\text{m}$. This increase can be attributed to the finite width of the pixels, as well as the Gaussian distribution of the focused beam, as discussed earlier in section 4.3.3.

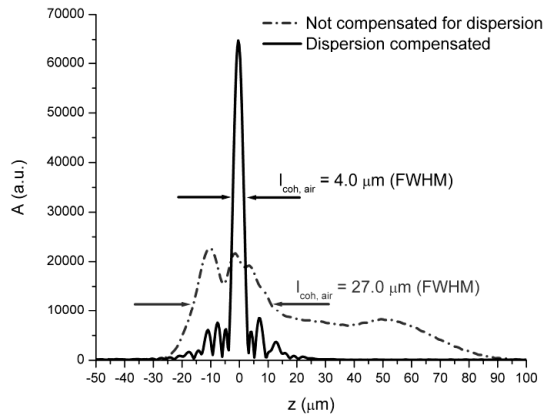


Figure 36. Coherence function obtained from a mirror in air. Uncompensated data (dash-dot) is compared with a coherence function after dispersion compensation (solid). The density of points was increased in both cases by a factor of 8 using a zero-padding technique.

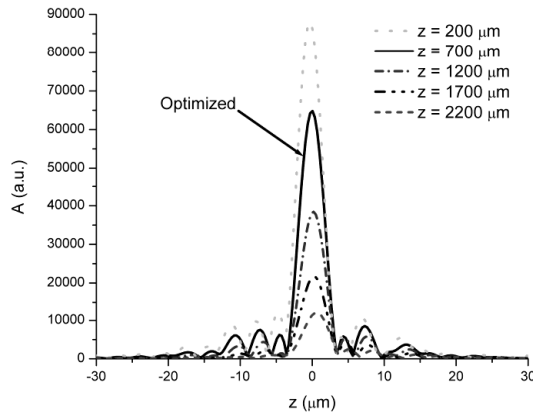


Figure 37. Coherence functions obtained from a mirror at different path length differences z . The coherence function at $z = 700 \mu\text{m}$ was dispersion compensated, and the data of all other curves was multiplied with the same phase $e^{-i\theta(k)}$ before Fourier transformation. The coherence length for path length differences up to $1200 \mu\text{m}$ was $4.0 \mu\text{m}$ in air, $4.1 \mu\text{m}$ for $z = 1700 \mu\text{m}$ and $4.3 \mu\text{m}$ for $z = 2200 \mu\text{m}$.

The depth-dependent attenuation was also calculated from Figure 37,⁴ by comparing peaks at $z = 200$ and $1200 \mu\text{m}$ and found to be equal to 7.2 dB over this image. Compared to the results obtained with an ordinary broadband source, as shown earlier in Figure 30, this result is very similar. With the SLD in the source arm, a depth-dependent attenuation of approximately 7.5 dB was calculated, comparing peaks at $z = 250$ and $1250 \mu\text{m}$.

4.4.6 Noise performance

An analysis on 1000 reference spectra demonstrated that the system was shot-noise-limited, using the same method and well depth value as described earlier in section 4.3.2. We found that without an isolator, the system was not shot-noise-limited. The isolator effectively suppressed optical feedback to the source, therefore all other measurements were performed with an isolator in the source arm.

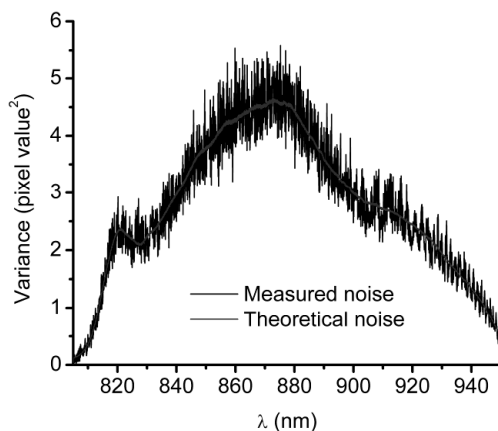


Figure 38. Shot noise measurement using the BroadLighter in an SD-OCT configuration. The shot noise level was determined with illumination of the reference arm only. The measured shot noise curve was fit with a theoretical expression for the shot noise, demonstrating that the system was shot-noise-limited. A color image can be found on page 122.

4.4.7 Sensitivity measurements

The maximum power after the sample arm fiber collimator was $533 \mu\text{W}$. Using a mirror in the sample arm, $101 \mu\text{W}$ returned to the detector arm. After attenuation with a 30.8 dB neutral density filter in the sample arm, 83.7 nW was measured at the detection arm, and a signal-to-noise ratio (SNR) of 58.0 dB was measured at an acquisition rate of 29,300 spectra per second (see coherence function at $z = 700 \mu\text{m}$). In theory, a detected power of 83.7 nW with our previously reported spectrometer efficiency of 28% should give an SNR of 65.6 dB .⁴ Comparing this value with the

measured value of 58.0 *dB*, the spectrometer performed 7.6 *dB* below the theoretical SNR. This reduction was attributed to a reduced quantum efficiency of the detector for longer wavelengths.

For a measured sample arm power of 400 μW after the slit lamp, a return loss through the slit lamp of 1 *dB* and a 3 *dB* sensitivity gain by coherent addition of two consecutive spectra, the system sensitivity was determined to be 89.6 *dB* at a 14,600 A-lines/*s* acquisition rate.

4.4.8 *In vivo* measurements on a human volunteer

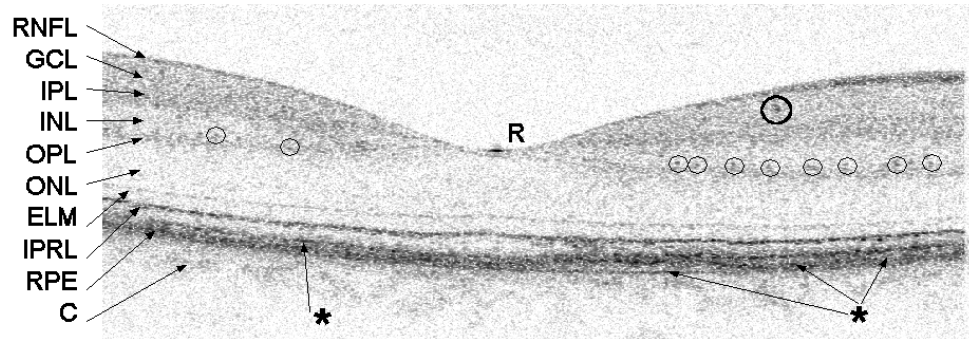


Figure 39. Structural image of the fovea. The dimensions of the image are 3.1 x 0.61 *mm*. The image is expanded in the vertical direction by a factor of 2 for clarity. Layers are labeled as follows: RNFL – retinal nerve fiber layer; GCL – ganglion cell layer; IPL – inner plexiform layer; INL – inner nuclear layer; OPL – outer plexiform layer; ONL – outer nuclear layer; ELM – external limiting membrane; IPRL – interface between the inner and outer segments of the photoreceptor layer; RPE – retinal pigmented epithelium; C – choriocapillaris and choroid. A highly reflective spot in the center of the fovea is marked with an R. A blood vessel is marked with a large circle and structures in the outer plexiform layer are marked with smaller circles. Two layers at the location of the RPE at the left and right are marked with arrows and an asterisk (*).

The image shown in Figure 39 was recorded in the fovea at an acquisition rate of 29.3 frames per second with 500 A-lines per frame. The image is expanded in vertical direction by a factor of 2. A movie made at the same location can be seen online.⁵ The dimensions of the image are 3.1 x 0.61 *mm*. The maximum dynamic range within the image was equal to approximately 35 *dB*. Several layers can be recognized in this image.²¹ The upper dark band at the left and right of the image is the retinal nerve fiber layer that becomes thicker further away from the fovea. Below this layer, we see two dark bands delineated by two whiter bands. The upper dark band consists of the ganglion cell layer and the inner plexiform layer. The two white bands are the inner and outer nuclear layers, and the second dark band is the outer plexiform layer. The first dark layer below the outer nuclear layer is the external limiting membrane, which

extends over the whole width of the image. This layer is in general not visible with OCT using an ordinary broadband source. Below this membrane we can see the interface between the inner and outer segments of the photoreceptor layer, which rises directly below the center of the fovea. The lowest layer comprises the retinal-pigmented epithelium (RPE). At the left and right side of the image at the location of the RPE, two layers seem to be present. We hypothesize that one of these layers might be Bruch's membrane. Below the RPE, a cloudy structure can be seen. This structure is the choriocapillaris and the choroid. The fast acquisition rate reveals the true topography of the retina. The coherence length was determined *in vivo* from the specular reflection in the center of the fovea, averaged over 5 A-lines. This coherence function is plot in Figure 40, and the coherence length after dispersion compensation was equal to $4.8 \mu\text{m}$ in air and $3.5 \mu\text{m}$ in tissue ($n = 1.38$). Compared to the coherence length displayed in Figure 36, using the same index of refraction of 1.38, the coherence function is broadened. Due to absorption of longer wavelengths in the vitreous, the effective bandwidth is reduced, yielding a longer coherence length.

Small highly-reflecting black dots can be seen in the ganglion cell layer and in both plexiform layers. We conclude that they are not caused by speckle, because they consistently appeared at the same location over consecutive movie frames.⁵ The dots seem to be almost regularly spaced in the outer plexiform layer. We believe that these black dots are very small blood vessels. Snodderly *et al.* measured the distribution of blood vessels in an enucleated macaque eye by means of microscopy in frozen samples.³² They report a very similar spacing of small blood vessels in the plexiform layers near the fovea. To positively identify these structures as blood vessels, we analyzed the data for blood flow as described in our earlier work.³¹ Doppler flow analysis confirmed that flow occurs in the darker dots located in the ganglion cell layer, which therefore can be positively identified as blood vessels. In the plexiform layers, a clear correlation between location of the highly reflective black dots and Doppler flow could not be found. Flow was only detected incidentally in these layers at locations where black dots were seen. One explanation for the fact that no consistent flow was detected in the well-reflecting features in the plexiform layers is that these features are not blood vessels. Another explanation may be that our system is not sensitive enough to measure flow in such small vessels. For instance, the blood vessels may be too small, which reduces the number of A-lines and therefore the signal that can be used to determine the presence of blood flow. Furthermore, the analysis depends on measuring a Doppler component parallel to the direction of the beam. If the blood vessel is exactly perpendicular to the beam direction, a parallel Doppler flow component will be absent and no flow can be registered. In previous work, larger blood vessels were recognized by their white appearance and the shadow they cast, caused by light attenuation in the blood. Here blood vessels act as good scatterers, presumably due to their small sizes.

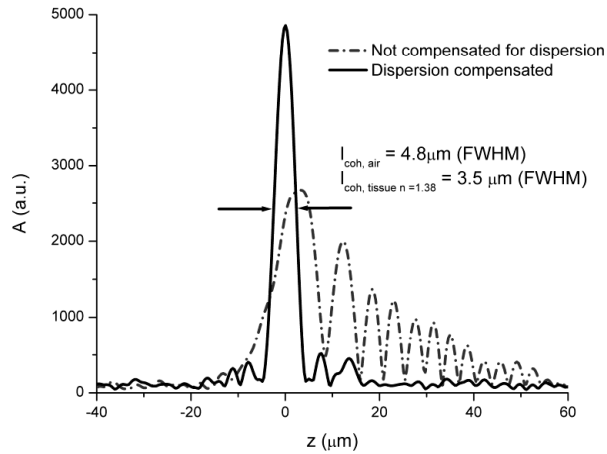


Figure 40. Coherence function obtained from a reflective spot in the fovea. Dispersion compensated, the coherence length is equal to $4.8 \mu\text{m}$ in air.

By running the slow axis of the retinal scanner, subsequent cross-sections of the fovea were made. The image in Figure 41 measures 6.2 by 1.2 mm and the slow axis scans over 3.1 mm . During processing, noise was filtered with a 2 by 2 median filter to match the data better to the pixel resolution of this image. A movie made at the same location can be found online.⁵

The reflecting spot in the center of the fovea, as seen in the Figure 39, only showed up in a couple of movie frames,⁵ indicating that the specular reflection only occurs in the three-dimensional center of the fovea. The horizontal lines at the top of the image are residual fixed pattern noise.

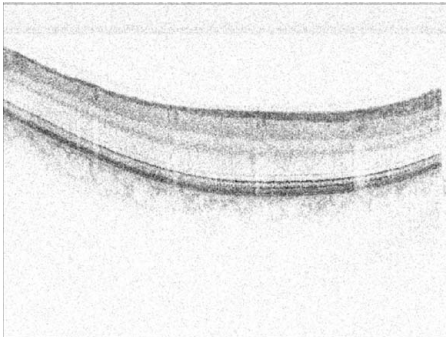


Figure 41. Structural intensity image of the fovea. The dimensions of the image are $6.2 \times 1.2 \text{ mm}$.

In this study, the performance of an SD-OCT system equipped with an ultra-broadband source was determined by measuring the SNR and the coherence length on a mirror and in the eye. Comparing the measured SNR value of 89.6 *dB* with the theoretical value of 97.2 *dB*, our system performs 7.6 *dB* below the theoretical limit. In our previous system described in section 4.3, the difference between the measured and theoretical SNR was 2.2 *dB*.⁴ The extra loss of 5.4 *dB* that we encounter in this system equipped with the BroadLighter can be attributed to the lower sensitivity of the line scan camera. In Figure 34, the reference arm spectrum recorded with a commercial optical spectrum analyzer is compared with the same spectrum recorded with our high-speed spectrometer. The sensitivity of our line scan camera drops by at least a factor of two for wavelengths above 850 *nm*.

In a conventional HR-OCT system, the highest documented A-line rate is equal to 250 A-lines per second. The power incident on the cornea was equal to 500-800 μW , resulting in a sensitivity of 95 *dB*. The A-line length was equal to 1-2.8 *mm*.²¹ The effective A-line rate of our SD-OCT system was 14,800 A-lines per second, and the measured sensitivity was 89.6 *dB*, with a power of $395 \pm 5 \mu\text{W}$ incident on the cornea. Comparing the two systems, the spectral-domain OCT system was 59 times faster at a 5.4 *dB* lower sensitivity.

4.5 Conclusion

We theoretically and experimentally demonstrated a sensitivity improvement of SD-OCT over TD-OCT by a factor of 148 (21.7 *dB*) and ultrahigh-speed *in vivo* human retinal OCT imaging at 29,300 depth profiles per second, resulting in cross-sectional imaging at video rate with 6 μm axial resolution. At these speeds, realignment of depth profiles becomes obsolete, revealing the true topography of retina. Motion artifacts, commonly present in both research and commercial ophthalmic OCT systems are greatly reduced, thus minimizing the image distortion caused by involuntary eye movement. The demonstrated speed improvement allows for a shift from two-dimensional sampling to comprehensive three-dimensional screening of ocular pathology with OCT.

The axial resolution of a TD-OCT system increases with source spectral bandwidth, but its SNR is inversely proportional to an increase in detection bandwidth. Since source bandwidth does not affect the SNR performance of a SD-OCT configuration, SD-OCT is preferred for ultrahigh-resolution ophthalmic imaging. However, ultra-broadband sources induce more dispersion than standard broadband sources. With dispersion compensation in software, we managed to reduce dispersion artifacts significantly. After dispersion compensation, the coherence length measured from a mirror in air was equal to 4.0 μm ($n = 1$). The dispersion-compensated axial resolution obtained from a reflecting spot in the fovea was equal to

3.5 μm ($n = 1.38$). To our knowledge, this is the first coherence length measurement in the human eye *in vivo*. The combination of high axial resolution measurements at a high data acquisition rate allows us to identify features that have not been seen in the human retina before with OCT. Movies at 29.3 frames per second with 500 A-lines per frame seem to indicate two layers at the location of the RPE, as well as small structures previously unseen in the two plexiform layers, which are believed from their location to be blood vessels. Comparing the performance of our ultrahigh-resolution SD-OCT system with a conventional high-resolution time-domain OCT system, the A-line rate of the spectral-domain OCT system was 59 times higher at a 5.4 dB lower sensitivity.

References

1. H.A. Quigley, E.M. Addicks and W.R. Green, "Optic nerve damage in human glaucoma. III. Quantitative correlation of nerve fiber loss and visual field defect in glaucoma, ischemic neuropathy, papilledema, and toxic neuropathy," *Archives of Ophthalmology*, 100, 135-46 (1982).
2. J.F. de Boer, B. Cense, B.H. Park, et al., "Improved signal-to-noise ratio in spectral-domain compared with time-domain optical coherence tomography," *Optics Letters*, 28, 2067-2069 (2003).
3. N. Nassif, B. Cense, B.H. Park, et al., "In vivo human retinal imaging by ultrahigh-speed spectral domain optical coherence tomography," *Optics Letters*, 29, 480-482 (2004).
4. N.A. Nassif, B. Cense, B.H. Park, et al., "In vivo high-resolution video-rate spectral-domain optical coherence tomography of the human retina and optic nerve," *Optics Express*, 12, 367-376 (2004).
5. B. Cense, N.A. Nassif, T.C. Chen, et al., "Ultrahigh-resolution high-speed retinal imaging using spectral-domain optical coherence tomography," *Optics Express*, 12, 2435-2447 (2004).
6. W.V. Sorin and D.M. Baney, "A Simple Intensity Noise-Reduction Technique for Optical Low-Coherence Reflectometry," *Ieee Photonics Technology Letters*, 4, 1404-1406 (1992).
7. B.M. Hoeling, A.D. Fernandez, R.C. Haskell, et al., "An optical coherence microscope for 3-dimensional imaging in developmental biology," *Optics Express*, 6, 136-146 (2000).
8. L. Mandel and E. Wolf, "Measures of Bandwidth and Coherence Time in Optics," *Proceedings of the Physical Society of London*, 80, 894-897 (1962).
9. A.F. Fercher, C.K. Hitzenberger, G. Kamp and S.Y. Elzaiat, "Measurement of Intraocular Distances by Backscattering Spectral Interferometry," *Optics Communications*, 117, 43-48 (1995).
10. G. Hausler and M.W. Lindner, "Coherence Radar and Spectral Radar - new tools for dermatological diagnosis," *Journal of Biomedical Optics*, 3, 21-31 (1998).
11. M. Wojtkowski, R. Leitgeb, A. Kowalczyk, T. Bajraszewski and A.F. Fercher, "In vivo human retinal imaging by Fourier domain optical coherence tomography," *Journal of Biomedical Optics*, 7, 457-463 (2002).
12. T. Mitsui, "Dynamic range of optical reflectometry with spectral interferometry," *Japanese Journal of Applied Physics Part 1-Regular Papers Short Notes & Review Papers*, 38, 6133-6137 (1999).
13. R. Leitgeb, C.K. Hitzenberger and A.F. Fercher, "Performance of fourier domain vs. time domain optical coherence tomography," *Optics Express*, 11, 889-894 (2003).
14. B. Cense, T.C. Chen, B.H. Park, M.C. Pierce and J.F. de Boer, "In vivo birefringence and thickness measurements of the human retinal nerve fiber layer using polarization-sensitive optical coherence tomography," *Journal of Biomedical Optics*, 9, 121-125 (2004).
15. R. Waterbury, *Ocean Optics*, Telephone conversation and e-mail follow-up, June 2004.
16. A.N.S.I., *Safe use of lasers*. 1993, Laser Institute of America: New York.

17. M.A. Choma, M.V. Sarunic, C.H. Yang and J.A. Izatt, "Sensitivity advantage of swept source and Fourier domain optical coherence tomography," *Optics Express*, 11, 2183-2189 (2003).
18. C. Dorrer, N. Belabas, J.P. Likforman and M. Joffre, "Spectral resolution and sampling issues in Fourier-transform spectral interferometry," *Journal of the Optical Society of America B-Optical Physics*, 17, 1795-1802 (2000).
19. S.H. Yun, G.J. Tearney, B.E. Bouma, B.H. Park and J.F. de Boer, "High-speed spectral-domain optical coherence tomography at 1.3 μ m wavelength," *Optics Express*, 11, 3598-3604 (2003).
20. R. Tripathi, N. Nassif, J.S. Nelson, B.H. Park and J.F. de Boer, "Spectral shaping for non-Gaussian source spectra in optical coherence tomography," *Optics Letters*, 27, 406-408 (2002).
21. W. Drexler, H. Sattmann, B. Hermann, et al., "Enhanced visualization of macular pathology with the use of ultrahigh-resolution optical coherence tomography," *Archives of Ophthalmology*, 121, 695-706 (2003).
22. F.W. Campbell and D.G. Green, "Optical and Retinal Factors Affecting Visual Resolution," *Journal of Physiology-London*, 181, 576-593 (1965).
23. E.A. Swanson, D. Huang, M.R. Hee, et al., "High-Speed Optical Coherence Domain Reflectometry," *Optics Letters*, 17, 151-153 (1992).
24. W. Drexler, U. Morgner, F.X. Kartner, et al., "In vivo ultrahigh-resolution optical coherence tomography," *Optics Letters*, 24, 1221-1223 (1999).
25. W. Drexler, U. Morgner, R.K. Ghanta, et al., "Ultrahigh-resolution ophthalmic optical coherence tomography," *Nature Medicine*, 7, 502-507 (2001).
26. C.K. Hitzenberger, P. Trost, P.W. Lo and Q.Y. Zhou, "Three-dimensional imaging of the human retina by high-speed optical coherence tomography," *Optics Express*, 11, 2753-2761 (2003).
27. B. Cense, T.C. Chen, B.H. Park, M.C. Pierce and J.F. de Boer, "In vivo depth-resolved birefringence measurements of the human retinal nerve fiber layer by polarization-sensitive optical coherence tomography," *Optics Letters*, 27, 1610-1612 (2002).
28. G.J. Tearney, B.E. Bouma and J.G. Fujimoto, "High-speed phase- and group-delay scanning with a grating-based phase control delay line," *Optics Letters*, 22, 1811-1813 (1997).
29. J.F. de Boer, C.E. Saxer and J.S. Nelson, "Stable carrier generation and phase-resolved digital data processing in optical coherence tomography," *Applied Optics*, 40, (2001).
30. A.F. Fercher, C.K. Hitzenberger, M. Sticker, et al., "Dispersion compensation for optical coherence tomography depth- scan signals by a numerical technique," *Optics Communications*, 204, 67-74 (2002).
31. B.R. White, M.C. Pierce, N. Nassif, et al., "In vivo dynamic human retinal blood flow imaging using ultra-high-speed spectral domain optical Doppler tomography," *Optics Express*, 11, 3490-3497 (2004).
32. D.M. Snodderly, R.S. Weinhaus and J.C. Choi, "Neural Vascular Relationships in Central Retina of Macaque Monkeys (*Macaca-Fascicularis*)," *Journal of Neuroscience*, 12, 1169-1193 (1992).

5. Polarization-sensitive spectral-domain optical coherence tomography

Abstract

Combining spectral-domain OCT and polarization-sensitive OCT, polarization data with a dynamic range of approximately 35 dB was obtained from the retina of a glaucoma patient. The time required for a measurement of 12 concentric circular scans was 1.6 seconds, which is 45 times faster than time-domain PS-OCT measurements with a lower signal-to-noise ratio. Similar measurements on a healthy volunteer with spectral-domain polarization-sensitive OCT yielded images with a dynamic range of approximately 40 dB. Three-dimensional volume data was reduced to a single two-dimensional image, which resembles a fundus image.

Measurements on a healthy volunteer gave results that were similar to those that were previously obtained with the slower time-domain polarization-sensitive OCT system. Measurements on one glaucoma patient did not give a satisfying conclusion, regarding whether the birefringence of the glaucomatous retina is affected or not. Measurements on more patients have to be made to determine the effects of glaucoma on the retinal nerve fiber layer.

5.1 Introduction

Age is an important risk factor for the development of glaucoma. In general, glaucoma patients tend to be older and with progressing age the chance of developing cataracts and myopia increases. In Chapter 3 we compared the image quality and polarization-sensitive results obtained in healthy volunteers with those of glaucoma patients. The lower signal-to-noise ratio in images obtained from glaucoma patients was identified as the cause of unreliable results. Furthermore, from the analyzed RNFL thickness and double-pass phase retardation per unit depth (DPPR/UD) data obtained from a healthy subject, we concluded that a retinal nerve fiber layer (RNFL) thickness of more than $75 \mu\text{m}$ was required for a reliable birefringence measurement. Since most of the measured glaucomatous nerve fiber layer thickness was below this limit, no complete glaucomatous data set could be retrieved. We hypothesized that data from these layers acquired at a higher signal-to-noise ratio would make the data analysis more reliable. Also, the long acquisition time of 6 seconds per scan and 72 seconds for a complete data set resulted in unreliable data due to involuntary eye motion and data loss caused by frequent blinking.

A combination of spectral-domain OCT and polarization-sensitive OCT combines ultra-high-speed acquisition or high sensitivity with polarization-sensitivity. This new combination could improve the reliability of measurements obtained from glaucoma patients.

Yasuno *et al.* reported measurements on human skin *in vitro* and porcine esophagus *in vitro* using a spectrometer-based Fourier-domain system.^{1, 2} In both publications, Yasuno *et al.* failed to mention their A-line rate. Recently, Zhang *et al.* reported measurements on rabbit tendon *in vitro* using a polarization-sensitive optical frequency-domain imaging (OFDI) system.³ The A-line rate of their system was 250 Hz, which was not an improvement compared to classic time-domain PS-OCT systems. Independent of the A-line rate, the two main advantages of spectral-domain OCT over time-domain OCT, which are a higher sensitivity and higher acquisition rate, both necessary for *in vivo* measurements, were not demonstrated by either group of authors. Here we will demonstrate both advantages, and use them to measure the thickness and DPPR/UD of the retinal nerve fiber layer of a glaucoma patient *in vivo*.

5.2 Measurement Method

5.2.1 Setup

A spectral-domain optical coherence tomography system (as described in Chapter 4) was made polarization-sensitive by adding a polarization modulator in the source arm and a polarizing beam splitter (CVI) combined with an extra line scan

camera (Basler, 2048 elements of 10 by 10 μm , maximum line frequency 29,300 Hz) in the detection arm.

A high-power superluminescent diode (SLD-371-HP, Superlum, $\lambda_0 = 840 \text{ nm}$, $\Delta\lambda_{FWHM} = 50 \text{ nm}$) was isolated by means of a broadband isolator (OFR), and at the output of the isolator the light was linearly polarized. A Pentium PC with dual Intel Xeon processors and with National Instrument I/O boards generated the driving waveform for the polarization modulator, which was positioned directly after the isolator. The waveform was amplified with a high voltage amplifier and sent to the modulator. The waveform consisted of a block wave with a maximum frequency of 29,300 Hz , creating two different polarization states behind the polarization modulator that were 90° separate on the Poincaré sphere. The modulation frequency could be slowed down arbitrarily, to increase the measurement sensitivity as desired. The integration time of the line scan cameras could be increased accordingly, with a slower scan speed as a penalty. The polarization modulator was synchronized with two line scan cameras in the detection arm, such that alternate A-lines were acquired with two different input polarization states. Data was only acquired when the polarization state was constant and polarization instabilities due to switching of the polarization modulator were not recorded by shortening the acquisition time of the two cameras to 33 μs . Each B-scan or frame was synchronized with the fast scanning axis of the slit lamp apparatus, which was described in Chapter 2.

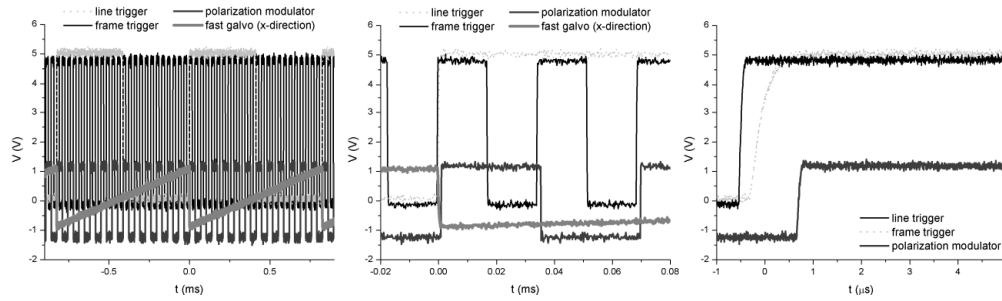


Figure 42: Synchronized trigger waveforms for the line scan cameras (line trigger, frame trigger) and driving waveforms for the polarization modulator and fast galvanometer. From left to right, graphs are shown at a shortened time scale. For clarity, only 20 spectra were grabbed per scan. In reality, 1000 spectra were recorded per cycle of the fast galvanometer. A time delay between the starting points of the different waveforms (right plot) was created to compensate for delays in the line scan cameras and the polarization modulator.

In the example of Figure 42, the trigger and driving waveforms are shown for a configuration where only 20 A-lines were acquired for one image. The driving waveform for the fast galvanometer increased linearly and started simultaneously with the frame trigger waveform. Within this frame, 20 pulses were generated to trigger

both line scan cameras for the acquisition of 20 spectra. This also happened at every up flank. Since there was an internal delay in the camera of $2 \mu\text{s}$, and a $1 \mu\text{s}$ delay in the polarization modulator, the polarization modulator signal was delayed in software by approximately $1 \mu\text{s}$.

An 80/20 fiber coupler sent 80% of the power to the reference arm. Here, a rapid scanning delay line (RSOD) was equipped with a polarizing beam splitter, ensuring transmission of equal amounts of power through the delay line for both input polarization states. The RSOD was mainly used for dispersion compensation and the galvanometer mirror was kept stationary for these measurements. Light returning from the RSOD interfered with light returning from the sample arm where a slit lamp was used to image the retina. Interference spectra were recorded with the polarization-sensitive spectrometer in the detection arm, where two line scan cameras were positioned around a polarizing beam splitter. Light was first collimated and diffracted with a transmission grating, after which it was focused by means of a three-element air-spaced lens. A polarizing beam splitter directed orthogonal states to the two line scan cameras, which were mounted on three-axis translation stages (New Focus).

A polarization state that is transmitted straight through a polarizing beam splitter is in general pure, i.e. approximately 99% of the power is horizontally polarized. The polarization state that is reflected at 90° by a polarizing beam splitter is usually less pure, with horizontally polarized light mixing with vertically polarized light. Since such contamination distorts a proper polarization analysis, the horizontally polarized light was filtered from the reflected polarization state using a second polarizer. We used a Polarcor wire grid polarizer with an extinction ratio of 1: 10,000 and a transmission performance of better than 90% over the full bandwidth. It was positioned in front of the off-axis line scan camera. The transmitted wavefront distortion of this polarizer was specified as less than a quarter wavelength (at 632.8 nm). Spectra were recorded simultaneously with the two line scan cameras and stored to hard disk. In real time, an on-screen frame rate of approximately three frames per second was maintained. The polarization state in all arms of the interferometer was optimized using polarization controllers.

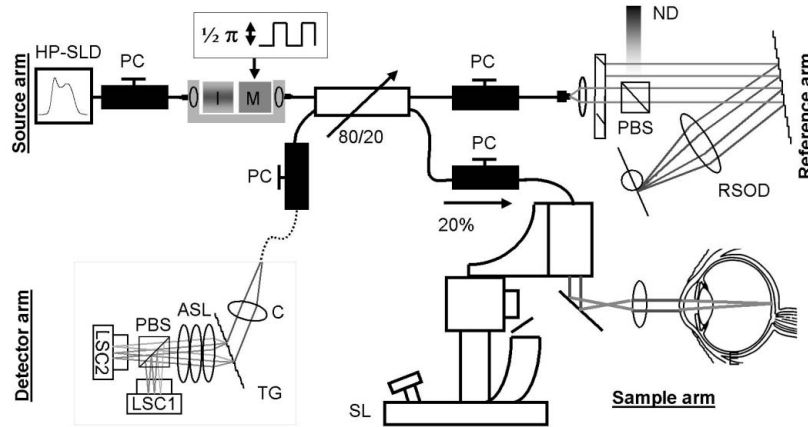


Figure 43: Measurement setup for polarization-sensitive spectral-domain optical coherence tomography. Light from a broadband source (HP-SLD) was coupled through an isolator (I) and modulated at 29,300 Hz with a bulk polarization modulator (M). An 80/20 fiber coupler distributed the modulated light over sample and reference arms. The retina was scanned with a slit lamp (SL) based retinal scanner, and the reference arm consisted of a rapid scanning delay line (RSOD), employed with a polarizing beam splitter (PBS) to ensure equal transmission for both polarization states, and a variable neutral density filter (ND) for attenuation. On the return path, interference fringes were detected with a high-speed polarization-sensitive spectrometer. Light was collimated ($C - f = 60 \text{ mm}$) and diffracted with a transmission grating (TG, 1200 lines / mm) after which a three-element air-spaced lens (ASL - $f = 100 \text{ mm}$) focused the spectra on two line scan cameras (LSC1 and 2). A polarizing beam splitter in the detection path directed orthogonal polarization components to the two cameras, which were synchronized with each other and with the polarization modulator in the source arm. A clean-up polarizer was positioned in front of LSC1 to remove the contaminating polarization state. Polarization controllers (PC) were used to fine-tune the polarization state of the light.

The system that was described earlier in Chapter 3 simultaneously acquired OCT data and video images. As can be seen in Figure 43, the PS-SD-OCT system was equipped with a CCD camera as well and it was used for the positioning of the scans around the optic nerve head. These camera images were not stored to hard disk.

Prior to and during data acquisition, information from the CCD camera and the real-time OCT structural intensity display were used to aim the scanning beam through the center of the pupil and to position the scans around the optic nerve head. Furthermore, both imaging modalities were used to focus the beam onto the retina, guaranteeing data with the highest possible signal-to-noise ratio.

5.2.2 Alignment of the polarization-sensitive system

The data that is acquired with a spectral-domain system has to be mapped correctly to k -space to avoid artifacts in A-lines (Chapter 4). In polarization-sensitive spectral-domain OCT, a difference in k -space mapping between data acquired with the two cameras generates a difference in amplitude and phase in A-lines. For instance, a scattering event in an A-line taken with one of the two cameras will be located at a certain depth, while the same event is located at a slightly higher or lower depth in the data set taken with the other camera due to incorrect k -space mapping. These small differences, which may be smaller than a coherence length, induce non-existent birefringence artifacts in the phase retardation data.

Several measures were taken to avoid these artifacts. Prior to data acquisition, the reference arm signal was maximized on both cameras. To align the two cameras with each other, a non-birefringent scattering sample such as a stack of microscope cover slips was measured in real-time with the polarization-sensitive system. The location of one camera was shifted perpendicular to the beam until the birefringence in the sample, as measured with the system, was negligible.

For each of the two cameras, a set of parameters was determined for the mapping and dispersion compensation procedure as described in Chapter 4. Using a mirror in a water-filled model eye, spectra were obtained with both line scan cameras simultaneously at different path length differences.

5.2.3 Measurement procedure on subjects

All experiments were performed under a protocol that adhered to the tenets of the Declaration of Helsinki and was approved by the Institutional Review Boards of both the Massachusetts Eye and Ear Infirmary and Massachusetts General Hospital. For this study, one healthy volunteer and seven glaucoma patients were enrolled. Patients with various stages of open angle glaucoma (primary, pigmentary, and pseudoexfoliation forms) were recruited from the glaucoma practice of Teresa Chen, M.D. at the Massachusetts Eye and Ear Infirmary. Medical records were used to determine if patients were eligible for the study. After giving informed consent, the eligible eyes of the glaucoma patients were dilated with phenylephrine hydrochloride 5.0% and tropicamide 0.8%. Measurements were performed on all enrolled subjects.

Healthy volunteer

For comparison, the healthy volunteer was previously imaged with both the polarization-sensitive time-domain system,^{4,6} as well as the spectral-domain system.⁷⁻⁹ For this experiment, the power of the light incident on the volunteer's undilated right eye was equal to 470 μW . Two different types of scans were made around the optic nerve head. One data set was made with concentric circular scans (12 circular scans of 1000 A-lines equidistantly spaced between 1.5 and 2.6 mm), the other data set was

made with 250 linear scans of 500 A-lines covering an area of $6.4 \times 6.4 \text{ mm}$. Data was acquired at integration times of either $33 \mu\text{s}$ or $132 \mu\text{s}$ per A-line. For the last set, the system was slowed down by a factor of 4, improving the sensitivity by a factor of 4. This setting was still almost 45 times faster than the time-domain measurement, reducing the total measurement time for 12 circular scans from 72 seconds to 1.6 s. The eye that was under investigation was stabilized with a fixation spot.

Glaucoma patients

The power incident on the eye was $< 500 \mu\text{W}$ for all glaucoma patients. In cases where the patient could only see with one eye, the eye without vision was imaged. Eyes that were imaged were stabilized with the internal fixation light of the slit lamp system. An external fixation light was used for the contralateral eye of patients who could not see this light. Circular scans of 1000 A-lines with integration times of 33 and $132 \mu\text{s}$ were made. In addition, some eyes were imaged with an integration time of $330 \mu\text{s}$. Finally, linear scans (200 scans of 1000 A-lines, $6.2 \times 6.2 \text{ mm}$) were made at $132 \mu\text{s}$ per A-line.

5.2.4 Data analysis

The data analysis procedure consisted of several steps. In the first step, the data that was obtained from the mirror in the model eye was analyzed to determine spectrometer specific parameters as described in Chapter 4.⁷⁻⁹ Those parameters were used to map the eye data to k -space. In addition, a phase curve was determined for each camera to compensate for chromatic dispersion in the eye and the interferometer, also described in Chapter 4.⁹ After Fourier transforming the data to ξ -space, Stokes parameters were determined as described in Chapter 3. From the I stokes parameter, the upper and lower boundaries of the retinal nerve fiber layer were determined.¹⁰ In the polarization analysis, surface Stokes parameters were compared with Stokes parameters at a certain depth to determine the depth-resolved phase retardation.^{4-6, 11} This procedure was described earlier in Chapter 3. For the data obtained from a healthy volunteer, the surface Stokes vector was chosen $10 \mu\text{m}$ below the automatically-detected surface, while for the glaucoma patient, we chose a value of $3 \mu\text{m}$, to preserve as many points as possible for accurate data extraction. Moving-average filters were used to reduce the influence of speckle noise. In the horizontal direction we averaged over 20 A-lines, while in the vertical direction we averaged over 3 points, which corresponds to $10 \mu\text{m}$. The thickness and birefringence of retinal nerve fiber layer tissue was measured as a function of sector and radius. Each circular scan was divided in 50 sectors of 7.2° . The 50 sectors almost match the 48 sectors that we used for the time-domain data. However, since we scanned 1000 A-lines per circular scan with SD-OCT compared to 1536 A-lines per time-domain circular scan,

the number of A-lines that was averaged to reduce speckle noise was almost two times lower with the current settings. This may have affected the influence of speckle noise.

Data sets that were acquired with linear scans were processed into a surface image, equivalent to those made with either a fundus camera, a scanning laser ophthalmoscope or with a scanning laser polarimeter. This was done by summing intensity values per A-line to one value. So, instead of a three-dimensional volume, the data set is flattened down to a two-dimensional image, which looks like a fundus image.

5.3 Results and discussion

5.3.1 Results obtained from a healthy volunteer

A set of linear scans ($6.4 \times 6.4 \text{ mm}$, 500×250 data points, acquired at 7.5 kHz), processed in a fundus-like image is displayed in Figure 44. White lines indicate the approximate positions of the smallest and largest circular scans that were analyzed.

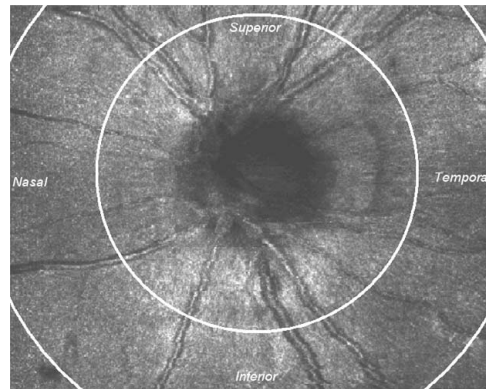


Figure 44: Pseudo fundus image of the optic nerve head, reconstructed from a three-dimensional volume set. The white lines indicate the positions of the smallest and largest diameter circular scans. Large blood vessels can be seen branching out from the optic nerve in the superior and inferior areas.

Circular scans made at 30 kHz and 7.5 kHz were analyzed and compared with each other. The 7.5 kHz data set demonstrated a higher signal-to-noise ratio ($\sim 41 \text{ dB}$ vs. $\sim 36 \text{ dB}$) and did not contain noticeable motion artifacts. Figure 45 shows a structural intensity image taken at 7.5 kHz with a circular scan of the undilated right eye of a 40-year-old healthy volunteer.

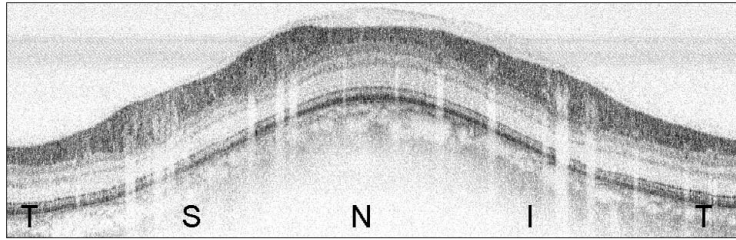


Figure 45: Structural intensity image of a circular scan around the optic nerve head of a healthy volunteer. Positions in the eye are labeled: temporal (T); superior (S); nasal (N); inferior (I). The image measures 0.96 mm deep by 12.6 mm wide and is expanded in vertical direction by a factor of four for clarity. The image was not realigned and shows the true topography of the tissue around the optic nerve head. The dynamic range of the image above the noise floor was 38.5 dB . The image was acquired at an A-line rate of 7.5 kHz . The horizontal lines below the top of the image were caused by electrical noise in the off-axis line scan camera.

The dynamic range of the image is 38.5 dB (in the same data set, images with a dynamic range up to 44 dB were found). Strong reflections are represented by black pixels. The image was expanded in the vertical direction for clarity. As described previously in Chapter 3, the superior (S) and inferior (I) areas contain RNFL tissue that is relatively thick.

Both data sets were analyzed to compare thickness and double-pass phase retardation per unit depth (DPPR/UD) as a function of sector and radius. The data set acquired at 30 kHz was compared with the one taken at 7.5 kHz , as well as with the data set that was earlier acquired with the time-domain system at 256 Hz . An overview of the measurements is given in Figure 47. First, spectral-domain OCT measurements averaged over one sector will be discussed, starting with a measurement in the temporal section, taken from the data presented in Figure 45.

In the temporal area, the RNFL is thin and a relatively low DPPR/UD value is found. The superior sector contains thicker RNFL tissue with a higher birefringence. Nasal plots demonstrate thin RNFL and low birefringence, while inferior plots show thick RNFL with high DPPR/UD values. Both the intensity and thickness curves of Figure 46 are noisier than similar curves obtained from healthy subjects with TD-OCT (Chapter 3).

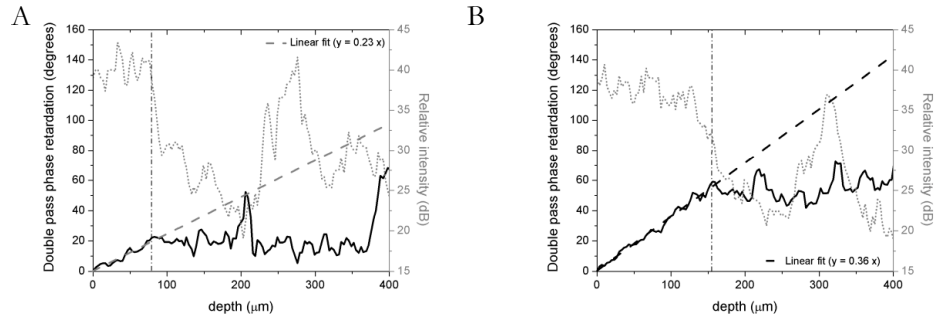


Figure 46: Thickness (dotted line) and DPPR (solid line) plots of sectors temporal (A) and superior (B) to the ONH, acquired with an A-line rate of 7.5 kHz. The data was averaged over a sector of 20 A-lines or 7.5°. DPPR data belonging to the RNFL is fit with a least-squares linear fit. The slope in the equation represents the DPPR/UD. The vertical line indicates the estimated boundary of the RNFL, as determined from the intensity and DPPR data. The increase in DPPR at depths over 150 μm is caused by a low signal between the RNFL and the RPE.

Thickness values were plotted as a function of radius and sector, and data points taken at one radius were connected with a line. The thickness of the line indicates the radius of the scan, with thicker lines of scans closer to the optic nerve head. DPPR/UD values were also plotted as a function of radius and sector, with data points at a certain radius bearing the same symbol. The mean DPPR/UD value per sector was determined and a line connected mean values per sector. The standard error (SE) of the mean was determined and is represented in the graphs by error bars.

Comparing the thickness graphs of Figure 47, a similar trend can be observed, with higher values superiorly and inferiorly. The higher thickness values in these areas can be explained by the presence of arcuate nerve fiber bundles, which branch off towards the fovea. The differences in the thickness measurements can be attributed to subjective interpretation of the data by the operator. An automatic image analysis program may improve the objectivity and therefore the analysis.

The DPPR/UD graphs show similar trends as well, with higher values superiorly and inferiorly. The SD-OCT results obtained at 7.5 kHz match best with the TD-OCT results. The temporal values however increase in both SD-OCT data sets, while these are very low in the TD-OCT setup. The general trend of higher inferior and superior values can be seen in all graphs.

The maximum mean DPPR/UD value measured in this subject with SD-PS-OCT was approximately $0.45^\circ/\mu\text{m}$, while the minimum mean value equals to approximately $0.2^\circ/\mu\text{m}$. These values are equivalent to a birefringence of 5.4×10^{-4} and 2.4×10^{-4} , respectively, measured at 840 nm.

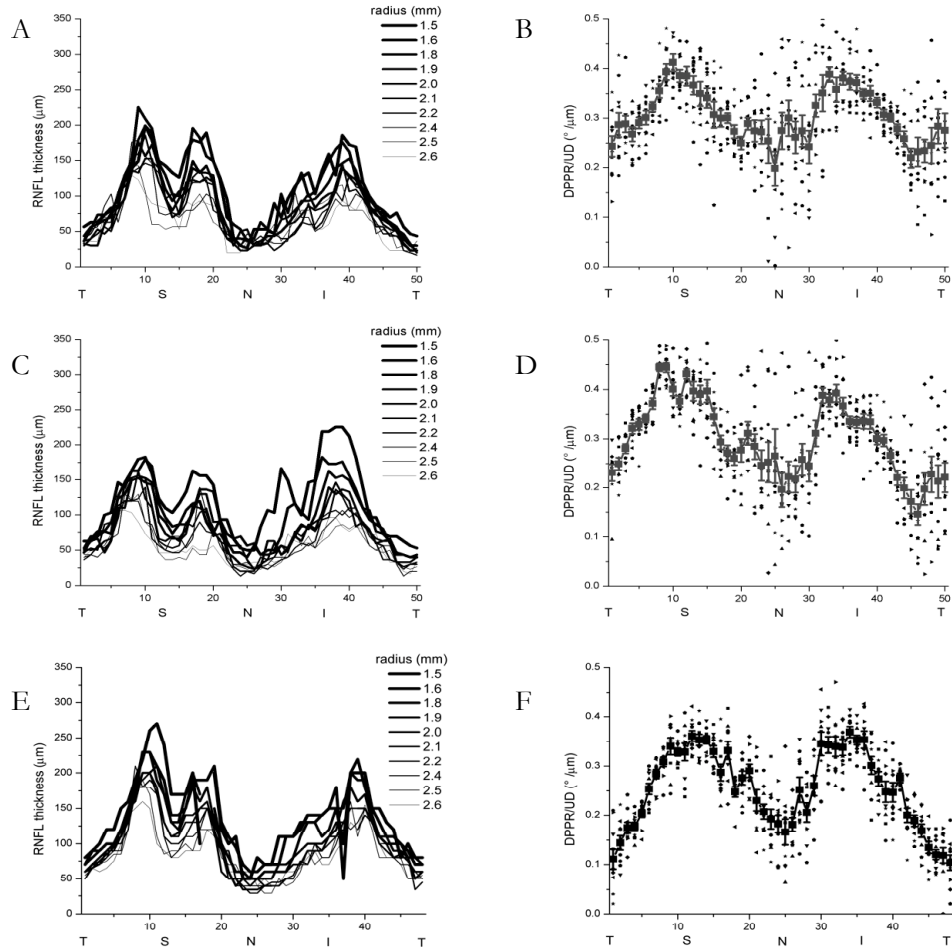


Figure 47: RNFL thickness and DPPR/UD measurements at different integration times. The top two graphs (A,B) display data taken at 7.5 kHz, while the middle two graphs (C,D) were taken at 30 kHz. The bottom two graphs (E,F) are shown for comparison; these were taken at 256 Hz with the time-domain system. The thickness graphs (A, C, E) develop similarly, with a double-hump pattern and higher values superiorly (S) and inferiorly (I). In the superior area, a smaller double-hump pattern can be seen (C). The DPPR/UD graphs develop similarly with high values superior and inferior. The spread of measurement points around the mean values (connected with a line) is higher for the spectral-domain data (B, D) than for the time-domain data (F).

5.3.2 Discussion of results obtained from a healthy subject

Comparing the time-domain DPPR/UD plot (F) with the spectral-domain plots (B, D), the spectral-domain data points are scattered over a larger range. This is partly due to inexperience with a new analysis program, used for the spectral-domain data, by the use of an automatic slope-fitting algorithm and by averaging over a relatively low number of A-lines. For noisy time-domain measurements, the average DPPR value below the RNFL was used to calculate the DPPR/UD. The average DPPR value would be divided by the thickness of the RNFL to calculate the DPPR/UD. For the spectral-domain values, the program would fit a line through the DPPR data points of the RNFL, independent of noise present on the data. For the thick parts of the RNFL, with many data points to fit, this method yields reliable results. For sectors with a thin RNFL, this method is less reliable than the method employed with the time-domain data.

Another difference that can be observed between time-domain and spectral-domain results, is a small offset between DPPR/UD measurements (Figure 47). The highest mean values in the spectral-domain results are around $0.45^\circ/\mu m$, while with the time-domain system values equal or lower than $0.4^\circ/\mu m$ are measured. This difference was attributed to a depth dependent phase difference between the two cameras, caused by inaccurate mapping of the data to k -space. This issue is currently under investigation and can be resolved most likely by an extension of the mapping procedure as described in Figure 28 of section 4.3.1.

The reported higher temporal DPPR/UD values are less reliable due to the thin RNFL at this location. Although we did not quantify the accuracy of the method, an analysis of time-domain results indicated that the DPPR/UD measurement becomes less reliable when the RNFL thickness is lower than $75 \mu m$ (Chapter 3).

A comparison between results obtained with a $30 kHz$ acquisition rate and $7.5 kHz$ rate show that a slower rate yields data with a slightly higher signal-to-noise ratio. Thickness as well as DPPR/UD depth curves display similar trends. The latter result is important for results obtained with the glaucoma patient.

5.3.3 Results of a glaucoma patient

All seven glaucoma patients that were recruited were imaged with SD-PS-OCT. Initial inspection of the data quality indicated that only one data set had a signal-to-noise ratio that was found good enough for analysis. This data was obtained from the left eye of an 81-year old white female. She had undergone cataract surgery 6 years earlier, which possibly lead to the relatively high image quality. Her best-corrected visual acuity was 20/20, and the internal fixation spot was used to stabilize the eye. The visual field test results showed a superior visual field defect, which should result in a thinner nerve fiber layer in the inferior area (the vision of the eye is inverted). The reported field defect was relatively small. Figure 48 shows a structural intensity image

from a circular scan in this patient, taken at a radius of 2 mm and an A-line acquisition rate of 7.5 kHz .

Compared to scans made in healthy volunteers (for instance the scan shown in Figure 45), the contrast between the RNFL and ganglion cell layer, which borders the RNFL, is not as strong. The inferior (I) RNFL tissue of this patient is clearly thinner than the equivalent inferior tissue of a healthy volunteer.

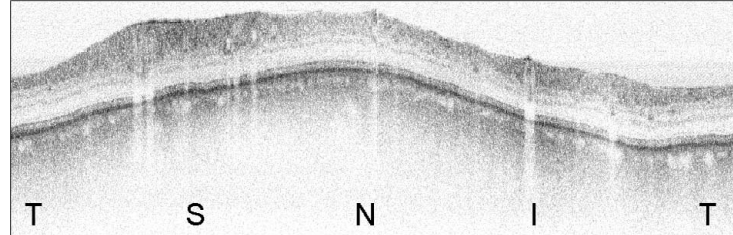


Figure 48: Structural intensity image from a circular scan around the optic nerve head of an 81-year old glaucoma patient. The image shows a relatively thin inferior nerve fiber layer (I), caused by glaucoma. All other areas seem to be unaffected. Positions in the eye are labeled: temporal (T); superior (S); nasal (N); inferior (I). The image measures 0.96 mm deep by 12.6 mm wide and is expanded in the vertical direction by a factor of four for clarity. The dynamic range of the image above the noise floor was 37.4 dB , with A-lines acquired at 7.5 kHz .

The data set that was acquired at 30 kHz had a dynamic range of approximately 24 dB , which is too low for a reliable analysis. Although we acquired almost 400 images from the patient at 7.5 kHz , only one full data set of 10 scans at radii varying between 1.5 and 2.6 mm could be retrieved with an acceptable average dynamic range of approximately 35 dB .

The graphs displayed in Figure 49 are slightly noisier than those in Figure 46, the graphs obtained from the healthy volunteer. A lower signal-to-noise ratio of the data is most likely the source of the noise. Similar to Figure 46, low values are found in the temporal sector and high values in the superior sector. Since 20 A-lines were averaged for these plots, a variation in thickness over the 20 A-lines may have caused problems when determining the thickness of a certain sector (B). Here, the thickness and phase retardation plot do not exactly match up. Although the phase retardation plot indicates a RNFL thickness of at least 210 μm , the intensity plot starts to drop at around 160 μm , indicating the lower border of the RNFL. In this case a thickness of 210 μm was chosen.

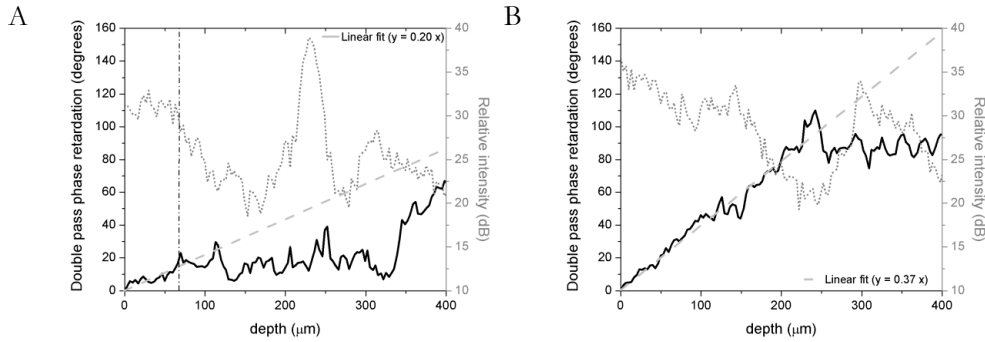


Figure 49: Thickness (dotted line) and DPPR (solid line) plots of an area temporal (A) and superior (B) to the ONH. This data was obtained from a glaucoma patient. DPPR data in each graph belonging to the RNFL is fit with a least-squares linear fit. The slope in the equation represents the DPPR/UD. The vertical line indicates the estimated boundary of the RNFL, as determined from the intensity and DPPR data.

In the structural intensity image displayed in Figure 48 we observed a field defect in the inferior area (labeled “I”). Figure 50 shows the DPPR results from a sector within this field defect. The estimated thickness of approximately $50 \mu m$ is well below the values that are seen in the inferior area of healthy volunteers. This poses a problem as well, since there are fewer data points to fit to and obtain reliable results. The DPPR curve has a slope of $0.44^\circ/\mu m$ in the first $50 \mu m$, indicating relatively highly birefringent tissue, as can normally be seen in the inferior area of normal subjects. The increase in DPPR at a depth of around $150 \mu m$ is due to a low signal. In areas with a low signal, the DPPR calculation becomes unreliable and drifts to 115° , as predicted by theoretical simulation.¹²

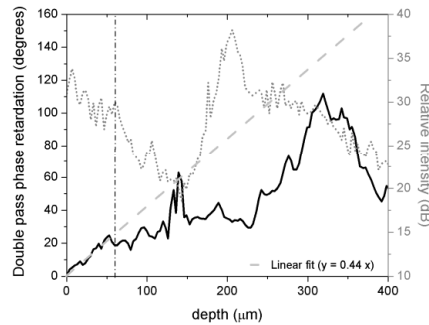


Figure 50: Thickness (dotted line) and DPPR (solid line) plots in a sector that is part of a field defect in the inferior area of a glaucoma patient. Although the RNFL is relatively thin, the DPPR/UD remains high.

After analyzing all sectors at all radii, thickness and DPPR/UD plots were combined in two graphs.

The thickness graph of Figure 51 shows that the thickness measured in the superior area decreases as a function of radius. This decrease was also seen in healthy volunteers (Figure 19, Figure 47). In the inferior area, this decrease as a function of radius is less clear, since curves from different radii overlap. Interestingly, compared to the thickness graph of the healthy volunteers, the inferior area is thinner. In particular, the ratio between the superior and inferior area is much larger in this patient than in a healthy volunteer. The thinner inferior area is in agreement with the visual field defect as measured with the visual field test.

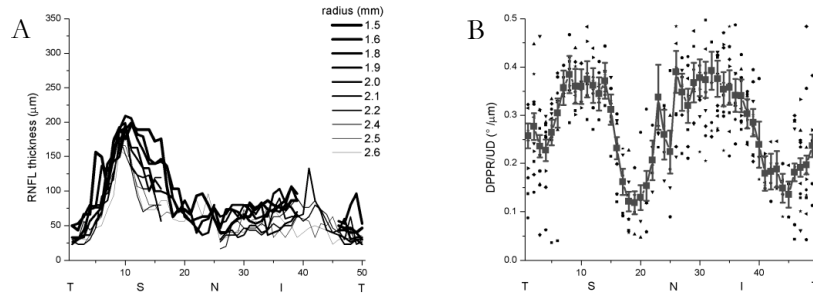


Figure 51: RNFL thickness (A) and DPPR/UD values (B) from nerve fiber layer tissue of a glaucoma patient.

The DPPR/UD graph (B) of Figure 51 shows high superior (S) values. High values are also found between the nasal (N) and inferior (I) areas, while low values occur in the nasal and temporal area. Between the temporal and inferior area, there seems to be a depression. The general trend is similar to the trends observed in all healthy subjects, with both spectral-domain and time-domain OCT. Compared to data from healthy volunteers, the graph is somewhat skewed, with the lowest values occurring around sector 20. In the graph of a healthy volunteer (Figure 47), lowest values occur around sector 25. During the measurements, the subject's head may have been tilted, but this does not explain such a deviation. Furthermore, comparing the glaucomatous structural intensity image of Figure 48 with an intensity image from a healthy subject (Figure 45), there does not seem to be much tilt at all. Overall, the inferior area is relatively thin and contains parts that display normal birefringence, and also parts with a lower birefringence.

When we discussed the results from the healthy volunteers, we mentioned that a different averaging scheme might have been the result of the slightly noisier DPPR graphs. To overcome this problem, the data was analyzed again, but now the

averaging filter was used to average the Stokes parameters of 40 A-lines. Data was consequently mapped over fewer data points in the scan, decreasing the number of sectors by a factor of 2.

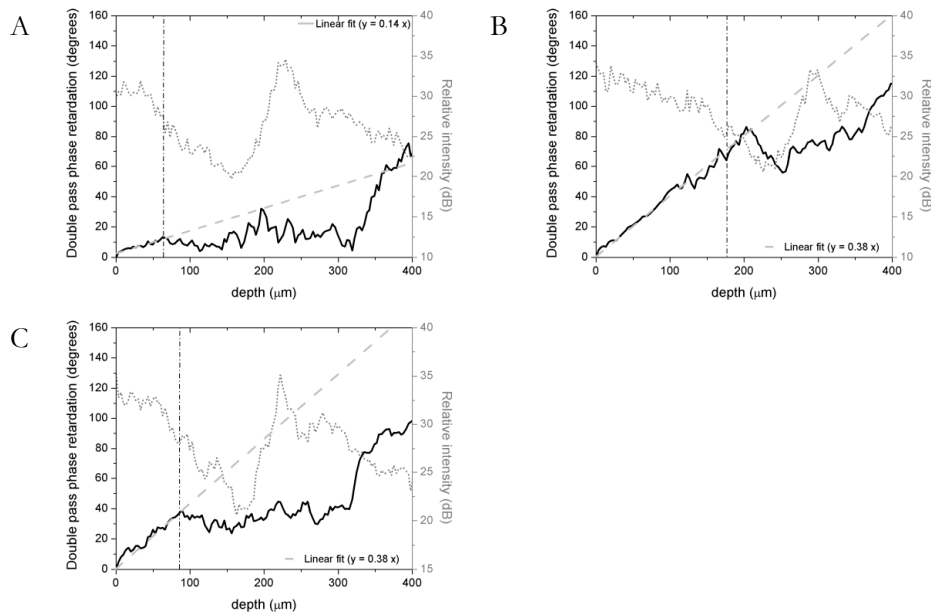


Figure 52: Thickness (dotted line) and DPPR (solid line) plots of an area nasal (A), superior (B) and inferior (C) to the ONH of a glaucoma patient. For these plots, Stokes parameters of 40 A-lines were averaged, to reduce the influence of speckle noise.

Figure 52 contains graphs of nasal (A), superior (B) and inferior (C) sectors. All graphs demonstrate DPPR/UD values that are very similar to the ones displayed in Figure 51. Comparing these graphs with sector graphs of the same patient that were averaged over fewer A-lines (Figure 49), these curves are slightly less noisy. The results of all sectors and radii are given in Figure 53. Although the averaging procedure reduces the spread in data points, the overall trend remains very similar.

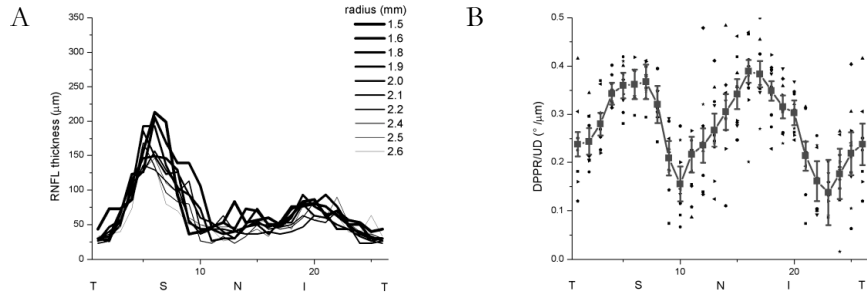


Figure 53: RNFL thickness (A) and DPPR/UD values (B) from nerve fiber layer tissue of a glaucoma patient. For these plots, Stokes parameters from 40 A-lines were averaged. The trends that could be seen in glaucoma data averaged over 20 A-lines remain the same: high DPPR/UD values superiorly and inferiorly, with the thickest tissue located in the superior area.

The maximum mean DPPR/UD value measured in this patient with SD-PS-OCT was approximately $0.4^{\circ}/\mu m$, while the minimum mean value equals approximately $0.15^{\circ}/\mu m$. These values are equivalent to a birefringence of 4.8×10^{-4} and 1.8×10^{-4} , respectively, measured at 840 nm .

5.3.4 Discussion of glaucoma patient results

In the introduction of this thesis, it was hypothesized that glaucoma would cause a decrease of RNFL birefringence, since less birefringent amorphous glial cells would replace the well aligned and birefringent nerve fibers. Although the inferior area of the glaucoma patient described in section 5.3.3 is relatively thin as a result of glaucoma, most of the DPPR/UD values in this area appear normal. There is a slight depression in the region between the inferior and temporal area, which can be seen in some healthy subjects as well, but between the nasal and inferior areas, normal inferior values occur. The peak value of approximately $0.4^{\circ}/\mu m$ is very similar to the DPPR/UD value in the superior area, and those of the inferior and superior area of healthy volunteers.

First, most of the RNFL in the inferior area is only slightly thicker than $75 \mu m$. For a time-domain measurement at the same signal-to-noise ratio, DPPR/UD measurements are considered to be reliable. However, these measurements were obtained at a lower signal-to-noise ratio than measurements obtained from a healthy subject (Figure 47 B and D). An analysis of those results indicated that SD-OCT measurements in the thinner parts of the RNFL were most likely less reliable than those obtained with TD-OCT. The signal-to-noise ratio of the glaucoma data was on average approximately 3 dB lower than the data from the healthy subject. A lower signal-to-noise ratio is not beneficial for a reliable DPPR/UD result.

These preliminary results were obtained from one glaucoma patient with one type of glaucoma and cannot be translated to all glaucoma patients. Measurements on other glaucoma patients, preferably at a slightly larger signal-to-noise ratio have to demonstrate that the observed trend is consistent for all glaucoma patients.

A higher signal-to-noise ratio can be achieved in several ways. First, it can be improved by increasing the source arm power. The ANSI standards allow a higher power than $600 \mu W$ for scanning beams. At an acquisition speed of 7.5 kHz , a scan length of 9.4 mm (scan with the shortest radius) and a scan time of 132 ms per scan, the power can be increased by a factor of 15 to approximately 9 mW . Another option is to slow down the scan rate, without increasing the power. Preliminary experiments, which were not reported here, indicate that reliable DPPR/UD results can be obtained by slowing down the scan rate to 3 kHz . A longer acquisition time may become problematic for the glaucoma patients, since motion artifacts are more likely to occur. A retina tracker can avoid such artifacts, and also automatically rescan areas that were missed because of blinks.¹³ Since spectral-domain measurements in a healthy volunteer match well with those obtained in time-domain, another option would be to recruit young patients with glaucoma. So far, the study focused on patients with moderate to severe glaucoma, since the contrast between these groups and healthy subjects is large. Unfortunately, patients with moderate and severe glaucoma generally have other eye related problems, which are not beneficial for the eye scanning process. A study on younger patients will avoid these problems.

5.4 Conclusion

The birefringence of healthy RNFL tissue, measured in one healthy subject with spectral-domain polarization-sensitive OCT, is constant as a function of scan radius but varies as a function of position around the ONH, with higher values occurring superior and inferior to the ONH. The measured mean DPPR/UDs around the ONH in one healthy subject varied between 0.20 and $0.45 \text{ }^\circ/\mu m$. These values are equivalent to birefringences of 2.4×10^{-4} and 5.4×10^{-4} , measured at a wavelength of 840 nm .

Measurements in one glaucoma patient with a small visual field defect demonstrate nerve fiber layer thinning in inferior sectors due to glaucoma. Polarization-sensitive measurements seem to indicate that a portion of the nerve fiber layer tissue in these sectors is just as birefringent as healthy tissue. However, measurements in this thin area at the measured signal-to-noise ratio are not as reliable as measurements in thicker RNFL, or as measurements made at a higher signal-to-noise ratio.

References

1. Y. Yasuno, S. Makita, Y. Sutoh, M. Itoh and T. Yatagai, "Birefringence imaging of human skin by polarization-sensitive spectral interferometric optical coherence tomography," *Optics Letters*, 27, 1803-1805 (2002).
2. Y. Yasuno, S. Makita, T. Endo, et al., "Polarization-sensitive complex Fourier domain optical coherence tomography for Jones matrix imaging of biological samples," *Applied Physics Letters*, 85, 3023-3025 (2004).
3. J. Zhang, W.G. Jung, J.S. Nelson and Z.P. Chen, "Full range polarization-sensitive Fourier domain optical coherence tomography," *Optics Express*, 12, 6033-6039 (2004).
4. B. Cense, T.C. Chen, B.H. Park, M.C. Pierce and J.F. de Boer, "In vivo depth-resolved birefringence measurements of the human retinal nerve fiber layer by polarization-sensitive optical coherence tomography," *Optics Letters*, 27, 1610-1612 (2002).
5. B. Cense, T.C. Chen, B.H. Park, M.C. Pierce and J.F. de Boer, "In vivo birefringence and thickness measurements of the human retinal nerve fiber layer using polarization-sensitive optical coherence tomography," *Journal of Biomedical Optics*, 9, 121-125 (2004).
6. B. Cense, T.C. Chen, B.H. Park, M.C. Pierce and J.F. de Boer, "Thickness and birefringence of healthy retinal nerve fiber layer tissue measured with polarization-sensitive optical coherence tomography," *Investigative Ophthalmology & Visual Science*, 45, 2606-2612 (2004).
7. N. Nassif, B. Cense, B.H. Park, et al., "In vivo human retinal imaging by ultrahigh-speed spectral domain optical coherence tomography," *Optics Letters*, 29, 480-482 (2004).
8. N.A. Nassif, B. Cense, B.H. Park, et al., "In vivo high-resolution video-rate spectral-domain optical coherence tomography of the human retina and optic nerve," *Optics Express*, 12, 367-376 (2004).
9. B. Cense, N.A. Nassif, T.C. Chen, et al., "Ultrahigh-resolution high-speed retinal imaging using spectral-domain optical coherence tomography," *Optics Express*, (2004).
10. R. Chan, J. Kaufhold, L. Hemphill, R. Lees and W. Karl. Anisotropic edge-preserving smoothing in carotid B-mode ultrasound for improved segmentation and intima-media thickness measurement. in *Computers in Cardiology*. 2000. Cambridge, MA.: IEEE.
11. C.E. Saxer, J.F. de Boer, B.H. Park, et al., "High-speed fiber-based polarization-sensitive optical coherence tomography of in vivo human skin," *Optics Letters*, 25, 1355-1357 (2000).
12. B.H. Park, C. Saxer, S.M. Srinivas, J.S. Nelson and J.F. de Boer, "In vivo burn depth determination by high-speed fiber-based polarization sensitive optical coherence tomography," *Journal of Biomedical Optics*, 6, 474-9 (2001).
13. R.D. Ferguson, D.X. Hammer, L.A. Paunescu, S. Beaton and J.S. Schuman, "Tracking optical coherence tomography," *Optics Letters*, 29, 2139-2141 (2004).

6. Discussion, conclusion and outlook

6.1 Discussion

In the introduction of this thesis, two new technologies were proposed for the early detection of glaucoma: polarization-sensitive optical coherence tomography and spectral-domain optical coherence tomography. Are these new technologies suitable for the detection of glaucoma? Or even more important, are these technologies suitable for the *early* detection of glaucoma? In several studies the sensitivity and specificity of other imaging modalities such as SLO, SLP and (time-domain) OCT have been tested on groups of healthy volunteers and age-matched glaucoma patients.¹⁻⁶ Although in this thesis, PS-OCT and SD-OCT were only tested on a few volunteers and patients, compared to standard time-domain OCT they offer a higher axial resolution (both modalities), a higher acquisition speed and higher sensitivity (SD-OCT), and a depth-resolved birefringence measurement (PS-OCT). Employed with a normative database, it is most likely that both technologies will perform equal to, or better than any current technology.

The onset of glaucoma reveals itself through changes in the retina, as ganglion cells and their axons degenerate as glaucoma progresses. In a very early stage, these changes are small and become larger as the disease progresses. An imaging system with higher measurement accuracy, such as ultrahigh-resolution spectral-domain optical coherence tomography, will therefore improve the chance of early detection. The average thickness of a healthy retinal nerve fiber layer is approximately 150 μm . In the areas most sensitive to glaucoma, the thickness is even higher, up to 300 μm . A system with an axial resolution of $\sim 3 \mu\text{m}$ and a measurement error of $2 \times \sim 3 \mu\text{m}$ for nerve fiber layer thickness determination will be sensitive to 2% changes in retinal thickness. This would make ultrahigh resolution SD-OCT more sensitive than Humphrey's visual field test, which needs approximately 40% loss of axons before it can detect glaucoma.⁷ The SD-OCT system's high sensitivity to light allows for fast volume scanning and with an eye tracker, motion artifacts and data loss due to blinking can be avoided.⁸ A baseline measurement would be followed by regular follow-ups, and small changes in nerve fiber layer thickness could be detected. By comparing measurements with a normative database, and taking age-related effects into account, an abnormal reduction of nerve fiber layer tissue could indicate the onset of glaucoma.

When the axons of the ganglion cells are replaced by glial cells,⁷ a change in retinal nerve fiber layer thickness may be more difficult to detect in structural intensity images alone. The depth-resolved birefringence measurement of PS-OCT can distinguish between birefringent nerve fiber tissue and non-birefringent glial cells.

Could a change in the tissue structure be measured with PS-OCT? First of all, where would these changes most likely happen in the RNFL? In general, glaucoma initially affects the superior and inferior areas around the optic nerve head. Minckler *et al.* determined the nerve fiber axons distribution in primate eyes by means of horse radish staining.⁹ In the nerve fiber layer around the ONH of a primate eye, the axons of peripheral ganglion cells are located at the bottom of the RNFL close to the ganglion cell layer. In contrast, ganglion cells close to the ONH have axons that are located at the top of the RNFL. If the same distribution holds for human eyes, the axons at the *bottom* of the RNFL are most likely to be affected first due to glaucoma. A change in birefringence at the bottom of the RNFL would only affect the corresponding part of the double-pass phase retardation plots. In the double-pass phase retardation plots of healthy eyes, as given in Figure 13 of Chapter 3, the transition from a linearly increasing phase retardation to a constant phase retardation is not abrupt, but rather continuous. Experiments on patients with early-stage glaucoma are necessary to prove if a deviation in slope at the bottom of the RNFL can be detected with PS-OCT. Furthermore, the time scale at which these changes happen has to be long enough for successful detection. For instance, repeated SLP measurements on a patient with acute anterior ischemic optic neuropathy indicate that the phase retardation in affected areas decreases over a time-course of weeks,¹⁰ suggesting that the nerve fiber layer tissue can degenerate over a short time scale. A measurement with a PS-OCT system on such a patient could determine if the loss of phase retardation is caused by a decrease in birefringence (which may occur if for instance nerve fiber layer tissue is replaced by non-birefringent glial cells) or if the tissue simply disappears. In case of the latter mechanism, PS-OCT will not be able to detect a change of birefringence, because the affected tissue no longer exists.

6.2 Conclusion

A slit lamp-based interface was constructed for ophthalmic optical coherence tomography (OCT) measurements on healthy volunteers and glaucoma patients *in vivo*. The system is equipped with a camera that helps the operator to find locations in the eye. For the eye that is under investigation, a fixation spot in the view of the subject can be used to stabilize the eye and to shift the eye to a desired position.

A polarization-sensitive OCT (PS-OCT) system was set up to perform retinal phase retardation measurements in subjects *in vivo*. The system had an A-line rate of 256 Hz and a depth range of 1 mm. Five healthy subjects were successfully imaged with this system, and measurement results demonstrated a variation in thickness as well as double-pass phase retardation per unit depth (DPPR/UD) of the retinal nerve fiber layer. In two healthy subjects, the measured DPPR/UDs around the optic nerve head varied between 0.10 and 0.35 °/μm. These values are equivalent to birefringence of 1.2 x 10⁻⁴ and 4.1 x 10⁻⁴, measured at a wavelength of 840 nm. In addition, two

glaucoma patients were imaged with this system. From the results it was concluded that a more sensitive system was necessary for imaging of glaucoma patients.

Our PS-OCT system was based on the classical form of OCT, so-called time-domain OCT. This technology only detects photons that are within a rapid-scanning detection window. By replacing the time-domain detector by a spectrometer, and eliminating the scanning of the reference arm, all photons returning from the sample arm of the interferometer are used for the reconstruction of an image. A spectral-domain OCT system equipped with a high-speed spectrometer (29,300 spectra per second) was constructed. Theoretically and experimentally, a signal-to-noise ratio gain of more than 20 dB was demonstrated. The standard broadband source ($\Delta\lambda = 50 \text{ nm}$) was replaced by an ultra-broadband source ($\Delta\lambda = 150 \text{ nm}$) to perform high-resolution measurements. A coherence length of $3.5 \mu\text{m}$ (FWHM) was measured in the center of the fovea of a healthy volunteer *in vivo*. To our knowledge, this was the first time that a coherence length was determined in a human eye. Movies at 29.3 frames per second with 500 A-lines per frame seemed to indicate two layers at the location of the RPE as well as previously unseen small structures in the two plexiform layers, which from their location were believed to be blood vessels.

A combination of these two new technologies allows a birefringence measurement to be performed at a higher sensitivity. The higher sensitivity can be used to acquire data faster and to acquire it with a higher signal-to-noise ratio. We built a spectral-domain polarization-sensitive OCT system and successfully measured the thickness and DPPR/UD of one healthy volunteer and one glaucoma patient. The measurements on a healthy subject were acquired up to 145 times faster than with a conventional PS-OCT system, yielding similar results. Preliminary measurement results in one glaucoma patient did not give a satisfying conclusion, as to whether the birefringence of the glaucomatous retina is affected. Measurements on more glaucoma patients have to be made, to confirm if the results found are valid.

6.3 Outlook

Measurements on more patients have to be done to determine the effects of glaucoma on the retinal nerve fiber layer. Our preliminary results indicate that eyes without cataracts, or eyes of younger patients are more likely to yield good data sets.

Currently, the data analysis is done semi-automatically. The operator has to determine the boundaries of the RNFL per sector. The result of this analysis is a set of curves that display the thickness and DPPR/UD of sectors at different radii. With automatic image analysis, this process can be completely automated and any subjectivity from the operator's side is avoided. By applying a moving average filter, speckle noise can be reduced while the number of measurements per scan can be increased. Currently, only 25 to 50 sectors are analyzed per scan. With a moving average filter, the density of measurements could theoretically be increased to the total

numbers of A-lines divided by two (for each polarization-sensitive measurement, two A-lines are necessary), improving the spatial resolution. Figure 54 shows the structural intensity image of a healthy volunteer, where the boundaries of the retinal nerve fiber layer were automatically detected.

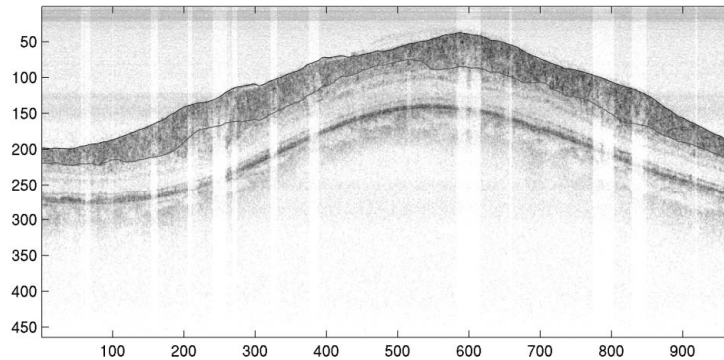


Figure 54: Structural intensity image of a circular scan around the optic nerve head of a healthy volunteer. The image measures approximately 12 mm wide and 1.7 mm deep and displays 1000 A-lines. The automatically-detected upper- and lower boundaries are represented by continuous lines. Light colored columns indicate the location of large blood vessels in the RNFL.

Although the results of the boundary detection algorithm look promising, the algorithm has to be used with glaucoma patients as well. As these patients have less experience fixating and tend to blink, a successful analysis strongly depends on the quality of the data.

References

1. F.A. Medeiros, L.M. Zangwill, C. Bowd and R.N. Weinreb, "Comparison of the GDx VCC scanning laser polarimeter, HRT II confocal scanning laser ophthalmoscope, and stratus OCT optical coherence tomograph for the detection of glaucoma," *Archives of Ophthalmology*, 122, 827-837 (2004).
2. N.J. Reus and H.G. Lemij, "Diagnostic accuracy of the GDx VCC for glaucoma," *Ophthalmology*, 111, 1860-1865 (2004).
3. C.A. Sanchez-Galeana, C. Bowd, E.Z. Blumenthal, et al., "Using GDx scanning laser polarimetry and optical coherence tomography clinical print-outs to detect glaucoma," *Investigative Ophthalmology & Visual Science*, 41, S287-S287 (2000).
4. C. Sanchez-Galeana, C. Bowd, E.Z. Blumenthal, et al., "Using optical imaging summary data to detect glaucoma," *Ophthalmology*, 108, 1812-8 (2001).
5. L.M. Zangwill, C.F. Chang, J.M. Williams and R.N. Weinreb, "New technologies for diagnosing and monitoring glaucomatous optic neuropathy," *Optometry and Vision Science*, 76, 526-536 (1999).
6. L.M. Zangwill, C. Bowd, C.C. Berry, et al., "Discriminating between normal and glaucomatous eyes using the Heidelberg Retina Tomograph, GDx Nerve Fiber Analyzer, and Optical Coherence Tomograph," *Archives of Ophthalmology*, 119, 985-993 (2001).

7. H.A. Quigley, E.M. Addicks and W.R. Green, "Optic nerve damage in human glaucoma. III. Quantitative correlation of nerve fiber loss and visual field defect in glaucoma, ischemic neuropathy, papilledema, and toxic neuropathy," *Archives of Ophthalmology*, 100, 135-46 (1982).
8. R.D. Ferguson, D.X. Hammer, L.A. Paunescu, S. Beaton and J.S. Schuman, "Tracking optical coherence tomography," *Optics Letters*, 29, 2139-2141 (2004).
9. D.S. Minckler, "The Organization of Nerve-Fiber Bundles in the Primate Optic-Nerve Head," *Archives of Ophthalmology*, 98, 1630-1636 (1980).
10. T.P. Colen, J.A.M. van Everdingen and H.G. Lemij, "Axonal loss in a patient with anterior ischemic optic neuropathy as measured with scanning laser polarimetry," *American Journal of Ophthalmology*, 130, 847-850 (2000).

7. Summary

Glaucoma is the world's second leading cause of blindness. The disease causes irreversible damage to the retinal ganglion cells, resulting in thinning of the retinal nerve fiber layer (RNFL). When glaucoma is detected at an early stage, further loss of vision can be prevented by treatment. Current measurement techniques are not sensitive enough to detect glaucoma at an early stage, which is essential for successful glaucoma treatment and management. The visual field test, the gold standard for glaucoma detection, can only detect glaucoma when up to 40% of the RNFL is irreversibly lost. In this thesis, two new imaging modalities are proposed for the early detection of glaucoma. Both modalities are based on optical coherence tomography, a technology that uses low-coherence light to create two-dimensional images of the retina. Depth scans are made as reflections are detected as a function of path length difference by rapidly changing the reference arm length of an interferometer. The sensitive coherence window that is created rejects light returning from other depths.

Chapter 2 deals with the interface that allows us to perform retinal measurements. For measurements in the eye, a special interface is required. Great care was paid to the construction of such an interface, designed around pupil and image planes, making stable measurements on different areas of the retina possible.

Chapter 3 is devoted to polarization-sensitive optical coherence tomography (PS-OCT). This technology uses polarized light to measure the depth-resolved birefringence of tissue. A fiber-based system was built and measurements were performed on healthy volunteers as well as glaucoma patients. The peripapillary area (the area around the optic nerve head) is most sensitive to changes induced by glaucoma. Concentric scans with increasing diameters up to 2.6 *mm* were made around the optic nerve head. The measurement time for each scan was 6 seconds, and eyes were dilated prior to an imaging session. Birefringence of healthy RNFL was shown to be constant as a function of scan radius but varying as a function of position around the ONH, with higher values occurring superior and inferior to the ONH. Measured DPPR/UDs around the ONH of two healthy subjects varied between 0.10 and 0.35 $^{\circ}/\mu\text{m}$. These values are equivalent to birefringence values of 1.2×10^{-4} and 4.1×10^{-4} , measured at a wavelength of 840 *nm*. Measurements of glaucomatous retinas demonstrated nerve fiber layer thinning due to glaucoma. The time-domain PS-OCT measurements of glaucomatous RNFL were not sensitive enough to measure birefringence reliably.

In Chapter 4, a spectral-domain optical coherence tomography system is described. In a time-domain system, only those photons returning from a certain depth (within the coherence window) are detected, making this technology rather inefficient. In spectral-domain optical coherence tomography (SD-OCT), photons returning from all depths are recorded simultaneously, making the technology more

efficient than the time-domain variant. We theoretically and experimentally demonstrated a sensitivity improvement of SD-OCT over TD-OCT by a factor of 148 (21.7 *dB*). In addition, we demonstrated ultrahigh-speed *in vivo* human retinal OCT imaging at 29,300 depth profiles/*s*, resulting in cross-sectional imaging at a video rate with 6 μm resolution. Motion artifacts, commonly present in both research and commercial ophthalmic OCT systems were greatly reduced, thus minimizing the image distortion by involuntary eye movement.

The axial resolution of an OCT system can be improved by using a source with a broader bandwidth. In a time-domain system, data acquired with such a source incurs a penalty in sensitivity, which is usually compensated for by slowing down the acquisition speed. In spectral-domain OCT, such a penalty does not exist since the sensitivity does not depend on the detection bandwidth. We built a spectral-domain system with an ultra-broadband source. One disadvantage of such a source is that chromatic dispersion is induced, which decreases the axial resolution. After dispersion compensation in software, the coherence length measured from a mirror in air was equal to 4.0 μm ($n = 1$). The dispersion-compensated axial resolution obtained from a reflecting spot in the fovea was equal to 3.5 μm ($n = 1.38$). To our knowledge, this was the first coherence length measured in the human eye *in vivo*. The combination of high axial resolution measurements at a high data acquisition rate allows us to identify features that have not been seen in the human retina before with OCT. Movies at 29.3 frames per second with 500 A-lines per frame seem to indicate two layers at the location of the RPE, as well as previously unseen small structures in the two plexiform layers, which determined from their location are believed to be blood vessels. Comparing the performance of our ultrahigh-resolution SD-OCT system with a conventional high-resolution time-domain OCT system, the A-line rate of the spectral-domain OCT system was 59 times higher at a 5.4 *dB* lower sensitivity.

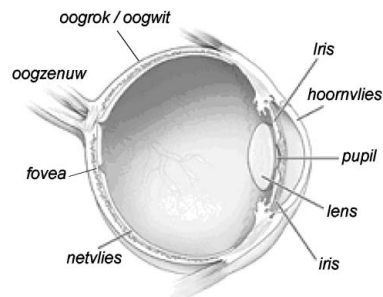
Chapter 5 is devoted to the most recent developments in optical coherence tomography. With a combination of spectral-domain OCT and polarization-sensitive OCT, polarization data with a dynamic range of approximately 35 *dB* was obtained from the retina of a glaucoma patient. The time required for a measurement of 12 concentric circular scans was 1.6 seconds, which is 45 times faster than time-domain PS-OCT measurements with a lower signal-to-noise ratio. Similar measurements on a healthy volunteer with spectral-domain polarization-sensitive OCT yielded images with a dynamic range of approximately 40 *dB*. Three-dimensional volume data was reduced to a single two-dimensional image, which resembles a fundus image.

Measurements on a healthy volunteer gave results that were similar to those that were previously obtained with the slower time-domain polarization-sensitive OCT system. Measurements on one glaucoma patient did not give a satisfying conclusion, regarding whether the birefringence of the glaucomatous retina is affected or not. Measurements on more patients have to be made to determine the effects of glaucoma on the retinal nerve fiber layer.

8. Samenvatting voor leken

Glaucoom is een ziekte die het gezichtsveld in één of beide ogen aantast. Het centrale deel van het gezichtsveld kan tot heel laat in het ziekteproces intact blijven, waardoor een patiënt pas laat in het ziekteproces klachten kan krijgen. Het centrale deel van het gezichtsveld wordt gebruikt om boeken te lezen, of om televisie te kijken. De periferie van het gezichtsveld is het meest gevoelig voor de ziekte. Dat deel is belangrijk in het verkeer en bij balsporten. Ouderen zijn gevoeliger voor de ziekte dan jongeren, en de kans om glaucoom te krijgen is ook groter als de ziekte in de familie voorkomt. Glaucoom komt voor bij grofweg 1% van de wereldbevolking. Daardoor is glaucoom de tweede oorzaak van blindheid in de wereld. De belangrijkste oorzaak is staar, een ziekte die leidt tot vertroebeling van de lens. Deze ziekte kan met een relatief eenvoudige operatie verholpen worden. Helaas is er voor glaucoom geen behandeling mogelijk. Het gezichtsveld dat eenmaal verloren is, kan niet meer gerepareerd worden. De ziekte kan wel gestabiliseerd worden. Voordat we hier verder op in gaan, bespreken we eerst de opbouw van het oog.

8.1 De opbouw van het oog



Figuur 1: Dwarsdoorsnede van het oog.

Het oog zit opgesloten in een oogkas. Het ziekteproces van glaucoom speelt zich voornamelijk af aan de voor- en achterkant van het oog. Aan de voorkant vinden we, van voren naar achteren, het doorzichtige hoornvlies, de lens en de pupil. Tussen de voorkant van het oog en de achterkant van het oog zit een geleachtige doorzichtige vloeistof. De achterkant van het oog bestaat uit verschillende lagen. Stel dat we een oog uit de oogkas halen, en we kijken naar de achterkant van het oog, dan is het oogwit de buitenste laag die we kunnen zien. Dit wordt ook wel de oogrok genoemd. Tussen het netvlies en de oogrok bevindt zich een netwerk van bloedvaten. Deze bloedvaten zijn gescheiden van de lichtgevoelige cellen door onder andere een laag

pigmentcellen. De staafjes en kegeltjes zijn cellen die licht omzetten in elektrische signalen die via zenuwen naar de hersenen worden gevoerd. *Bovenop* de staafjes en kegeltjes vinden we zenuwcellen en zenuwen. We kijken dus als het ware door onze zenuwen heen. Deze zenuwen spelen een belangrijke rol in glaucoom. De zenuwen liggen in een dunne laag over het netvlies, en die laag is het *dunst* in het centrale deel van het oog met de meeste kegeltjes, en het dichtst rondom de blinde vlek of de oogzenuw, omdat alle zenuwen daar samen komen. Vanuit de blinde vlek verbindt de oogzenuw het oog met de hersenen. Net rondom die oogzenuw is die zenuwlaag zo'n twee a driehonderd micrometer dik. Dat is net zo dik als 2 á 3 A4tjes.

Het hoornvlies en de lens bestaan uit doorzichtig weefsel, om licht op het netvlies te kunnen focuseren. Vanwege die doorzichtigheid kunnen ze niet direct via bloedvaten gevoed worden. Stel dat er bloedvaten aanwezig waren, dan zou je door die bloedvaten heen moeten kijken. Dat is net alsof je door een rode lap stof kijkt! Maar die bloedvaten zijn wel erg belangrijk om het oog gezond te houden. Dit probleem is op een ingenieuze manier opgelost. Achter de pupil zitten lichaampjes die een doorzichtige vloeistof afscheiden, een soort doorzichtig bloed. Dit vocht kan van achter de pupil naar de voorkant van de pupil stromen - de pupil is immers open - om daar gezonde cellen van de lens en het hoornvlies te voeden en dode cellen af te voeren. Deze vloeistof wordt constant ververs, maar moet ook worden afgevoerd. Ook hiervoor bestaat een ingenieus systeem: tussen het hoornvlies en de pupil zit een filtersysteem dat het vocht afvoert. Tijdens het ouder worden of door een erfelijk probleem kan het filter echter verstopt raken, of kapot gaan. Ondertussen maakt het oog net zoveel vocht aan als normaal. Als er meer vocht in het oog komt dan dat er wordt afgevoerd, dan neemt de druk toe, net als in een ballon die wordt opgeblazen. De oogdruk kan door een oogarts worden gemeten en als de druk hoger is dan normaal, dan bestaat er een *verhoogde kans* op glaucoom.

8.2 Glaucoom

Wat is de oorzaak van glaucoom? Dit is een vraag die de wetenschap nog niet heeft opgelost. Er bestaan twee theorieën. Er zijn aanwijzingen dat bij een verhoogde oogdruk de bloedvaten in het netvlies worden samengeknepen. Beetje morbide misschien, maar dit proces kun je goed vergelijken met het wurgen van een mens: handen die samenknijpen rondom de nek verhogen de druk op de bloedvaten, die daardoor worden afgeknepen, wat uiteindelijk leidt tot een gebrek aan zuurstof in de hersenen. Hersencellen hebben veel bloed en zuurstof nodig om te overleven. In het oog kan volgens de theorie iets soortgelijks gebeuren. Door de verhoogde oogdruk worden bloedvaten in het netvlies aan de achterkant van het oog afgeknepen, waardoor het netvlies niet voldoende gevoed kan worden. De meeste cellen in het netvlies kunnen daar eigenlijk best goed tegen, met uitzondering van cellen die heel erg op hersencellen lijken, de ganglioncellen. Dat is niet zo gek, want deze cellen

ontwikkelen zich vanuit de hersenen in het embryonisch groeiproces. De ganglioncellen sterven volgens de theorie bij gebrek aan bloed af, en de daaraan verbonden zenuwuiteinden, die de cellen verbinden met de oogzenuw en de hersenen, sterven ook af. Ondanks dat de lichtgevoelige staafjes en kegeltjes gewoon intact blijven bij glaucoom, en de rest van het netvlies nog eigenlijk best goed werkt, is door het kapotgaan van de zenuwen het contact met de hersenen verbroken. De patiënt is daardoor gedeeltelijk blind. In een later stadium van de ziekte kan dit zelfs leiden tot totale blindheid.

Volgens een tweede theorie zorgt een verhoogde oogdruk ervoor dat de oogzenuw afgeknepen wordt. Hiervoor halen we weer in gedachte het oog uit de oogkas en zien we aan de achterkant van het oog de oogzenuw, een bundel zenuwen. Rondom die oogzenuw zit stug bindweefsel, in de vorm van een ring. Je kunt deze situatie vergelijken met een vinger in een fles bier die je niet meer los krijgt. Lastig, maar als je niet in paniek raakt, dan krijg je die vinger er wel uit. Maar maak je je onnodig druk, en zwelt je vinger op, dan zit je vinger vast in de flessenhals, en dat kan pijn doen. Iets soortgelijks kan zich volgens de theorie ook bij glaucoom afspelen. Door de verhoogde oogdruk worden de zenuwen tegen het bindweefsel aangedrukt, waardoor de zenuwen worden afgeknepen. Zenuwen kunnen daar niet goed tegen, en sterven daardoor af.

We weten dus nog steeds niet welke theorie de beste kans maakt. Het zou goed kunnen zijn dat er nog andere mechanismen bestaan, of dat glaucoom wordt veroorzaakt door een combinatie van deze twee theorieën.

Afgestorven zenuwen en ganglioncellen kunnen niet meer door het lichaam gerepareerd worden. Als glaucoom in een vroeg stadium ontdekt wordt, dan kan de ziekte door een oogarts gestabiliseerd worden. Dit stabiliseren is gericht op het omlaag brengen van de oogdruk. Dat voorkomt in de meeste gevallen meer schade aan het oog. De oogdruk kan op verschillende manieren worden verlaagd. Men kan met medicijnen ervoor zorgen dat er meer vocht uit het oog wordt afgevoerd, of dat er minder vocht wordt aangemaakt. Een andere oplossing is om met behulp van een operatie een soort ventiel in het oog aan te brengen, zodat overtollig vocht kan worden afgevoerd.

We hadden het al eerder over de verschillen tussen staar en glaucoom. Staar is een ziekte die je als patiënt gemakkelijk ontdekt. Het zicht neemt snel af als de lens vertroebelt en dat is een goede raadgever om eens naar de oogarts te gaan. Voor glaucoom geldt dat niet zo sterk, omdat het centrale deel van het gezichtsveld tot in een laat stadium van de ziekte goed kan werken. Vooral als je tot een risicogroep behoort, is het raadzaam om regelmatig naar de oogarts te gaan, om zo glaucoom in een vroeg genoeg stadium te kunnen ontdekken.

Oogartsen gebruiken verschillende methodes om te zien of de laag zenuwen op het netvlies is aangetast. Bij de meest gebruikte methode, perimetrie genaamd, kijkt de oogarts zelf niet naar het netvlies. Hierbij moet de patiënt een test uitvoeren, waarvan

de resultaten door de oogarts geïnterpreteerd worden. Deze methode is helaas niet erg effectief in het opsporen van glaucoom. Over het algemeen is al zo'n 40% van het zenuwweefsel in het oog verdwenen voordat deze test aangeeft of iemand lijdt aan glaucoom. In de afgelopen jaren zijn er daarom meerdere methodes ontwikkeld waarbij de oogarts met een apparaat naar het netvlies kan kijken, om zo te zien of de zenuwen zijn aangetast. Helaas zijn ook deze methoden niet goed genoeg om met 100% zekerheid te voorspellen of iemand lijdt aan glaucoom. Over het algemeen wordt 1 op de 10 patiënten niet goed beoordeeld met deze methoden, wat betekent dat glaucoom kan worden ontdekt bij iemand die het niet heeft, of dat glaucoom over het hoofd wordt gezien.

8.3 Nieuwe detectiemethoden

In dit proefschrift zullen we twee nieuwe methoden beschrijven die zijn ontwikkeld om glaucoom met meer zekerheid, en in een vroeger stadium te kunnen ontdekken. Beide methoden zijn gebaseerd op *optical coherence tomography*, of OCT, een techniek waarbij met licht contactloos een dieptescan kan worden gemaakt. Je zou OCT kunnen vergelijken met ultrasound, of radar. In OCT gebruiken we een speciaal soort laserlicht, veilig voor het oog, waarmee een dieptescan het netvlies tot op zo'n 5 μm nauwkeurig, of eentiende van de dikte van een hoofdhaar, in kaart kan brengen. We kunnen daarmee dus heel nauwkeurig laagdiktes meten, en dus ook de dikte van de zenuwlaag, een belangrijke indicator voor glaucoom. Als mensen regelmatig naar de oogarts gaan en hun ogen met het apparaat laten doormeten, dan kunnen veranderingen ter grootte van zo'n 5 μm gemeten worden.

OCT wordt nu al gebruikt door oogartsen. Bestaande apparaten zijn helaas niet zo nauwkeurig als hierboven beschreven en zijn ook relatief langzaam, waardoor je maar een klein deel van het oog in kaart kunt brengen. Met een nieuwe methode die we hebben ontwikkeld, *spectral-domain* OCT, kunnen we dat veel sneller doen. Vergeleken met een OCT-apparaat dat nu door oogartsen gebruikt wordt, is de nieuwe methode zo'n 100 tot 150 keer sneller. In combinatie met een speciale lichtbron kunnen we zelfs met een nauwkeurigheid van 3,5 μm meten. Met deze methode kun je ook driedimensionale plaatjes van het netvlies maken. Voor het eerst in de geschiedenis kon een film met dertig plaatjes per seconde van het netvlies gemaakt worden. Hiermee konden we voor het eerst kleine bloedvaten in het lichtgevoelige deel van het oog, de fovea, zichtbaar maken.

Een andere techniek die we ontwikkelden voor de vroege detectie van glaucoom, is *polarization-sensitive* OCT, oftewel polarisatie-gevoelige OCT. Met deze methode kan de dubbelbrekendheid van het netvlies gemeten worden. Dubbelbrekendheid is geen ziekte, maar een eigenschap van een optisch materiaal als glas (kwarts), calciet, of doorzichtig zenuwweefsel in het netvlies. Dubbelbrekendheid en polarisatie zijn erg met elkaar verweven. Laten we eerst eens ingaan op polarisatie. Een Polaroid

zonnebril kan je gebruiken om licht, en dat hoeft geen zonlicht te zijn, te polariseren. Polariseren is een woord dat we ook kennen uit de politiek, en het betekent dat je richting geeft aan iets. Als je wel eens zo'n zonnebril gebruikt hebt, dan weet je dat het licht niet van richting verandert. Wat gebeurt er dan wel? Op een nog kleiner dan microscopische schaal kun je het licht modelleren als een trilling van lichtdeeltjes. Die deeltjes dansen op en neer en van links naar rechts *loodrecht* op de verplaatsingsrichting en ook kunnen ze rondom de as van de verplaatsingsrichting draaien. Je kunt dit vergelijken met een kind in een bewegende trein dat op en neer springt en van links naar rechts beweegt. Zelfs salto's in de breedte- en hoogte van de trein zijn toegestaan, zo lang ze maar loodrecht op de bewegingsrichting zijn. Met een polaroid zonnebril kun je ervoor zorgen dat de lichtdeeltjes nog maar in een richting trillen. Het licht is dan gepolariseerd.

Als gepolariseerd licht door een lege ruimte heen gaat, zoals een vacuüm, dan gebeurt dat met de snelheid van het licht en wel met een vaart van zo'n 300.000.000 meter per seconde. In lucht gaat dat bijna net zo snel, maar in glas gaat het al een stuk langzamer, en wel met zo'n 200.000.000 meter per seconde. In diamant is het "slechts" 100.000.000 meter per seconde. Dat laatste zorgt er trouwens voor dat licht zo apart weerkaatst wordt in diamanten. Het verschil in snelheid vertaalt zich in een "brekingsindex", de verhouding tussen de snelheid in het materiaal en die in vacuüm. Zo is de brekingsindex van glas grofweg $300.000.000/200.000.000 = 1.5$ en in diamant is het $300.000.000/100.000.000 = 3$. Hoe hoger de brekingsindex van een materiaal, hoe trager het licht zich verplaatst in datzelfde materiaal.

Terug naar de dubbelbrekendheid en de polarisatie. Met een zonnebril kunnen we licht in een richting laten trillen. Draaien we de zonnebril een kwartslag, dan kunnen we het licht loodrecht op de eerste richting laten trillen. We hebben het dan over horizontaal en verticaal gepolariseerd licht. Stel nu eens dat ons optisch materiaal zich met horizontaal gepolariseerd licht gedraagt als glas, en met verticaal gepolariseerd licht als diamant. Dat betekent dat het licht het snelst door het materiaal heen gaat als het horizontaal gepolariseerd is. Zulke materialen bestaan, en we noemen ze dubbelbrekende materialen. Door nu het verschil in snelheid tussen deze twee richtingen te meten, kun je bepalen hoe dubbelbrekend het materiaal is. Het verschil in brekingsindex tussen beide richtingen wordt dubbelbrekendheid genoemd. In het Engels wordt dit verschijnsel "*birefringence*" genoemd, als in "*bi*" (twee/dubbel) "*refraction*" (breking).

Iedere zenuw in het netvlies is dubbelbrekend. Echter, als de zenuwen kriskras boven op elkaar liggen, dan is de totale hoeveelheid dubbelbrekendheid meestal te verwaarlozen. De zenuwen moeten netjes gerangschikt zijn om een dubbelbrekende laag te kunnen vormen. Waarom is dat? Ietwat versimpeld: een dubbelbrekend materiaal zorgt voor snelheidsverschillen. De snelheid in een vlak, loodrecht op de verplaatsingsrichting, is anders dan in het andere vlak, dat ook loodrecht op de verplaatsingsrichting staat. Als deze vlakken niet precies met elkaar in een lijn liggen,

dan kan het zijn dat bijvoorbeeld het snellere vlak 1 van de eerste zenuw in dezelfde lijn ligt met het langzamere vlak 2 van de tweede zenuw. De totale snelheid is nu afhankelijk van twee brekingsindices. Alleen als alle zenuwen met hetzelfde vlak in een lijn liggen, dan wordt hun snelheid bepaald door één brekingsindex. Hetzelfde geldt voor het andere vlak, en dus ook voor de dubbelbrekendheid. In werkelijkheid meten we geen snelheidsverschillen, maar een faseverschil. Ik ga hier verder niet op in, omdat het dan te complex wordt, maar het is goed om te onthouden dat een gemeten faseverschil in verhouding staat tot een snelheidsverschil tussen de twee polarisatie-richtingen. Hoe groter het faseverschil, hoe groter het snelheidsverschil.

Met polarisatie-gevoelige OCT kunnen we de dubbelbrekendheid van het zenuwweefsel meten, en we kunnen tegelijkertijd meten hoe dik het zenuwweefsel is. Toen we deze studie begonnen, werd alom aangenomen dat de dubbelbrekendheid van gezond zenuwweefsel in het netvlies constant is. Verder dachten we dat de dubbelbrekendheid van het zenuwweefsel zou veranderen onder invloed van glaucoom. De ziekte zorgt ervoor dat het zenuwweefsel wordt afgebroken, en we dachten dat als de opengevallen plaatsen zouden worden ingenomen door niet dubbelbrekend weefsel (wat bekend was uit de literatuur), dat dit zou leiden tot een verandering in de hoeveelheid dubbelbrekendheid. Nadat we metingen hadden uitgevoerd op een aantal gezonde proefpersonen bleek dat de dubbelbrekendheid niet constant is. Afhankelijk van waar er gemeten wordt in het oog, blijkt de dubbelbrekendheid flink te variëren. De laagste waarde voor dubbelbrekendheid is grofweg vier keer zo laag als de hoogste waarde. De eerste metingen die we met glaucoompatiënten deden, waren niet erg bemoedigend. De ogen van glaucoompatiënten zijn meestal ouder, en drogen snel uit. Ook zijn er vaak sporen van staar. De combinatie van al deze factoren zorgde ervoor dat er niet genoeg licht van het OCT systeem het netvlies kon bereiken. Het resultaat daarvan was dat we hele vage OCT plaatjes kregen. Een ander probleem was dat we meer dan een minuut nodig hadden om een complete scan te maken. Door nu spectral-domain OCT te combineren met polarisatie-gevoelige OCT, konden we de meettijd terugbrengen tot iets meer dan een seconde, terwijl we vier keer zo gevoelig konden meten.

Tot zover hebben metingen op glaucoompatiënten nog geen uitsluitsel kunnen geven over wat de invloed is van glaucoom op de dubbelbrekendheid van het zenuwweefsel. Daar waar het relatief eenvoudig was om gezonde ogen te meten, bleek het erg lastig te zijn om het netvlies in oudere ogen van glaucoompatiënten te meten. Een conclusie kan pas worden gegeven als we meetresultaten van meer patiënten hebben.

9. Appendix

Images in color

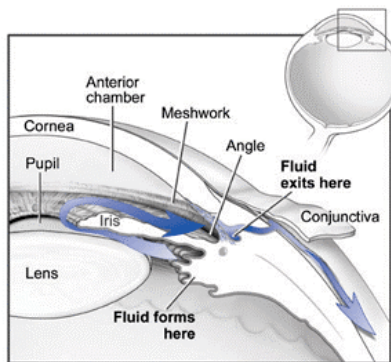


Figure 2 (p. 3): The eye's ciliary body ("Fluid forms here"), located near the lens, creates a translucent fluid that provides nutrients to transparent elements such as the lens and cornea. In a healthy eye, the influx of these fluids (the aqueous humor) is in balance with the outflow through the trabecular meshwork ("Meshwork") and Schlemm's canal ("Fluid exits here"). The latter is located at the periphery of the iris, beneath the sclera (image is courtesy of the National Eye Institute and National Institute of Health).

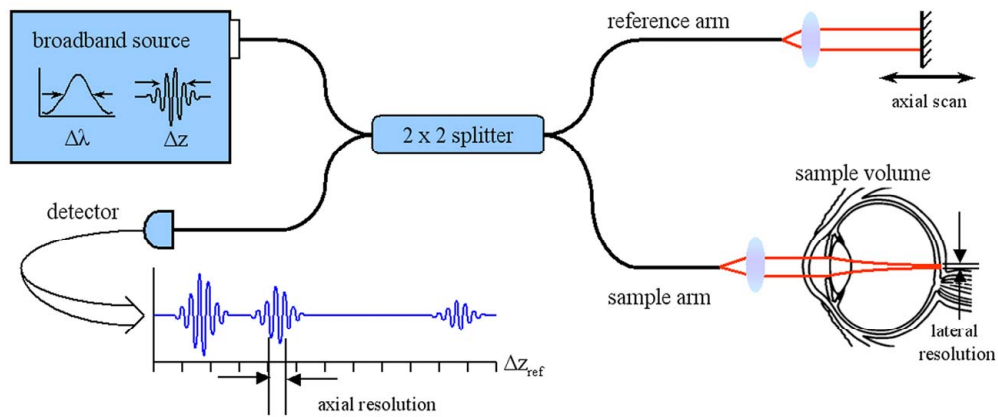


Figure 3 (p. 12): Schematic of a fiber-based setup for optical coherence tomography. Light from a broadband source is divided between reference and sample arms. The optical path length of the reference arm is modulated, and light returning from the two arms is recombined in the 50/50 splitter. Fifty percent of the light goes to the detector arm. A photosensitive detector records interference fringes only when the lengths of sample and reference arms match to within one coherence length.

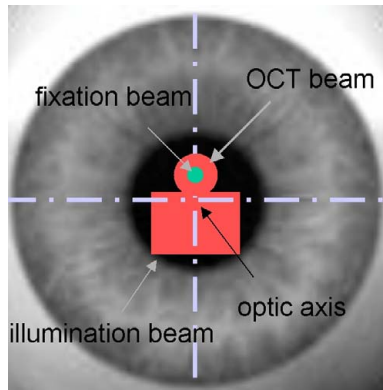


Figure 6 (p. 17): Reconstruction of the pupil plane. The fixation beam, OCT beam and illumination beam pass through the pupil. The fixation beam and OCT beam are slightly offset with respect to the optic axis of the CCD camera (crossed lines), while the illumination beam slightly overlaps with this axis.

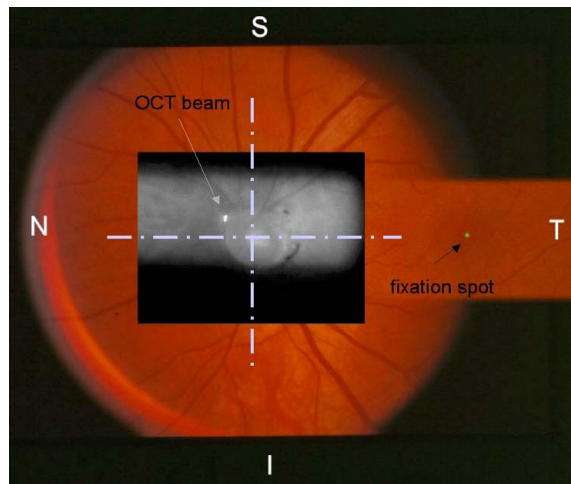


Figure 7 (p. 18): A composition of fundus images of the area around the optic nerve head (left) and around the fovea (right), both in color. The field of view of the CCD camera was much smaller than the field of view of the fundus camera, with an even smaller illuminated field. The cross indicates the position of the optic axis of the CCD camera. The fixation spot was added artificially.

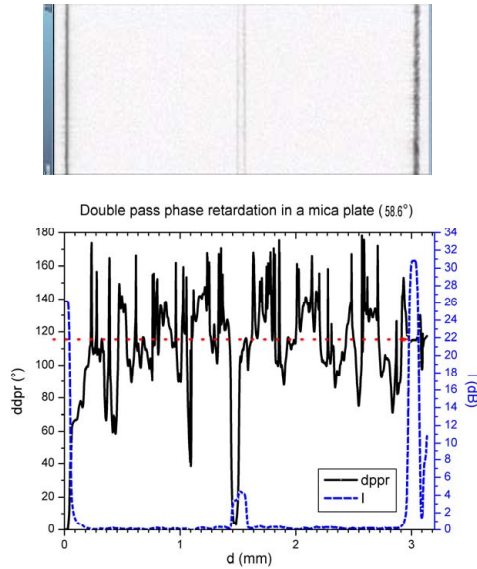


Figure 11 (p. 33): Structural intensity image (top) obtained with PS-OCT from a mica wave plate. The mica retarder was approximately $50 \mu\text{m}$ thick and glued between two glass plates. The image is rotated by 90° to match the graph (bottom). The graph shows the DPPR and intensity as a function of depth. The black line represents the DPPR, and touches the dotted red line at depths of approximately 1.45 mm and 3 mm . At these locations, the DPPR is equal to approximately 118° . The wave plate was measured by the manufacturer at 830 nm , yielding a phase retardation of 58.6° (single-pass).

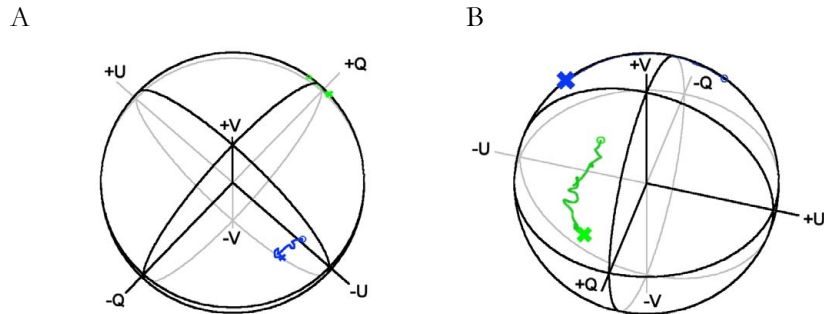


Figure 14 (p. 37). Evolution of the Stokes vectors with depth, from data averaged over 32 A-lines. The Poincaré sphere is oriented such that the axis of rotation is pointing out of the plane of the drawing. The two thick lines show the change in Stokes vectors over a distance of $85 \mu\text{m}$ in the RNFL (A), and $200 \mu\text{m}$ in the RNFL (B) and X's indicate the surface Stokes states. Circles indicate the Stokes state that is deepest in the tissue. The DPPR is derived from the angle of rotation about the optic axis, starting with the Stokes vector that belongs to the surface and finishing with the vector that belongs to a certain depth.

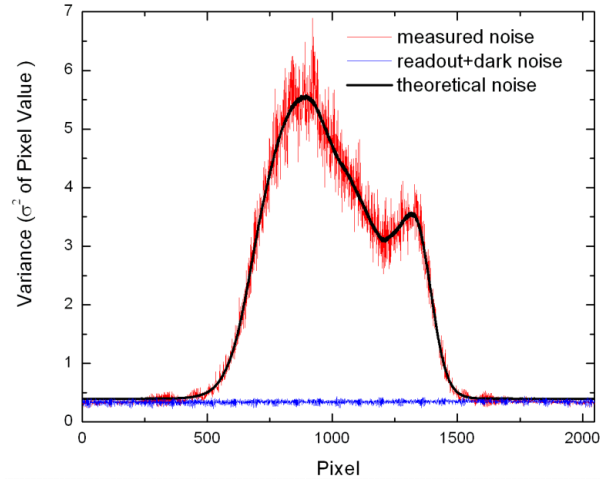


Figure 29 (p. 64). Noise components in the spectrometer. The shot noise level was determined with illumination of the reference arm only, and was used to determine the A/D resolution of the detector. The theoretical shot noise curve was fit using Eq. 24 to the measured average spectrum ($I_{c,PV}$), giving an analogue to digital conversion Δe of 173 electrons and a corresponding well depth of 177,000 electrons.

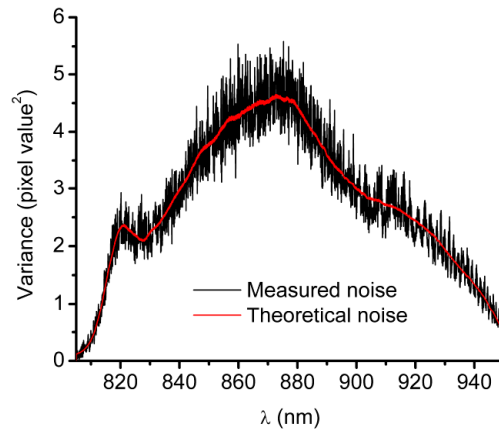


Figure 38 (p. 78). Shot noise measurement using the BroadLighter in an SD-OCT configuration. The shot noise level was determined with illumination of the reference arm only. The measured shot noise curve was fit with a theoretical expression for the shot noise, demonstrating that the system was shot-noise-limited.

Acronyms and medical terms

ANSI	American National Standards Institute
C/C	Choriocapillaris and choroid
CCD	Charged coupled device
dB	Decibel or $-10 \times \log_{10}$
DPPR	Double-pass phase retardation
DPPR/UD	Double-pass phase retardation per unit depth
ELM	External limiting membrane
FWHM	Full width at half maximum
GDx	Brand name for a scanning laser polarimeter
HP-SLD	High-power superluminescent diode
HRT	Heidelberg retinal tomograph
INL	Inner nuclear layer
IOP	Intra ocular pressure
IPL	Inner plexiform layer
IPR OR IPRL	Interface between inner and outer segments of the photoreceptor layer
OCT	Optical coherence tomography
ONH	Optic nerve head
ONL	Outer nuclear layer
OPL	Outer plexiform layer
POAG	Primary open angle glaucoma
PBS	Polarizing beam splitter
PM	Polarization modulator
PS-OCT	Polarization-sensitive optical coherence tomography
PS-SD-OCT	Spectral-domain polarization-sensitive optical coherence tomography
RNFL	Retinal nerve fiber layer
RPE	Retinal pigmented epithelium
RSOD	Rapid scanning delay line
SD-OCT	Spectral-domain optical coherence tomography
SLO	Scanning laser ophthalmoscope
SLP	Scanning laser polarimeter
VCC	Variable cornea compensator
Inferior	Down
Nasal	Towards the nose
Superior	Up
Temporal	Towards the temple

For both eyes, the fovea is located temporal to the optic nerve head.

Cataract	“ <i>Staar</i> ”, disease that causes scattering in the lens
Myopia	A collective word for “ <i>verziend</i> ” and “ <i>bijziend</i> ”
Anisometropic amblyopia	“ <i>Lui oog</i> ”

Acknowledgements

I am grateful for the help and contributions from my colleagues, as well as for the support from my family and friends. I would like to thank my parents for supporting me throughout these years, away from home.

I would like to thank Johannes de Boer for his support, and for only accepting the best results. Furthermore, I thank his extremely stable right eye for and his time for all the imaging sessions. Ton van Leeuwen smoothly guided me towards this end result. During the talks that I gave in Amsterdam, I received valuable input from Ton and his colleagues from the AMC.

I have been very lucky working with people who were not only colleagues, but also friends. Special thanks go towards my two office mates, Mark Pierce and Hyle Park. Sharing an office the size of a shoebox, often more than five days a week, without ever having a fight deserves to be mentioned. More important, without their help with all kinds of theory, language questions, software and hardware, far less would have been achieved. Hyle did an incredible job writing the data acquisition- and analysis software for the first polarization-sensitive system, described in Chapter 3. Mark's red pencil was highly appreciated for all posters, publications and this thesis.

The cover was made by Jill Parrin. Last summer, she also built the galvanometer controller's box and analyzed most of the data of Chapter 3. She also kept me sane throughout three years of living and working in Boston.

For Chapter 4 of this thesis, Nader Nassif and Hyle wrote the acquisition software, and Nader designed most of the spectrometer. Sections 4.2.3 and 4.3.3 of this thesis were basically from his hand and added to give a complete overview of the spectral-domain work.

Chulmin Joo wrote the acquisition code for the spectral-domain polarization-sensitive system, and in collaboration with Taner Akkin, who aligned the polarization modulator and the isolator, we managed to synchronize all components in the setup. This was a very ambitious project and since an increase of the number of components leads to an exponential increase in problems, Chulmin's perseverance in solving all synchronization problems deserves to be mentioned here. For Chapter 5, Mircea Mujat created the beautiful SLO image from our OCT data sets and helped me to improve the slit lamp design. The analysis software that was written in Matlab was based on code written by Hyle, Johannes, Brian White, Mircea and Mark.

A dermatology department is probably not the best place to do eye research. Teresa Chen of the Massachusetts Eye and Ear Infirmary has helped us tremendously with different problems related to glaucoma and the eye. She also caught many errors in papers and this thesis. This research could not have been done without the contributions of volunteers and glaucoma patients, whose eyes were checked at her clinic.

Rob Webb helped me out with many eye-related issues or questions about scanning technology. The eye safety calculations in this thesis were performed using a program written by Francois Delori from the Schepens Eye Research Institute. He also helped me with the discovery of the tiny blood vessels in the high-resolution OCT images of the fovea, which is something that should have been acknowledged in the Optics Express paper.

My colleagues in the labs of Gary Tearney, Brett Bouma, Charles Lin and Rox Anderson have been very helpful lending equipment or solving hardware problems. Special thanks to Clemens Alt, Bill Farinelli, Milen Shiskov and Nic Iftimia (currently with PSI) for helping with hardware problems and machining-related issues.

Ray Chan has helped us a lot with image reconstruction and image analysis of the latest polarization-sensitive results. Andy Yun has been a terrific resource for hard- and software answers regarding the spectral-domain technology.

The machine shop of the biomedical department caught many of my design errors. It is always a pleasure to work with a machine shop that has short lead times and an eye for detail.

I would like to thank Gene Vanderpool (a very far cousin of former Dutch cyclist Adrianus van der Poel), who was our staff assistant for many years. I would like to thank Susan Weeks' administrative staff, especially Dora Gaudette, for their help with conflicts with the Purchasing Department, vendors, purchasing, and visa issues.

Some of the work described in this thesis has benefited from cooperation between our lab and other labs. I would like to mention Tom Milner's lab in Texas, and Robert Knighton's lab in Florida.

Last, I would like to thank the management of Philips Research, who pushed me towards grad school. Not only PhDs write scientific papers.

Curriculum vitae

September 16, 1973	Born in Eindhoven
1985-1991	Eindhovens Protestants Lyceum, Eindhoven, Atheneum-B
1991-1995	Fontys Hogeschool Eindhoven, Eindhoven, Applied physics. <i>Ingenieurs</i> diploma (ing.), equivalent to BS degree
1995-2001	Philips Research, Eindhoven - Research assistant - 5 patents granted
2001-present	Wellman Center for Photomedicine and Harvard Medical School, Boston, Massachusetts, USA - Sr. research technologist - Graduate student

Barry Cense was born on September 16, 1973 in Eindhoven, the Netherlands. After finishing his secondary education in 1991, he studied Applied Physics at the Fontys Hogeschool Eindhoven. During his final internship with Philips Research he was offered a job as a research assistant. He worked on various projects, ranging from measuring skin and hair parameters to the development of a diode laser hair removal system. This work resulted in five granted US patents. In 2001 he took a job as a research technologist with the Wellman Center for Photomedicine in Boston, Massachusetts. In 2001 he started his PhD work, which focused on the measurement of thickness and birefringence of the human retinal nerve fiber layer. The author currently lives in Belmont, Massachusetts.